

University of Louisville

ThinkIR: The University of Louisville's Institutional Repository

Electronic Theses and Dissertations

12-2021

Aggregation dynamics of bulk nanoparticle haloing systems and the influence of non-ambient temperatures.

Marzieh Moradi
University of Louisville

Follow this and additional works at: <https://ir.library.louisville.edu/etd>



Part of the [Complex Fluids Commons](#)

Recommended Citation

Moradi, Marzieh, "Aggregation dynamics of bulk nanoparticle haloing systems and the influence of non-ambient temperatures." (2021). *Electronic Theses and Dissertations*. Paper 3801.

Retrieved from <https://ir.library.louisville.edu/etd/3801>

This Doctoral Dissertation is brought to you for free and open access by ThinkIR: The University of Louisville's Institutional Repository. It has been accepted for inclusion in Electronic Theses and Dissertations by an authorized administrator of ThinkIR: The University of Louisville's Institutional Repository. This title appears here courtesy of the author, who has retained all other copyrights. For more information, please contact thinkir@louisville.edu.

AGGREGATION DYNAMICS OF BULK NANOPARTICLE HALOING SYSTEMS
AND THE INFLUENCE OF NON-AMBIENT TEMPERATURES

By
Marzieh Moradi
B.S., Isfahan University of Technology, 2007
M.S., Isfahan University of Technology, 2010

A Dissertation
Submitted to the Faculty of the
J.B. Speed School of Engineering of the University of Louisville
in Partial Fulfillment of the Requirements
for the Degree of

Doctor of Philosophy
in Chemical Engineering

Department of Chemical Engineering
University of Louisville
Louisville, Kentucky

August 2021

Copyright 2021 by Marzieh Moradi

All rights reserved

AGGREGATION DYNAMICS OF BULK NANOPARTICLE HALOING SYSTEMS
AND THE INFLUENCE OF NON-AMBIENT TEMPERATURES

By
Marzieh Moradi
B.S., Isfahan University of Technology, 2007
M.S., Isfahan University of Technology, 2010

A Dissertation approved on

June 22, 2021

by the following dissertation Committee:

Dr. Gerold A. Willing, Dissertation Director

Dr. Stuart J. Williams

Dr. Vance Jaeger

Dr. James Watters

DEDICATION

I dedicate my dissertation to my husband, Amir, for his love, support, and encouragement.

And to my parents, Esfandiar and Farangis, merci Baba va Maman, for their endless love and for raising me to believe everything is possible.

ACKNOWLEDGMENTS

I would like to express my sincere gratitude to my advisor, Dr. Gerold Willing, for his encouragement, invaluable advice, continuous support, and patience during my Ph.D. study.

I would like to thank my co-advisor, Dr. Stuart Williams, for his valuable input and guidance and for providing support with the confocal microscopy.

I would also like to thank Dr. Vance Jaeger for his kind help and valuable technical support, which helped me shape my experiment methods and critique my results.

My sincere thanks to Dr. James Watters for his support and for agreeing to serve on my Ph.D. defense committee.

I greatly acknowledge the funding received towards my Ph.D. from NASA EPSCoR (Grant No. NNX14AN28A), which made this dissertation possible.

I thank the support of the faculty and staff of the Department of Chemical Engineering and the Conn Center.

I would like to express gratitude to Patricia Lumley and Mary Stewart for their support.

Thanks to my family, friends, and lab mates for their support, understanding, encouragement, and help.

ABSTRACT

EFFECT OF GRAVITY AND TEMPERATURE ON THE AGGREGATION OF BULK NANOPARTICLE HALOING SYSTEMS

Marzieh Moradi

June 22, 2021

One of the methods of assembling colloids into 3D crystal structures is through the use of nanoparticle haloing. Nanoparticle haloing is a stabilization mechanism in binary particle suspensions possessing both a size and charge asymmetry, with which the nanoparticles aid in the bulk suspension's stability. By altering the volume fractions of nanoparticles, it is possible to control the effective repulsion between the microparticles.

Understanding the colloidal interactions and aggregate crystallinity as a function of nanoparticle concentration, temperature, and time are key challenges in developing future materials and designing crystalized 3D colloidal systems. In this study, we investigated the effect of temperature and nanoparticle volume fraction on the aggregation size using experimental techniques and molecular dynamics simulations.

Gravity settling results showed a rapid aggregation in the absence of the nanoparticles due to the van der Waals interactions. However, by adding the nanoparticles to the system, the rate of gravity settling and aggregation significantly decreased due to the effective potential barrier that arises from the nanoparticle halo formation.

The effect of temperature on the aggregation of the nanoparticle haloing systems was investigated using a confocal microscopy. By applying a temperature shock to the

binary suspensions, the average colloid aggregates' size increased while the systems' coarseness decreased. The average aggregate size growth was more significant at the higher temperatures and the lower nanoparticle volume fractions. Overall, applying the temperature shock resulted in a more idealized structure with higher crystallinity.

Molecular dynamics simulations were employed to determine the repulsive barrier between colloidal particles induced by the nanoparticles as a function of nanoparticle volume fraction. Results showed that the induced repulsive barrier between the microparticles increases with increasing the volume fractions of nanoparticles, and it reaches $6.5 k_B T$ at the highest nanoparticle volume fraction of $\varphi_{\text{nano}} = 10^{-3}$. This potential barrier was strong enough to prevent aggregation gelation and increase the stability of the suspension, which was in agreement with the experimental results.

TABLE OF CONTENTS

CHAPTER 1: INTRODUCTION	1
1.1. COLLOIDAL SYSTEMS.....	1
1.2. COLLOID STABILITY	3
1.3. VAN DER WAALS AND DOUBLE LAYER INTERACTIONS	5
1.4. DLVO THEORY	11
1.5. NANOPARTICLE REGULATED COLLOIDAL SYSTEMS	12
1.6. PREVIOUS STUDIES.....	13
1.7. FORCE PROFILES IN PRESENCE OF NANOPARTICLES	16
1.8. OUR WORK.....	17
CHAPTER 2: MICROPARTICLE SYNTHESIS AND CHARACTERIZATION	19
2.1. INTRODUCTION	19
2.2. MATERIALS AND METHODS.....	21
2.2.1. MATERIALS.....	23
2.2.2. PARTICLE SYNTHESIS.....	23
2.2.3. STRUCTURE, MORPHOLOGY, AND SIZE.....	25
2.2.4. ZETA POTENTIAL	25
2.2.5. DENSITY	26
2.2.6. SPECIFIC SURFACE AREA.....	26
2.3. RESULTS AND DISCUSSION	27
2.3.1. MORPHOLOGY	27
2.3.2. ZETA POTENTIAL	32
2.3.3. DENSITY	35
2.3.4. SPECIFIC SURFACE AREA.....	35
2.3.5. GENERAL OVERALL STRUCTURE.....	37
2.4. CONCLUSION.....	38
CHAPTER 3: GRAVITY SETTLING OF NANOPARTICLE HALOING SYSTEMS	39
3.1. INTRODUCTION	39
3.2. METHODS	45
3.2.1. SUSPENSION PREPARATION.....	46

3.2.2. GRAVITY SETTLING OF THE BINARY SYSTEMS	46
3.2.3. IMAGING OF THE BINARY SUSPENSIONS	47
3.3. RESULTS AND DISSCUSION	47
3.3.1. GRAVITY SETTLING IMAGES	47
3.3.2. MICROSCOPY IMAGES	55
3.4. CONCLUSION.....	60
CHAPTER 4: EFFECT OF TEMPERATURE ON NANOPARTICLE HALOING SYSTEMS.....	62
4.1. INTRODUCTION	62
4.2. METHODS	64
4.2.1. TEMPERATURE EXPERIMENTS ON THE ISS	66
4.2.2. GRAVITY TEMPERATURE EXPERIMENTS.....	67
4.2.3. IMAGE ANALYSIS.....	69
4.3. RESULTS AND DISSCUSION	70
4.4. CONCLUSION.....	81
CHAPTER 5: MOLECULAR DYNAMICS SIMULATIONS OF NANOPARTICLE HALOING BINARY SYSTEMS	83
5.1. INTRODUCTION	83
5.2. THEORY	88
5.2.1. INTERACTIONS BETWEEN PARTICLES.....	88
5.2.2. UMBRELLA SAMPLING	91
5.2.3. MD AGGREGATION STUDIES.....	93
5.3. RESULTS AND DISCUSSION	95
5.3.1. INTERACTIONS BETWEEN PARTICLES.....	95
5.3.2. UMBRELLA SAMPLING	98
5.3.3. MD AGGREGATION STUDIES.....	100
5.4. CONCLUSION.....	102
CHAPTER 6: CONCLUSION AND FUTURE WORK	104
6.1. CONCLUSION.....	104
6.2. FUTURE WORK.....	107
REFERENCES	109
CURRICULUM VITAE.....	118

LIST OF TABLES

Table 1.1. Different types of colloidal dispersions	2
Table 2.1. Descriptive statistics of the amount of different elements in the surface layer of the BC-SSQ and BC-A-SSQ particles ⁷¹	30
Table 2.2. ImageJ analysis data of the BC-SSQ samples ⁷¹	35

LIST OF FIGURES

Figure 1.1. Definition of zeta potential ¹⁴	4
Figure 1.2. Qualitative sketch of zeta potential variation with pH	5
Figure 1.3. Total interaction energy curves, $V(1)$ and $V(2)$, obtained by the summation of an attraction curve, V_A , with different repulsion curves, $V_R(1)$ and $V_R(2)$. ¹	12
Figure 2.1. Light microscopy module images of binary systems of benzyl chloride-functionalized silsesquioxane with a rhodamine B fluorescent tag (BC-SSQ-RhB) (600 nm diameter) and ZrO ₂ nanoparticles(8 nm) at 10x on the ISS at start and over 1.9 and 9 days from top to bottom ($\varphi_{micro} = 1$, $\varphi_{nano} = 10^{-4}$, at pH 1.5).....	20
Figure 2.2. XRD patterns for amorphous a BC-SSQ and b BC-A-SSQ ⁷¹	28
Figure 2.3. HIM images of BC-SSQ and BC-A-SSQ ⁷¹	29
Figure 2.4. SEM images of BC-SSQ and BC-A-SSQ ⁷¹	30
Figure 2.5. Lognormal differential distributions of particle sizes weighted by volume for a BC-SSC and b BC-A-SSQ particles ⁷¹	31
Figure 2.6. Plot of the effective zeta potential (ξ) of the BC-SSQ, BC-SSQ-RhB, BC-A-SSQ, and BC-A-SSQ-RhB microparticles as a function of pH ⁷¹	33
Figure 2.7. Images of the BC-SSQ particles at pH 3 and 4 and isoelectric point after 4 h using inverted microscopy (20x) ⁷¹	34
Figure 2.8. N ₂ adsorption-desorption isotherm and pore size distribution of a BC-SSQ and b BC-A-SSQ ⁷¹	36
Figure 3.1. Gravity settling experiments setup	47
Figure 3.2. Gravity settling experiment results of BC-SSQ microparticles ($\varphi_{micro} = 10^{-2}$) without nanoparticles (a) at start (b) after 2 hours (c) after 6 hours at different pH values of 2 to 8.	49
Figure 3.3. Gravity settling experiment results of binary systems of BC-SSQ microparticles ($\varphi_{micro} = 10^{-2}$) with SiO ₂ nanoparticles at (a) $\varphi_{nano} = 10^{-4}$ at start (b) $\varphi_{nano} = 10^{-3}$ at start (c) $\varphi_{nano} = 10^{-4}$ after 2 hours (d) $\varphi_{nano} = 10^{-3}$ after 2 hours (e) $\varphi_{nano} = 10^{-4}$ after 6 hours (f) $\varphi_{nano} = 10^{-3}$ after 6 hours at different pH values of 2 to 8.....	50
Figure 3.4. Gravity settling experiment results of binary systems of BC-SSQ microparticles ($\varphi_{micro} = 10^{-2}$) with AlOOH nanoparticles at (a) $\varphi_{nano} = 10^{-4}$ at start (b) $\varphi_{nano} = 10^{-3}$ at start (c) $\varphi_{nano} = 10^{-4}$ after 2 hours (d) $\varphi_{nano} = 10^{-3}$ after 2 hours (e) $\varphi_{nano} = 10^{-4}$ after 6 hours (f) $\varphi_{nano} = 10^{-3}$ after 6 hours at different pH values of 2 to 8.....	51

Figure 3.5. Gravity settling experiment results of binary systems of BC-SSQ microparticles ($\phi_{\text{micro}} = 10^{-2}$) with ZrO_2 nanoparticles at (a) $\phi_{\text{nano}} = 10^{-4}$ at start (b) $\phi_{\text{nano}} = 10^{-3}$ at start (c) $\phi_{\text{nano}} = 10^{-4}$ after 2 hours (d) $\phi_{\text{nano}} = 10^{-3}$ after 2 hours (e) $\phi_{\text{nano}} = 10^{-4}$ after 6 hours (f) $\phi_{\text{nano}} = 10^{-3}$ after 6 hours at different pH values of 2 to 8.....	52
Figure 3.6. Images of gravity settling experiments of binary systems of BC-SSQ at isoelectric point with $\phi_{\text{nano}} = 0, 10^{-4}$ and 10^{-3} over time.....	53
Figure 3.7. Inverted microscopy images of binary systems of BC-SSQ microparticles ($\phi_{\text{micro}}=10^{-2}$) and ZrO_2 nanoparticles ($\phi_{\text{nano}}=0$) at isoelectric point after 2 days with (a) 4x magnification (b) 10x magnification (c) 20x magnification.....	56
Figure 3.8. Inverted microscopy images of binary systems of BC-SSQ microparticles ($\phi_{\text{micro}}=10^{-2}$) and ZrO_2 nanoparticles ($\phi_{\text{nano}}=10^{-4}$) at isoelectric point after 2 days with (a) 4x magnification (b) 10x magnification (c) 20x magnification.....	57
Figure 3.9. Inverted microscopy images of binary systems of BC-SSQ microparticles ($\phi_{\text{micro}}=10^{-2}$) and ZrO_2 nanoparticles ($\phi_{\text{nano}}=10^{-3.26}$) at isoelectric point after 2 days with (a) 4x magnification (b) 10x magnification (c) 20x magnification	58
Figure 3.10. Inverted microscopy images of binary systems of BC-SSQ microparticles ($\phi_{\text{micro}}=10^{-2}$) and ZrO_2 nanoparticles ($\phi_{\text{nano}}=10^{-3}$) at isoelectric point after 2 days with (a) 4x magnification (b) 10x magnification (c) 20x magnification.....	59
Figure 4.1. ISS experimental setup.....	67
Figure 4.2. Temperature shock experiment setup.....	68
Figure 4.3. Temperature shock heating and cooling steps.....	68
Figure 4.4. (a) An example of confocal laser scanning microscope image with 40x magnification (white particles on black background) and (b) resulting image after applying watershed using ImageJ (black blobs on white background)	71
Figure 4.5. Average blob size of the binary systems with $\phi_{\text{micro}}=10^{-3}$ BC-SSQ microparticles and $\phi_{\text{nano}} = 10^{-4}, \phi_{\text{nano}} = 10^{-3.26}, \phi_{\text{nano}} = 10^{-3}$ ZrO_2 nanoparticles, during 60°C temperature shock cycle.....	72
Figure 4.6. Average blob size of the binary systems with $\phi_{\text{micro}}=10^{-3}$ BC-SSQ microparticles and $\phi_{\text{nano}} = 10^{-4}, \phi_{\text{nano}} = 10^{-3.26}, \phi_{\text{nano}} = 10^{-3}$ ZrO_2 nanoparticles, during 70°C temperature shock cycle.....	73
Figure 4.7. Average blob size of the binary systems with $\phi_{\text{micro}}=10^{-3}$ BC-SSQ microparticles and $\phi_{\text{nano}} = 10^{-4}, \phi_{\text{nano}} = 10^{-3.26}, \phi_{\text{nano}} = 10^{-3}$ ZrO_2 nanoparticles, during 80°C temperature shock cycle.....	74
Figure 4.8. An example of radially averaged $S(q,t)$ at different steps of 60°C temperature shock cycle.....	75

Figure 4.9. Characteristic length of the binary systems with $\phi_{\text{micro}}=10^{-3}$ BC-SSQ microparticles and $\phi_{\text{nano}} = 10^{-4}$, $\phi_{\text{nano}} = 10^{-3.26}$, $\phi_{\text{nano}} = 10^{-3}$ ZrO ₂ nanoparticles, during 60°C temperature shock cycle.....	76
Figure 4.10. Characteristic length of the binary systems with $\phi_{\text{micro}}=10^{-3}$ BC-SSQ microparticles and $\phi_{\text{nano}} = 10^{-4}$, $\phi_{\text{nano}} = 10^{-3.26}$, $\phi_{\text{nano}} = 10^{-3}$ ZrO ₂ nanoparticles, during 70°C temperature shock cycle.....	77
Figure 4.11. Characteristic length of the binary systems with $\phi_{\text{micro}}=10^{-3}$ BC-SSQ microparticles and $\phi_{\text{nano}} = 10^{-4}$, $\phi_{\text{nano}} = 10^{-3.26}$, $\phi_{\text{nano}} = 10^{-3}$ ZrO ₂ nanoparticles, during 80°C temperature shock cycle.....	78
Figure 4.12. Microscopy images (4x magnification) of the binary systems of BC-SSQ microparticles ($\phi_{\text{micro}}=10^{-3}$) and ZrO ₂ nanoparticles ($\phi_{\text{nano}} = 10^{-4}$) (a) before and / (b) after 60°C (c) after 70°C (d) after 80°C temperature shock cycles.	79
Figure 4.13. Microscopy images (4x magnification) of the binary systems of BC-SSQ microparticles ($\phi_{\text{micro}}=10^{-3}$) and ZrO ₂ nanoparticles ($\phi_{\text{nano}} = 10^{-3.26}$) (a) before and (b) after 60°C (c) after 70°C (d) after 80°C temperature shock cycles.	80
Figure 4.14. Microscopy images (4x magnification) of the binary systems of BC-SSQ microparticles ($\phi_{\text{micro}}=10^{-3}$) and ZrO ₂ nanoparticles ($\phi_{\text{nano}} = 10^{-3}$) (a) before and (b) after 60°C (c) after 70°C (d) after 80°C temperature shock cycles.	81
Figure 5.1. Interaction energies and forces between (a) two microparticles (b) a microparticle and a nanoparticle (c) two nanoparticles	97
Figure 5.2. A rendering of the umbrella sampling simulation output for the binary system of $\phi_{\text{micro}} = 10^{-2}$ and $\phi_{\text{nano}} = 10^{-3}$ and separation distance of 20 nm. Figure is rendered in VMD using the Tachyon renderer.	98
Figure 5.3. Histograms of the configurations within the umbrella sampling windows with 44 bins, for the binary system with $\phi_{\text{nano}} = 10^{-6}$	99
Figure 5.4. The effective potential between a pair of silica colloidal particles as a function of zirconia nanoparticle volume fraction and separation distance	100
Figure 5.5. 3D and 2D Snapshots of MD simulations boxes filled with microparticles at nanoparticle volume fractions of (a,b) $\phi_{\text{nano}} = 10^{-5}$ (c,d) $\phi_{\text{nano}} = 10^{-4}$ (e,f) $\phi_{\text{nano}} = 10^{-3}$.	101

CHAPTER 1

INTRODUCTION

1.1. COLLOIDAL SYSTEMS

Colloids are systems with at least one component with dimensions in the nanometer or micrometer range ^{1, 2}. Colloids are classified into three main groups: colloidal dispersions, true macromolecule solutions, and association colloids. Colloidal dispersions are systems composed of disperse phase of solid particles that are much larger than the dispersion medium molecules. They are thermodynamically unstable due to their high surface free energy. Since a negative change in free energy is thermodynamically favorable, the system tends to aggregate to minimize the interfacial area. Macromolecules, such as proteins and polymeric solutions, can often be uniformly dispersed. These systems are thermodynamically stable and reversible. An association colloid, which is also thermodynamically stable and reversible, is a system with a number of molecules that associate together and form aggregates which are known as micelles ²⁻⁴.

Colloidal dispersions are two-phase systems consisting of a dispersed phase (the particles) and a dispersion medium (the medium in which the particles are distributed). The size of the suspended particles in a colloid can range from 1 nm to 1 μm . Different types of dispersions are listed in **Table 1.1** ^{2, 4}. Sols and emulsions are two most important types of colloidal dispersions.

Table 1.1. Different types of colloidal dispersions

Dispersion Phase	Disperse Phase	Name	Example
Gas	Liquid	Aerosol	Cloud, moist, fog
	Solid	Aerosol	Smoke, dust
Liquid	Gas	Foam	Beer
	Liquid	Emulsion	Mayonnaise, milk
	Solid	Sol/dispersion	Printing ink
Solid	Gas	Solid foam	Styrofoam
	Liquid	Solid emulsion	Ice cream, butter
	Solid	Solid dispersion	Glass, concrete

In colloidal dispersions, particles are large enough that definite surfaces of separation exist between the particles and the medium. The most important factors of colloidal systems are the size and shape of the particles, surface properties (charge), particle-particle interactions, and particle-solvent interactions. The most important types of colloidal dispersions are sols/colloidal suspensions (solid dispersed phase in a liquid medium) and emulsions (liquid dispersed phase in a liquid medium) ^{1,2}.

Colloidal particles and suspensions have been investigated widely due to their extensive applications from advanced materials to drug delivery ^{5,6}. Widespread research on colloidal particles has taken place in a number of application areas including coatings⁷, assembly of ceramics ⁸, photonic materials ⁹, and pharmaceutical materials ¹⁰. Different characteristics of colloidal suspensions and resulting products can be reached by tailoring both the morphology and chemistry of the colloidal particles ¹¹.

1.2. COLLOID STABILITY

Aggregation* in colloidal dispersions is an important property that depends on the interactions between the particles. In the absence of any repulsion interactions, van der Waal interactions between the particles result in the aggregation of particles. Electrostatic repulsive interactions are required to increase the stability of the colloidal dispersions^{2, 12, 13}.

Colloidal particles obtain a surface charge when they are in contact with an aqueous medium. This surface charge affects the nearby ions in the aqueous medium. Ions with opposite charge will be attracted towards the surface and ions of like charge will be repelled away from the surface. Electrokinetic behavior of colloids depends on the potential at the surface of shear between the charged surface and the solution which is known as zeta potential (shown in **Figure 1.1**). Zeta potential does not occur directly at the interface; It is the potential difference between the mobile dispersion medium and the stationary layer (slipping plane) of the dispersion medium attached to the dispersed particle. The pH of a colloidal suspension is one of the most important factors that affects its zeta potential^{2, 12}.

Figure 1.2 Shows a qualitative plot of zeta potential versus pH. Typically, zeta potential is positive at low pH, and it decreases by increasing the pH. The pH where zeta potential of a sample (net charge) becomes zero is called the isoelectric point. The isoelectric point of the sample in **Figure 1.2** is at pH 5.5. By adding an acid to the solution at the isoelectric point, the particles will acquire a positive charge, and the zeta potential will increase. However, by adding a base to the solution at the isoelectric, the particles will build up a

* In many of the colloid science literature, the terms aggregation and agglomeration are used interchangeably.

negative charge, and zeta potential will decrease (negative value). Colloidal systems are least stable at their isoelectric point since the only force between the particles is the van der Waals attractive force which causes the particles to aggregate and flocculate. Colloidal systems with zeta potential values of $>+30$ mV or <-30 mV are considered to have better stability since the particles have sufficient positive or negative net charges to repel each other ¹⁴

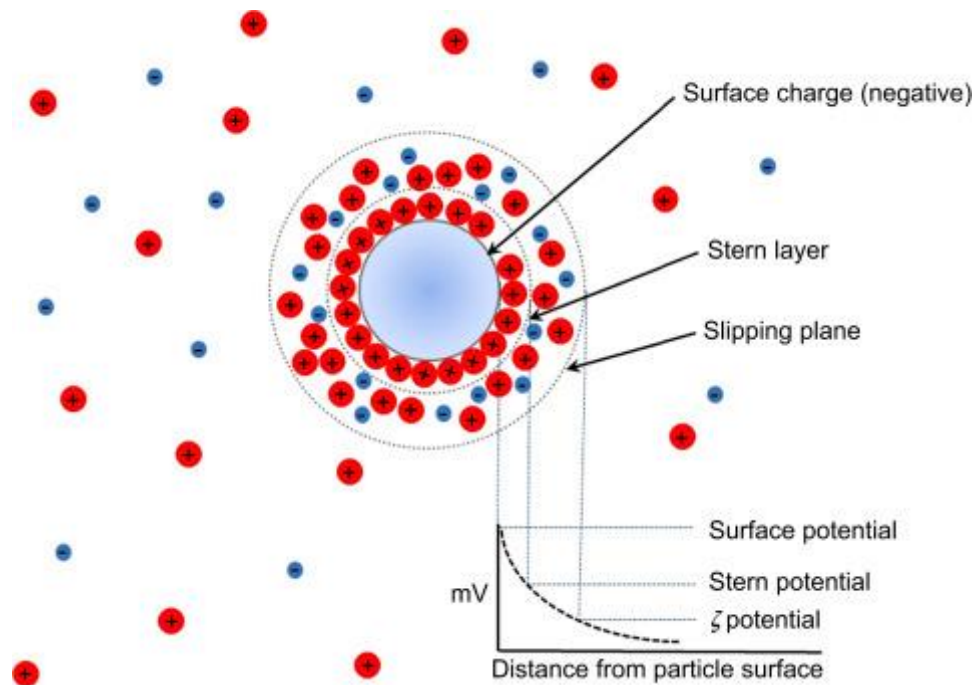


Figure 1.1. Definition of zeta potential ¹⁴

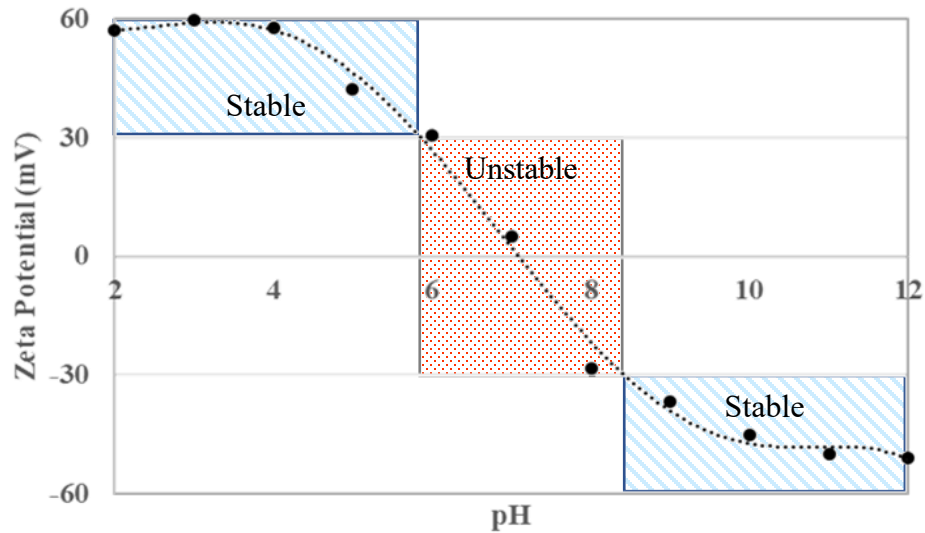


Figure 1.2. Qualitative sketch of zeta potential variation with pH

1.3. VAN DER WAALS AND DOUBLE LAYER INTERACTIONS

Van der Waals adsorption and electrical double layer caused by the electromagnetic effects of the molecules within the particles and the overlapping of the electrical double layers of particles determine the physical properties of the colloidal system. Interaction forces between colloidal particles can be determined by the potential distribution created by the variation of these molecules and ions, and between the particles themselves^{5, 6, 15}. Interaction forces are responsible for the stability of particles against aggregation and have an essential role in determining properties such as the shelf life, stability, rheology, and the overall behavior in several industrial processes (e.g., mixing and membrane filtration)¹⁵.

London-van der Waals interaction:

Brownian motion, which results from the thermal energy motion, is the random movement of dispersed particles as they continuously change direction due to the random collisions with the molecules of the dispersion phase, other dispersed particles, and the

walls of the container. When colloidal particles in a liquid medium collide, they tend to form persistent aggregates due to an inter-particle van der Waals attractive force ¹⁶⁻¹⁹.

The intrinsic van der Waals attraction between colloidal particles is always attractive, and it depends on the nature of the particles, the medium, and also on the geometry of the particles. Based on the molecules involved in the interaction, the three different Van der Waals forces are Keesom forces, Debye forces, and London forces. Keesom interactions occur when two permanent dipoles come in contact. Debye interactions are the attractive interaction that arises between polar molecules and nonpolar molecules. London forces occur in molecules without permanent dipoles. The fluctuations on the electron cloud cause temporary changes in the charge distribution, leading to a charge redistribution towards neighboring molecules. ^{17, 20}

The London attractive energy, V_A , between two spherical particles with R_1 and R_2 radii is given by ^{20, 21}:

$$V_A = -\frac{A}{6} \left[\frac{2R_1R_2}{r^2 - (R_1 + R_2)^2} + \frac{2R_1R_2}{r^2 - (R_1 - R_2)^2} + \ln \left\{ \frac{r^2 - (R_1 + R_2)^2}{r^2 - (R_1 - R_2)^2} \right\} \right] \quad (1.1)$$

Where A is the Hamaker constant, r is the center-to-center separation distance ($r = R_1 + R_2 + D$), and D is the surface-to-surface separation distance between particles. For two equal-sized particles with small separation distances ($D \ll R$), equations 1.1 reduces to ^{20, 21}:

$$V_A = -\frac{AR}{12D} \quad (1.2)$$

For a spherical particle of radius R and a flat surface ($R = \infty$), the total attractive interaction is ²²:

$$V_A = -\frac{A}{6} \left[\frac{R}{D} + \frac{R}{D + 2R} + \ln \left\{ \frac{D}{D + R} \right\} \right] \quad (1.3)$$

The total attractive force between a sphere near a plate ($D \ll R$) is ²¹:

$$V_A = -\frac{AR}{6D} \quad (1.4)$$

The Hamaker constant, A , depends on different properties of the dispersed phase and dispersion medium. The major difficulty in calculating the van der Waals interactions for colloidal particles is the measurement of the Hamaker constant. Two main methods used for calculating the Hamaker constant are the London-Hamaker microscopic approximation and Lifshitz macroscopic approximation. The London/Hamaker approach is the simplest microscopic approximation and is based on the London formula. In this approach, the total interaction energy is obtained by summing the total interactions between all interparticle atom pairs. This approach, which is valid for non-polar molecules, evaluates the Hamaker constant from individual atomic polarizabilities and atomic densities of particles. The macroscopic approach of Lifshitz does not assume the pairwise additivity of the individual intermolecular forces. In this approach, intervening media are treated as continuous phases, and forces are derived in terms of the bulk properties such as dielectric constants and refractive indices ^{21, 23, 24}.

Consider that there are two particles, 1 and 2, in a dispersion medium 3. When the particles are far from each other, the interactions are between the particle and dispersion, with Hamaker constants of A_{13} and A_{23} . But when the particles get close to each other, the particles are displaced by the dispersion medium. Therefore, the interactions become particle-particle interactions, and dispersion medium-dispersion medium interactions, with Hamaker constants of A_{12} and A_{33} . The effective Hamaker constant, A_{132} , in this system is given by ^{1, 2, 25}:

$$A_{132} = A_{12} + A_{33} - A_{13} - A_{23} \quad (1.5)$$

Based on the Berthelot principle, the attraction between two unlike phases can be given roughly by the geometric mean of the attractions of each phase considered separately where $A_{12} = (A_{11} \times A_{22})^{\frac{1}{2}}$, $A_{13} = (A_{11} \times A_{33})^{\frac{1}{2}}$, $A_{23} = (A_{22} \times A_{33})^{\frac{1}{2}}$. Therefore, equation 1.5 becomes ^{1, 2, 25}:

$$A_{132} = \left(A_{11}^{\frac{1}{2}} - A_{33}^{\frac{1}{2}} \right) \left(A_{22}^{\frac{1}{2}} - A_{33}^{\frac{1}{2}} \right) \quad (1.6)$$

If two particles are of the same material, equation 1.6 becomes ^{1, 2, 25}:

$$A_{131} = \left(A_{11}^{\frac{1}{2}} - A_{33}^{\frac{1}{2}} \right)^2 \quad (1.7)$$

The effective Hamaker constant between two particles of the same material is always positive, which means the van der Waals forces between similar particles are always attractive. Hamaker constants can be derived from experiments or from the macroscopic theory. The Hamaker constant value is usually between 10^{-20} to 10^{-19} J ²⁶. When the particles and the dispersion medium have similar Hamaker constants, the effective Hamaker constant will be small ^{1, 2, 25}.

Van der Waals attractive force is the negative of the derivative of the potential energy ^{1, 2, 25}:

$$F_A = - \frac{dV}{dD} \quad (1.8)$$

For two equal-sized particles with small separation distances ($D \ll R$), equations 1.2 and 1.8 yield ^{1, 2, 25}:

$$F_A = - \frac{AR}{12D^2} \quad (1.9)$$

Van der Waals forces are long-range forces that range from interatomic spacings (about 0.2 nm) up to large distances (~ 10 nm) ²⁷⁻²⁹.

Double layer electrostatic interactions:

The other main interaction in colloidal systems is the electrostatic interaction between two charged colloidal particles. The surface of particles is surrounded by an electric double layer which is also known as the electrical diffuse double layer¹³. This double layer is formed by the particle surface charge and its counterions, forming an ionic cloud surrounding the particle¹⁵.

When particles are dispersed in a liquid medium with a high dielectric constant, they develop a surface charge. Based on the Gouy-Chapman model and the Poisson-Boltzmann equation, the electric potential, Ψ is given by^{1,2}:

$$\Delta^2\Psi = -\frac{1}{\varepsilon_0\varepsilon_r}\sum_i n_i^0 z_i e \exp\left(\frac{-z_i e\Psi}{kT}\right) \quad (1.10)$$

Where, ε_0 and ε_r are the permittivity of vacuum and the dielectric constant, respectively. n_i^0 is the bulk concentration of i ions of valency z_i , e is the electronic charge, k is the Boltzmann's constant, and T is the absolute temperature. If we assume a symmetric electrolyte, equation 1.10 becomes^{1,2}:

$$\frac{d^2\Psi}{dx^2} = \frac{2n^0ze}{\varepsilon} \sinh\frac{ze\Psi}{kT} \quad (1.11)$$

When two dissimilar flat double layers are overlapping and the potential in the region between the plates is sufficiently small, the Debye-Hückel approximation can be applied and equation 1.11 then becomes^{1,2}:

$$\frac{d^2\Psi}{dx^2} = \kappa^2\Psi \quad (1.12)$$

Where κ is the Debye-Hückel reciprocal length and is given by²:

$$\kappa = \left[\frac{2n^0z^2e^2}{\varepsilon kT}\right]^{1/2} \quad (1.13)$$

For separation distance of D , solving equation 1.12 using the boundary conditions given by the two potentials Ψ_{01} and Ψ_{02} gives ^{1,2}:

$$\Psi = \Psi_{01} \cosh \kappa x + \left(\frac{\Psi_{02} - \Psi_{01} \cosh \kappa D}{\sinh \kappa D} \right) \sinh \kappa x \quad (1.14)$$

Electrostatic potential energy between two double layers is equal to the change in the free energies when the plates are at distance D and infinity:

$$V_R = \Delta G = G_D - G_\infty \quad (1.15)$$

The free energy of two double layers is given by:

$$G_D = -\frac{1}{2}(\sigma_1 \Psi_{01} + \sigma_2 \Psi_{02}) \quad (1.16)$$

The double layer charge on each plate, σ_1 and σ_2 , is given by:

$$\sigma_1 = -\varepsilon \frac{d\Psi}{dx}, \sigma_2 = +\varepsilon \frac{d\Psi}{dx} \quad (1.17)$$

Using equations 1.14 and 1.17, σ_1 and σ_2 become:

$$\sigma_1 = -\varepsilon \kappa (\Psi_{02} \operatorname{cosech} \kappa D - \Psi_{01} \operatorname{coth} \kappa D) \quad (1.18)$$

$$\sigma_2 = +\varepsilon \kappa (\Psi_{02} \operatorname{coth} \kappa D - \Psi_{01} \operatorname{cosech} \kappa D) \quad (1.19)$$

By combining equations 1.18 and 1.19 with equation 1.16:

$$G_D = \frac{1}{2} \varepsilon \kappa [2\Psi_{01} \Psi_{02} \operatorname{cosech} \kappa D - (\Psi_{01}^2 + \Psi_{02}^2) \operatorname{coth} \kappa D] \quad (1.20)$$

G_∞ can be calculated from equation 1.20 at large separations:

$$G_\infty = -\frac{1}{2} \varepsilon \kappa (\Psi_{01}^2 + \Psi_{02}^2) \quad (1.21)$$

Therefore, the electrostatic repulsive potential, V_R , becomes:

$$V_R = \frac{1}{2} \varepsilon \kappa [(\Psi_{01}^2 + \Psi_{02}^2)(1 - \operatorname{coth} \kappa D) + 2\Psi_{01} \Psi_{02} \operatorname{cosech} \kappa D] \quad (1.22)$$

For two identical spherical particles with radius a , the total electrostatic potential energy is assumed to be the sum of interactions from parallel rings between the particles

(each considered as a flat surface). This assumption is correct when the particles are sufficiently larger than the double layer ².

$$V_R = -\pi a \int_D^\infty V_R(\text{flat plate}) dD \quad (1.23)$$

Substituting equation 1.22 into equation 1.23, V_R becomes:

$$V_R = 2\pi\epsilon a \Psi_0^2 \ln[1 + \exp(-\kappa D)] \quad (1.24)$$

When double layer is very extensive, this equation can be simplified to:

$$V_R = 2\pi\epsilon a \Psi_0^2 \exp(-\kappa D) \quad (1.25)$$

1.4. DLVO THEORY

The two main forces between colloids are the van der Waals attractive force and the electrical repulsive force. Derjaguin, Landau, Verwey, and Overbeek developed a theory (DLVO theory) for the stability of colloidal systems. Based on this theory, the total potential energy of interaction between two colloidal particles (V_T) is the sum of repulsion interactions (V_R) and attraction interactions (V_A) ³⁰:

$$V_T = V_R + V_A \quad (1.26)$$

Van der Waals force dominates at large, and small distances and double-layer force dominates at the intermediate distances. **Figure 1.3** shows the total interaction energies between colloidal particles with different surface potentials. The difference between the repulsive and attractive interactions is the energy barrier between colloids which determines the stability of the colloidal suspension. In $V(I)$, the electrostatic repulsive interactions, $V_R(I)$, are high enough to overcome the van der Waals interactions and result in a repulsive energy maximum. $V_R(2)$, however, is not high enough to overcome the van der Waals interactions ¹.

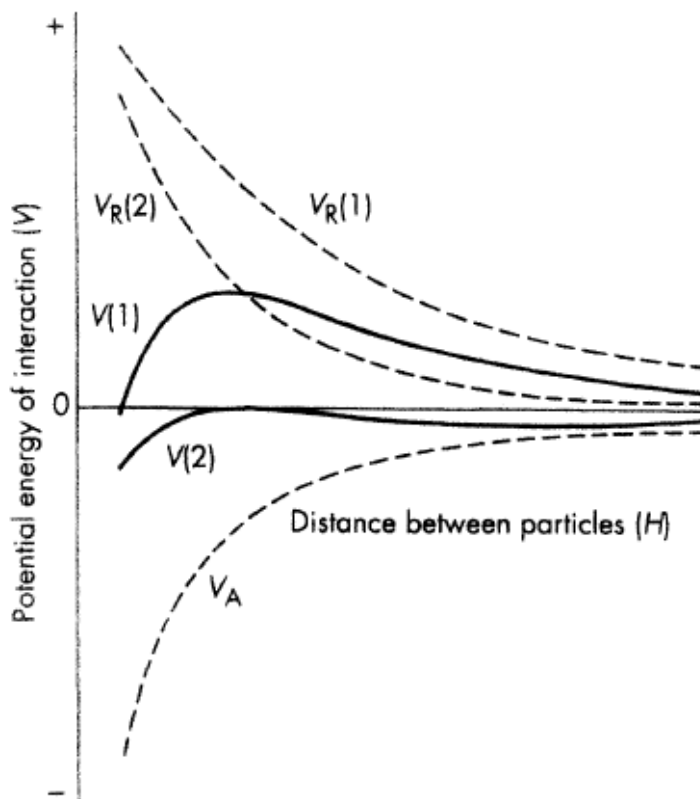


Figure 1.3. Total interaction energy curves, $V(1)$ and $V(2)$, obtained by the summation of an attraction curve, V_A , with different repulsion curves, $V_R(1)$ and $V_R(2)$.¹

1.5. NANOPARTICLE REGULATED COLLOIDAL SYSTEMS

Tuning the dispersion behavior of colloidal microspheres is important in several industrially relevant processes such as coatings, drug carriers, and ceramics. Traditional methods of stabilizing and assembling a suspension typically involve tuning of the effective interactions through charged groups or through grafting short polymer chains onto the colloidal surface³¹⁻³³. These mechanisms, however, pose serious problems in certain situations such as cracking of the crystal upon drying. The attached surfactants on colloidal surfaces may also change the thermal properties of the colloidal particles and solvent^{3, 25, 34}.

In 2001, a new stabilization technique regulated by nanoparticles had been proposed by Tohver et al.^{35, 36}. Their experimental system was composed of neutrally charged silica microparticles and highly charged zirconia nanoparticles. The colloidal suspension was found to be stabilized by using zirconia nanoparticles within a critical nanoparticle concentration range, and gelation was observed outside of this concentration window. They attributed the stabilization mechanism to nanoparticle haloing which is a non-adsorbing nanoparticle layer surrounding the colloidal particles that leads to an effective electrostatic repulsion between colloids to mitigate the inherent van der Waals attraction³⁴.

Minor adsorption of nanoparticles is expected at low nanoparticle volume fractions (10^{-5} to 10^{-3}), but the amount of nanoparticle adsorption dramatically increases with increasing the nanoparticle volume fraction beyond 10^{-3} . In fact, the fundamental mechanism of nanoparticle-regulated stabilization is nanoparticle haloing at low nanoparticle concentrations which transitions to adsorption at higher concentrations. Accordingly, at a nanoparticle volume fraction of around 10^{-3} , where the transition happens, the stabilization can be influenced by both nanoparticle haloing and adsorption. Despite the fact that nanoparticles are capable of stabilizing colloidal suspensions based on either the nanoparticle haloing or adsorption mechanism, it is of great importance to distinguish the working conditions of the stabilization.³⁴

1.6. PREVIOUS STUDIES

Hong and Willing used Atomic Force Microscopy to study the interaction between weakly charged silica surfaces in varying volume fractions of highly charged zirconia

nanoparticles (through 10^{-6} to 10^{-3})⁵. The key feature of their observations was a peak at a separation distance of ~ 2 nm in the force profile measured at a volume fraction of 10^{-5} , which could be attributed to a formation of nanoparticle halo with a 2 nm separation distance from silica surface. Their result was in accordance with Tohver's observation that the haloing distance is roughly equal to the Debye length³⁴.

Besides the original silica-zirconia system, the colloidal stabilization regulated by charged nanoparticles has also been successfully applied to other colloid-nanoparticle binary suspensions³⁷⁻³⁹. Since this stabilization method does not rely on adsorption, it is specifically suitable in applications where using adsorbed species may hinder reactivity or availability of the surface such as in colloidal surface functionalization. Examples of where nanoparticles have been used to increase the stability of colloidal particles in different industrial processes include ceramic processing^{40, 41}, chemical-mechanical polishing⁴², development of paints⁴³, and drilling fluids^{34, 44}.

Ji et al.⁴⁵ and Mckee et al.²² also investigated the use of charged nanoparticles to manipulate the interaction between neutral colloids. They proposed that the stabilization of the binary suspension is caused by sufficient deposition of nanoparticles onto the colloids, leading to an increase in the effective charge density on the colloidal surfaces, and thereby enhancing the electrostatic repulsion between them. This increased repulsion did not vanish upon flushing the nanoparticles out of the system, indicating strong nanoparticle adsorption³⁴. This result challenges the potential use of highly charged nanoparticle as a tool to reversibly tailoring colloidal stability. However, their experiment focused on relatively high nanoparticle volume fractions ($\geq 10^{-3}$)³⁴.

As mentioned above, some researchers have shown that in some of the systems the stabilization mechanism is based on the nanoparticle haloing while other researchers observed strong deposition of nanoparticles in their systems ^{35, 45}. Considering the widespread use of nanoparticles in the stabilization of colloidal particles and the contrary observations in the stabilization mechanism resulting from the different studies, it is very important to understand and determine the exact stabilization mechanism of the colloidal binary systems ³⁴.

He and Willing performed a comprehensive experimental investigation on the interaction between neutral colloidal surfaces in highly charged nanoparticle aqueous solutions ⁴⁶. Their results showed that the silica-zirconia binary suspension system could be stabilized by highly charged nanoparticles at volume fractions ranging from 10^{-5} to 10^{-2} . A subsequent adsorption isotherm study and force modeling showed that at low nanoparticle volume fraction (10^{-5} to 10^{-4}), nanoparticles form a nonadsorbing nanoparticle layer around neutral colloidal particle, which presents as an effective surface charge and produces an electrostatic repulsion that mitigates the inherent van der Waals attraction between them. In this region, there is a minor amount of adsorption, and colloidal stabilization is dominated by nanoparticle haloing. At high nanoparticle volume fractions ($\sim 10^{-2}$) the colloidal surface is significantly occupied by the adsorbing nanoparticles, and instead of nanoparticle haloing, the increased surface charge is primarily induced by nanoparticles that are directly adsorbed onto the silica surfaces. Therefore, adsorption will overcome nanoparticle haloing in this region. There is a transition region around a nanoparticle volume fraction of 10^{-3} , within which the stabilization mechanism can be influenced by both nanoparticle haloing and adsorption ³⁴.

Their study suggests when using highly charged nanoparticles to stabilize colloidal suspensions, the two fundamental mechanisms of nanoparticle haloing, and adsorption are not mutually exclusive. They work across the continuum to regulate the stability of colloidal suspensions over increasing nanoparticle concentrations. Depending on the ultimate application of the colloids, the primary mechanism can be controlled by simply tuning the nanoparticle concentrations ³⁴.

1.7. FORCE PROFILES IN PRESENCE OF NANOPARTICLES

When colloidal particles are placed in a suspension of nanoparticles, other than the van der Waals attractive and electrostatic repulsive interactions between the colloids, another attractive interaction arises between colloids called the depletion interaction. When microparticles are placed in a solution of nanoparticles, and separations distance is less than the diameter of the nanoparticles, nanoparticles are excluded from the gap between the microparticles, which leads to an attractive force equal to the osmotic pressure of the nanoparticles ⁴⁷.

Therefore, in the nanoparticle regulated systems, the total interaction between two microparticles is expressed as the combination of the van der Waals attractive force, electrostatic repulsive force, and depletion force:

$$F_{Total}(D) = F_{vdW} + F_{electro} + F_{depletion} \quad (1.27)$$

For a system of a colloidal particle near a plate, the approximated equations are as follows ³⁴:

$$F_{vdW}(D) = -\frac{AR}{6D^2} \quad (1.28)$$

$$F_{electro}(D) = +\kappa R \epsilon_0 \epsilon_r \pi \Psi_{effective}^2 \exp(-\kappa D) \quad (1.29)$$

$$F_{depletion}(D) = \begin{cases} -2\rho_{\infty}kT\pi \left[a^2 + 2aR - RD - \frac{D^2}{4} \right] & \text{for } 0 \leq D \leq 2a \\ 0 & \text{for } D > 2a \end{cases} \quad (1.30)$$

Where D is the separation distance of the closest approach between the sphere and the plate, R is the radius of the microparticle, and A is the Hamaker constant of silica (0.8×10^{-20} J)⁴⁸. ϵ_0 is the vacuum permittivity, ϵ_r is the dielectric constant, κ is the reciprocal of the Debye length, $\Psi_{effective}$ is zeta potential of the binary mixture, a is the nanoparticle size, ρ_{∞} is the bulk number density, and kT is the thermal energy. The van der Waals attraction between a silica sphere and plate is calculated using the simplified expression of Hamaker when the colloidal sizes are sufficiently large compared to the distance between them²². The electrostatic repulsion is calculated using the Hogg-Healy-Fuerstenau (HHF) formula³⁰, which is well known to calculate the double layer interactions at constant surface potential between dissimilar surfaces and has been utilized to study mechanisms of nanoparticle haloing in several previously reported works^{49, 50}. The depletion force is estimated using Piech and Walz's approximation^{34, 47}.

1.8. OUR WORK

This study aims to investigate the effect of temperature and nanoparticle concentration on the stabilization of binary systems of colloids and nanoparticles under both gravity and microgravity conditions, with possible nanoparticle haloing. Proper nanoparticle haloing systems were prepared to meet NASA safety requirements and were sent to the International Space Station (ISS) for microgravity experiments. Gravity experiments were conducted in several facilities at the University of Louisville. Due to a delay in the NASA experiment timeline, we were not able to compare the gravity results with the results from similar experiments performed onboard the ISS.

We are the first group that has studied the effect of temperature on nanoparticle haloing, which provides a new perspective on the stability of the suspensions with temperature-dependent halo disruption. We have also performed molecular dynamics simulations of the nanoparticle haloing systems using HOOMD-blue to quantify the apparent kinetic barrier and the effective pair interactions between microparticles in the presence of nanoparticle halos. This study helps in the development of future materials where the assembly and structure of colloids are critical.

The rest of this dissertation is divided into five chapters. The second chapter explains the synthesis and characterization of the microparticles for nanoparticle haloing binary systems. The third chapter includes the preparation of the binary systems for NASA microgravity and on earth settling experiments. Temperature shock experiments to measure the impact of the temperature on nanoparticle haloing are discussed in the fourth chapter. Molecular dynamics simulations of the binary systems are presented in chapter five. The conclusion of this work and future directions are examined in the last chapter (chapter six).

CHAPTER 2

MICROPARTICLE SYNTHESIS AND CHARACTERIZATION

2.1. INTRODUCTION

Previous NASA binary samples made from silsesquioxane microparticles (600 nm diameter, $\varphi_{micro} = 10^{-2}$) and varying volume fractions of ZrO₂ nanoparticles (8 nm diameter, $\varphi_{nano} = 10^{-4}, 10^{-3.26}, 10^{-3}$) at pH 1.5 were sent to the ISS so that their aggregation behavior could be observed in the Light Microscopy Module (LMM) under the microgravity environment. The silsesquioxane microparticles were synthesized in another lab in Western Kentucky University with the impression that they are similar to silica in properties. However, ISS microscopy images of the binary systems showed a rapid agglomeration as can be seen in **Figure 2.1**. This was incompatible with previous studies showing a stable colloidal system under the same conditions. Therefore, we needed to further investigate the system and to characterize the silsesquioxane particles in order to understand the reason for the rapid agglomeration of our systems. We also had to define a new binary system with possible nanoparticle haloing for the next ISS experiment.

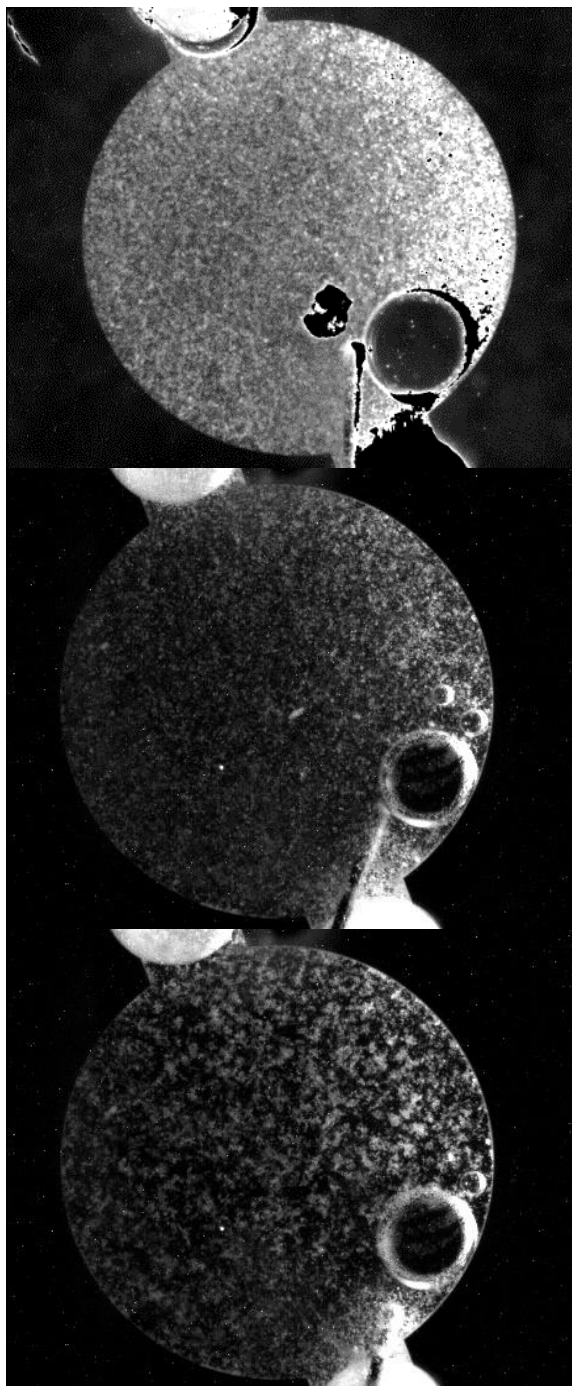


Figure 2.1. Light microscopy module images of binary systems of benzyl chloride-functionalized silsesquioxane with a rhodamine B fluorescent tag (BC-SSQ-RhB) (600 nm diameter) and ZrO_2 nanoparticles (8 nm) at 10x on the ISS at start and over 1.9 and 9 days from top to bottom ($\varphi_{micro} = 1$, $\varphi_{nano} = 10^{-4}$, at pH 1.5).

As will be discussed later in this chapter, zeta potentials results of BC-SSQ microparticles show that their isoelectric point is near pH 4 and particles are highly charged at pH 1.5. Therefore, the previous ISS system which was a binary system of BC-SSQ and ZrO₂ nanoparticles at pH 1.5, is not a favorable system for nanoparticle haloing. As mentioned before, nanoparticle haloing needs a binary mixture possessing both a size and charge asymmetry, in which the microparticles are negligibly charged and nanoparticles are highly charged. But based on the zeta potential results, the previous ISS system is a system with mutually charged microparticles and nanoparticles. The rapid agglomeration in this system shows that the depletion interaction is very high. This system has interesting physics to be studied due to its high size asymmetry. By directly measuring the force of this system with an AFM, we can gain fundamental understanding about the physics of this system. However, an AFM study of this system is beyond the scope of this study and would be a direction for future research.

2.2. MATERIALS AND METHODS

Silsesquioxanes (SSQ) have gained significant attention due to the fact that they can be easily synthesized and further modified with organic or inorganic functionalities⁵¹⁻⁵⁷. Silsesquioxane refers to structures with a ratio of 1.5 of oxygen to silicon atoms resulting in the general formula of RSiO_{1.5}. In this case, the R can represent a hydrogen or an organofunctional group^{58, 59}. Based on the chemistry of the silsesquioxanes with an organic-inorganic composition, their properties are a combination of ceramic-like properties of silica and the soft nature of organic materials⁶⁰. Silsesquioxanes have potential applications as nanoscale fillers in polymer systems for use in adhesives, coatings, composites, and dental fillings^{11,61}. They have also been examined

for semiconducting devices ⁶², fuel cells ⁶³, optical devices ⁶⁴ and sensors ⁶⁵. But there has been limited effort aimed at chemical modifications of the silsesquioxane particles with reactive organic functional groups. Recently, Rathnayake et al. ¹¹ made novel benzyl chloride and benzyl chloride-amine-functionalized silsesquioxane (BC-SSQ, BC-A-SSQ) particles by adopting a modified Stöber method. They also post-functionalized the synthesized particles with a rhodamine B (RhB) fluorescent tag (BC-SSQ-RhB, BC-A-SSQ-RhB). Silsesquioxane with benzyl chloride functionalization is useful for the tailoring and grafting of a wide variety of materials to the surface including polymer ligands and other precursors. The post-functionalization capabilities of these particles are significantly beneficial for numerous applications in colloid chemistry and nanoscience. Due to the nature of the reactive group's functionality which mimics strong dipole-dipole and hydrogen bonding interactions, a colloidal suspension of these particles can assemble into monolayers and hollow colloidosomes on a variety of polymer-coated substrates to create 3D colloidal assemblies ^{11, 66}. Considering the applications of silsesquioxanes in adhesives, coatings, and semiconductors, it is very important to determine a wide range of properties for these particles such as their charge, density, and porosity along with their morphology.

For our work, BC-SSQ, BC-A-SSQ particles were synthesized based on the Rathnayake et al. method ¹¹ by adapting a modified Stöber method. The synthesized microparticles were then post-functionalized with a Rhodamine-B (RhB) fluorescent tag (BC-SSQ-RhB, BC-A-SSQ-RhB). The post-functionalization capabilities of these particles are significantly beneficial for imaging in confocal microscopy.

While the compounds are similar in nature, the properties of silica and silsesquioxane are very different, but little is known about these differences. The synthesized silsesquioxane particles were characterized by a variety of physical and chemical methods. The synthesized particles are amorphous and nonporous in nature and are less dense than silica. While silsesquioxane and silica have some similar physical properties from their siloxane core, the organic functional group of silsesquioxane and the one-half oxygen difference in its structure impact many other properties of these particles like their charging behavior in liquids. These differences not only allow for the ease of surface modification as compared to that necessary to modify silica but also allow for the use in a variety of colloidal systems that due to pH or electrolyte concentrations may not be suitable for silica particles.

2.2.1. MATERIALS

Para-(chloromethyl)phenyltrimethoxysilane was purchased from Gelest Inc. Potassium carbonate (ACS reagent) was purchased from Fisher Scientific. 3-Aminopropyltriethoxysilane (3-APT), anhydrous ethanol (200 proof), ammonium hydroxide (28%), and rhodamine B carboxylic acid were purchased from VWR International.

2.2.2. PARTICLE SYNTHESIS

For synthesizing BC-SSQ particles, 10 mL of anhydrous ethanol and 4 mL of 28% ammonium hydroxide were mixed on a magnetic stirrer for 5 min. Then, 1.8 mL of benzyl chloride trimethoxysilane was added to the reaction at a rate of 0.08 mL/min and was

allowed to stir for 18 h. The particles were separated by centrifuging at 3000 rpm for 20 min. Then, the particles were washed multiple times with ethanol followed by distilled water to remove any impurities. Finally, the particles were dried under the hood for 48 h to yield the BCSSQ particles.

The materials used for the synthesis of BC-SSQ were the same as those that Rathnayake et al.¹¹ used. However, the silane solution (95% purity) that we received was not clear and had a yellowish color. We could not synthesize BC-SSQ particles using the exact amounts of materials that Rathnayake et al.¹¹ reported, which could be due to the different impurities of the silane solution. Therefore, we had to modify the reactants and test different amounts of ammonium hydroxide and silane to get the spherical microparticles. The proper amount of ammonium hydroxide that resulted in spherical microparticles structures was 4 ml in our lab, which is 400% larger than the amount reported by Rathnayake et al.¹¹ Lower amounts of ammonium hydroxide resulted in polymerized structures.

For synthesizing BC-A-SSQ particles, 65 mL of anhydrous ethanol and 3.5 mL of 28% ammonium hydroxide were mixed on a magnetic stirrer for 5 min. Then, 2 mL of 3-APT silane was added to the flask dropwise followed immediately by 1 mL of benzyl chloride trimethoxysilane at a rate of 0.08 mL/min and was allowed to stir for 18 h. Then, the BC-A-SSQ particles were washed and dried in the same way as the BC-SSQ particles.

In order to functionalize the as-synthesized particles with rhodamine B, 500 mg of particles was dispersed in 30 mL of anhydrous ethanol and was mixed on a magnetic stirrer until the particles were dispersed completely. Then, 79 mg of potassium carbonate was added followed by 230 mg of rhodamine B and was allowed to stir for 18 h. In order to

keep the reaction away from visible light, the reaction flask was covered with aluminum foil. The same procedure was used to wash and dry the particles.

Tagging the BC-SSQ and BC-A-SSQ particles with RhB is the last step after synthesizing the microparticles. Since BC-SSQ and BC-A-SSQ particles are not very porous (it will be shown later in this chapter), RhB is not embedded inside the microparticles.

2.2.3. STRUCTURE, MORPHOLOGY, AND SIZE

In this work, the morphology of particles was investigated using a Zeiss Auriga Crossbeam FIB-FESEM scanning electron microscope and a Zeiss Orion helium ion microscope. A TESCAN scanning electron microscope (SEM) equipped with energy-dispersive X-ray spectroscopy (EDX) was used for the surface analysis of the particles. X-ray diffraction (XRD) measurements were carried out on a Bruker D8 Discover diffractometer. Patterns were recorded over the range from 10 to 90° (2 θ) in steps of 0.02° with a scan speed of 2 s at each step. A Brookhaven 90Plus-Zeta particle size analyzer was used to measure the average sizes of the particles and their size distributions.

2.2.4. ZETA POTENTIAL

The Brookhaven 90Plus-Zeta particle size analyzer was used to measure the zeta potential of the colloidal particles as well. The zeta potential of the particles was measured at 0.01 vol% concentration of particles in solutions with pH ranging from 3 to 11. Acidic and basic solutions were made by adding the proper amount of nitric acid or potassium hydroxide to DI water. Each sample was sonicated and well-suspended in the pH solution

before zeta potential measurements. These measurements also revealed the isoelectric point of the particles. A Nikon Eclipse Ti inverted microscope was then used to observe any agglomerates that formed during settling.

2.2.5. DENSITY

Particle density is required for sedimentation analysis or calculations involving volumes or mass of particles. The particle density of different SSQ particles was measured by a AccuPyc II 1340 Pycnometer which is a fully automatic gas displacement pycnometer. The particles were first dried in the desiccator to obtain true sample mass and to avoid the distorting effect of water vapor on the volume measurement. Mass was determined by precisely weighing the particles on an analytical balance. Knowing the mass of the particles, the density was measured by the pycnometer using a 1.0-cm³ cup.

2.2.6. SPECIFIC SURFACE AREA

After drying the particles in a desiccator, the particles were degassed using a SmartPrep degasser to remove any gas trapped in the pores and on the other surfaces of the particles. To degas, the particles were heated to 120 °C and degassed for 2 h. After degassing, a TriStar 3000 gas adsorption analyzer was used to measure the surface area and porosity of the particles by measuring gas (N₂) adsorption.

2.3. RESULTS AND DISCUSSION

2.3.1. MORPHOLOGY

In the literature, silsesquioxanes have been reported to have a variety of different structures, including a random structure, ladder structure, cage structure, and partial cage structure^{67, 68}.

The X-ray diffraction patterns of the as-synthesized BCSSQ and BC-A-SSQ microparticles are shown in **Figure 2.2**. The XRD spectral traces show that a broad peak is present at $2\theta = 10\text{--}30^\circ$ for both particles, verifying them to be of amorphous structure^{69, 70}.

HIM and SEM images of the BC-SSQ and BC-A-SSQ particles are shown in **Figure 2.3** and **Figure 2.4**. These images are taken after 4 h of reaction. As it is clearly seen in these pictures, both particles are mostly spherical with a smooth surface which is in agreement with N. Neerudu's results¹¹.

In **Table 2.1**, the EDX descriptive statistics of the average amount of different elements in the surface layer of the BCSSQ and BC-A-SSQ particles are presented. One may notice that the chlorine amount in the surface layer is much higher in the BC-SSQ particles compared to that of the BC-A-SSQ particles. This is expected as the amine functionalization will cover and replace many of the exposed benzyl chloride groups on the particle surface.

Particle size measurements by the DLS method, as shown by volume in **Figure 2.5**, showed the BC-SSQ and BC-A-SSQ particles with sizes in the range of 600–2700 nm and 1400–3600 nm, respectively. The median size was determined for the BC-SSQ particles as 1200 nm and for BC-A-SSQ as 2300 nm.

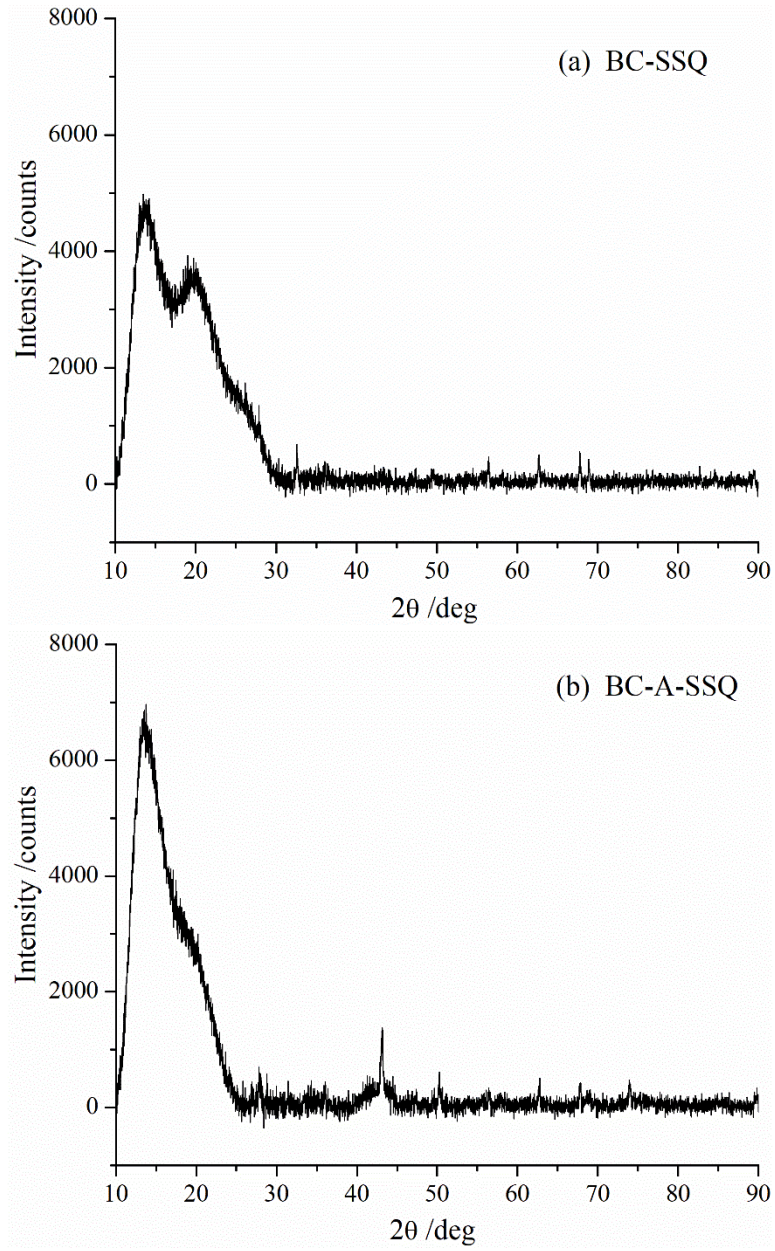


Figure 2.2. XRD patterns for amorphous a BC-SSQ and b BC-A-SSQ ⁷¹

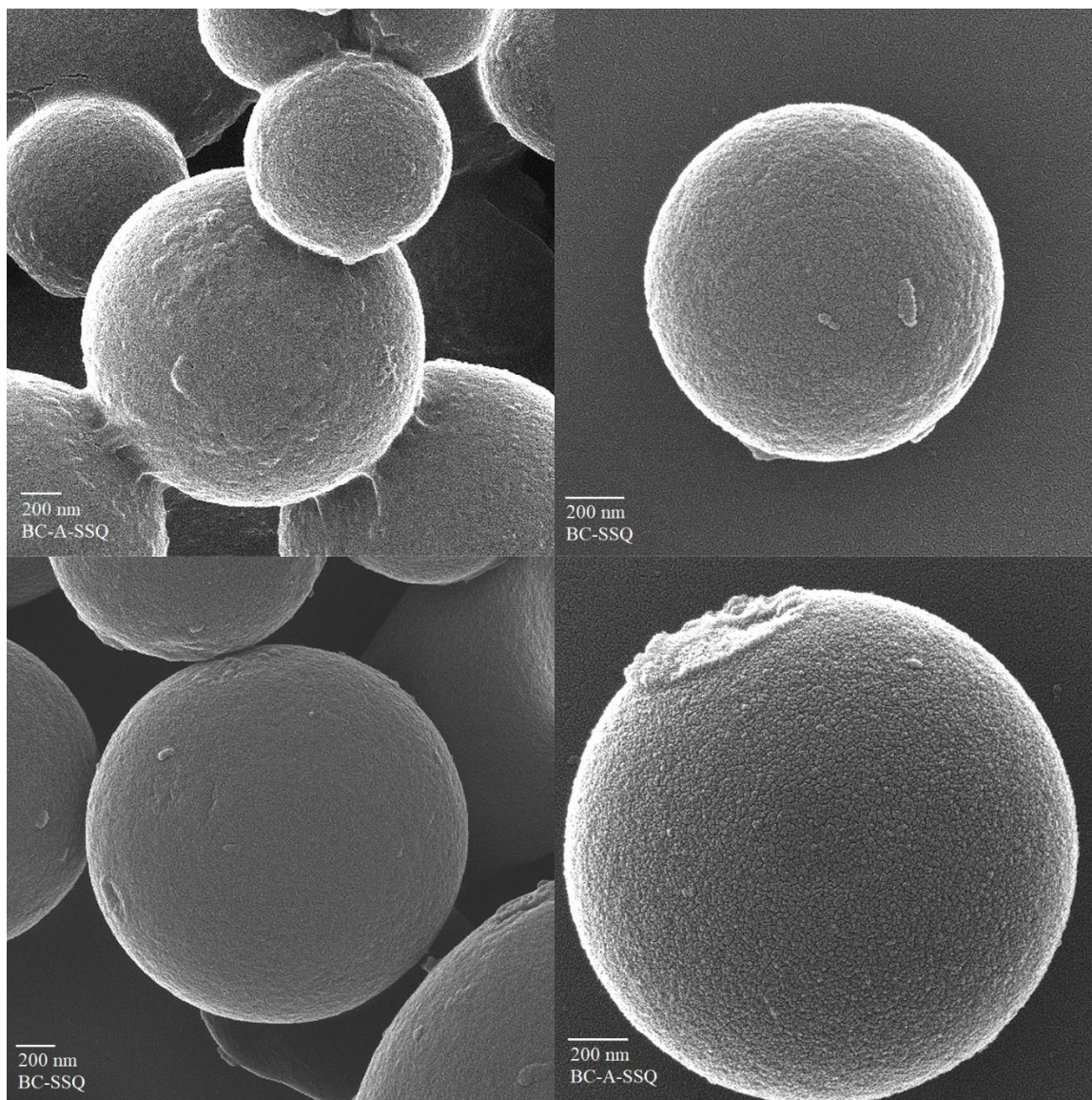


Figure 2.3. HIM images of BC-SSQ and BC-A-SSQ ⁷¹

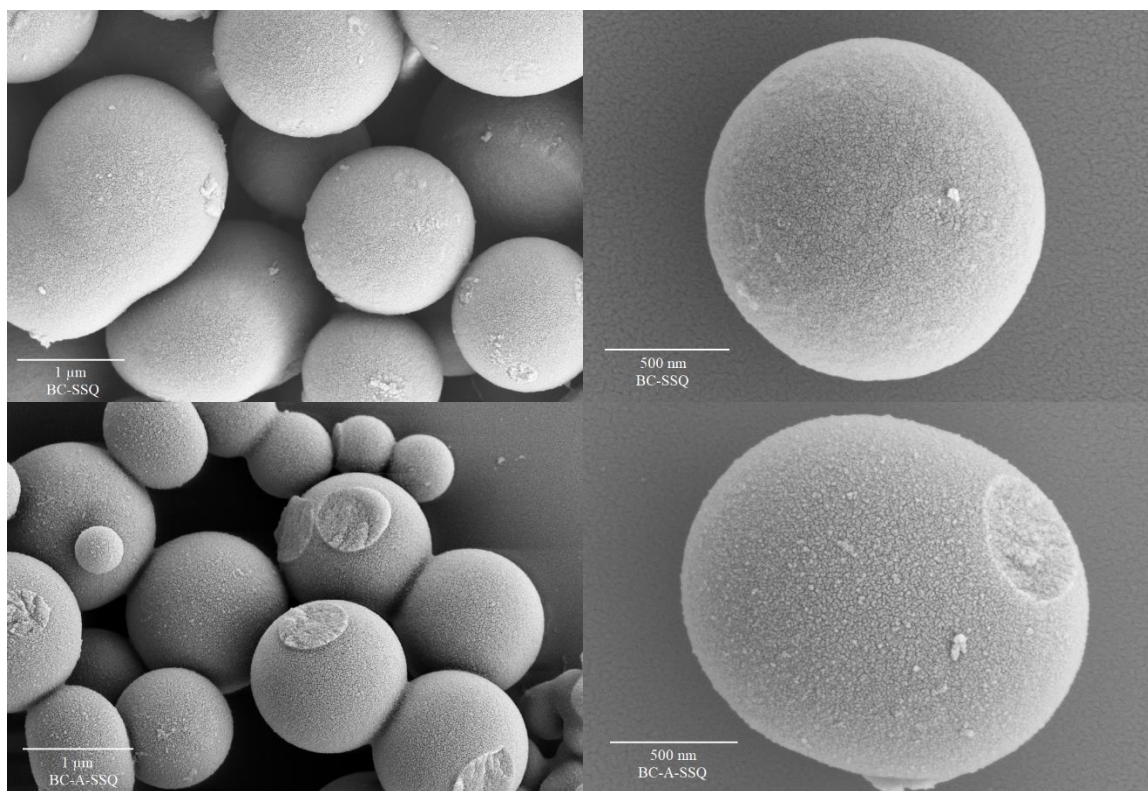


Figure 2.4. SEM images of BC-SSQ and BC-A-SSQ ⁷¹

Table 2.1. Descriptive statistics of the amount of different elements in the surface layer of the BC-SSQ and BC-A-SSQ particles ⁷¹

Element	Atomic %		Ratios to Si	
	BC-SSQ	BC-A-SSQ	BC-SSQ	BC-A-SSQ
Si	27.77	26.94	1	1
O	40.52	43.33	1.46	1.61
Cl	31.71	17.83	1.14	0.66
N	0	11.90	0	0.44

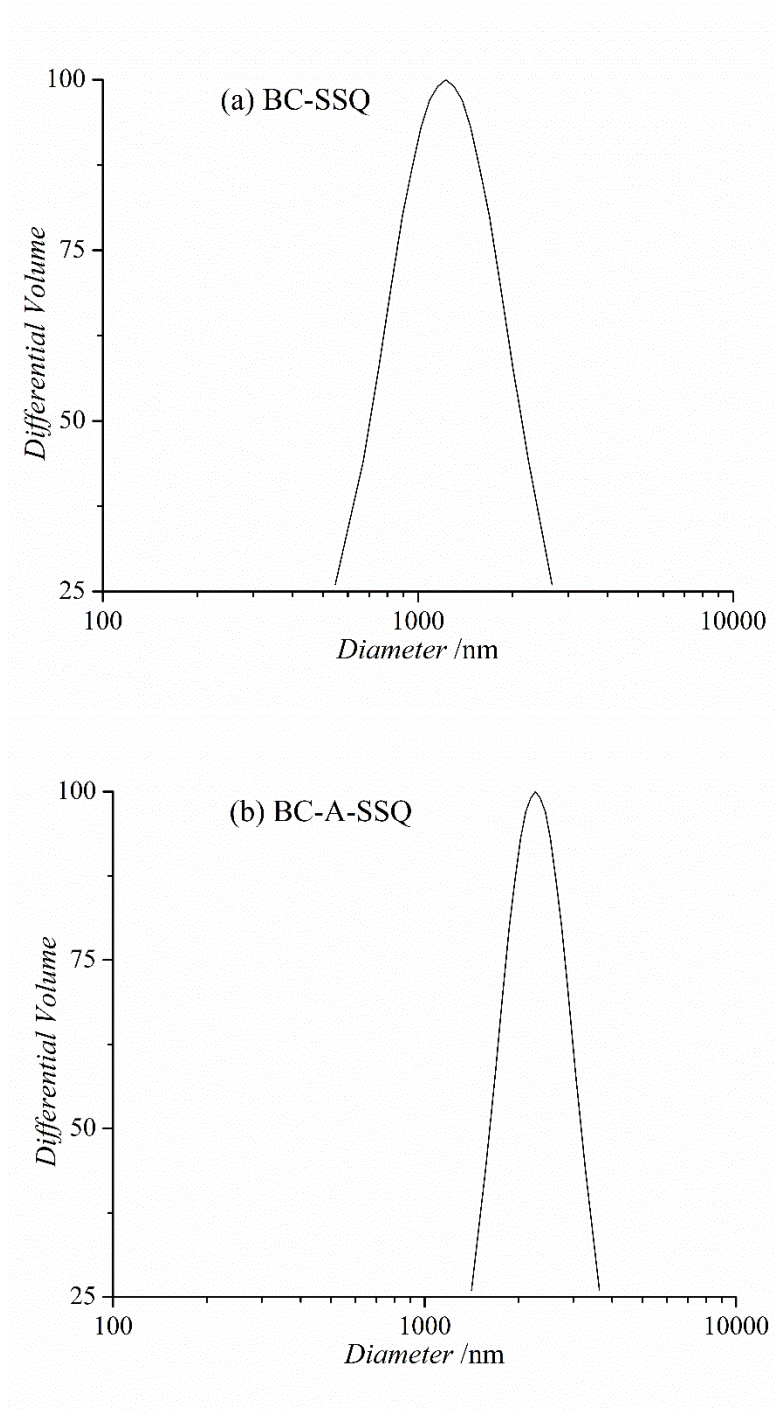


Figure 2.5. Lognormal differential distributions of particle sizes weighted by volume for a BC-SSC and b BC-A-SSQ particles ⁷¹

2.3.2. ZETA POTENTIAL

Figure 2.6 shows zeta potential measurements as a function of pH for the BC-SSQ and BC-SSQ particles. It is noted that both particles are positively charged at lower acidic pH while the bifunctional BC-A-SSQ particles have a higher charge at a lower pH. This confirms the presence of amino groups in the BC-A-SSQ particle surface in their protonated form. At a higher pH, that is, towards the basic end of the scale, the value of the zeta potential changes from positive to negative. The isoelectric point of the BCSSQ and BC-A-SSQ was found to be near pH 4 and 7, respectively, while the isoelectric point of silica has been reported to be between pH 1.7 and pH 2.5^{36,72}. This makes SSQ favorable for conditions where highly acidic solutions cannot be used due to material or safety concerns. It should also be noted that RhB functionalization did not significantly affect the charge of the particles⁷³. This is extremely valuable for imaging in confocal microscopy because one can easily fluorescently label these SSQ particles and study the structure of agglomerates without changing their isoelectric point.

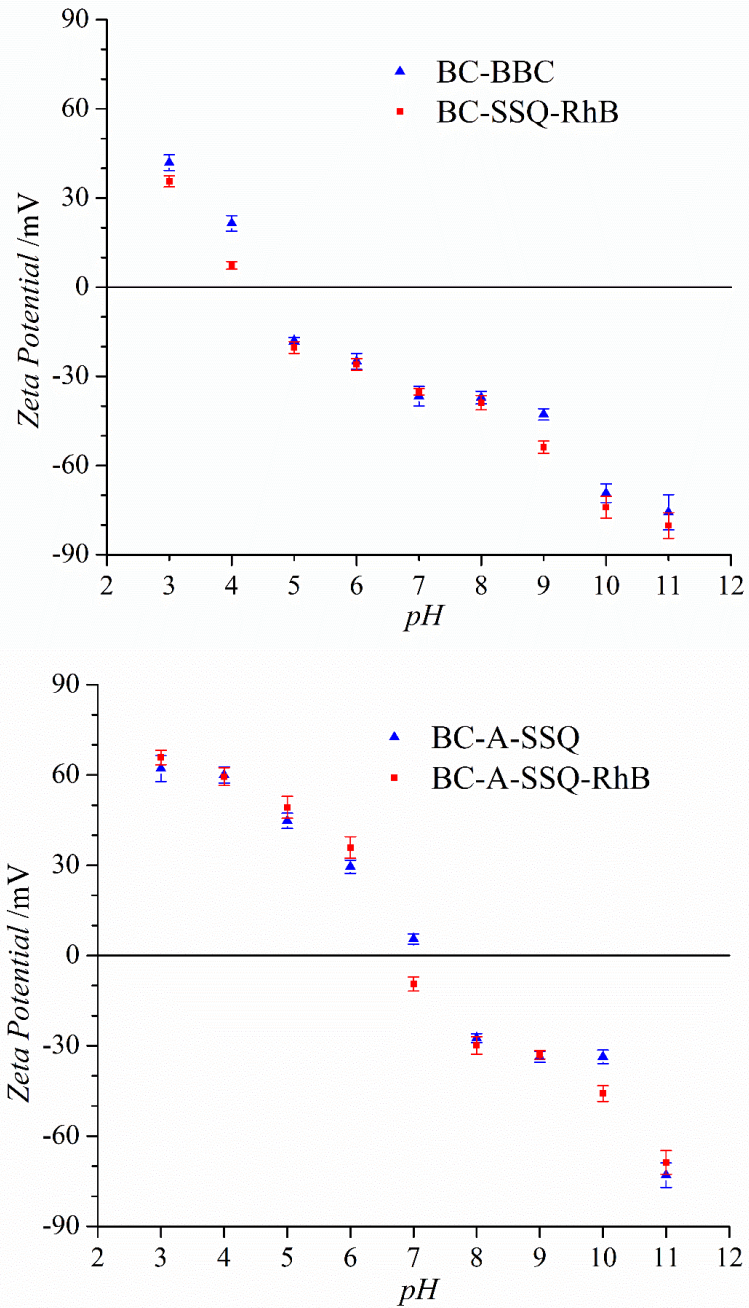


Figure 2.6. Plot of the effective zeta potential (ξ) of the BC-SSQ, BC-SSQ-RhB, BC-A-SSQ, and BC-A-SSQ-RhB microparticles as a function of pH ⁷¹

Figure 2.7 shows the microscope images of the BC-SSQ samples at pH 3 and 4 and the isoelectric point. As it can be seen in this figure, by decreasing the pH from isoelectric point to 3 which increases the electric charge of the particles, we observe that

the particles are more dispersed during settling. These images were analyzed using ImageJ. For this purpose, the images were converted into 8-bit, and then, an Iso-Data algorithm threshold was set to differentiate the particles from the backdrop⁷⁴. A binary close operation and a watershed separation were performed on the thresholded images. The watershed function visually separated the semi-agglomerated particles, and ImageJ output the particle count, total blob area, and average blob size which are listed in Table 2. As the pH increases, the number of aggregates, total blob area, and average blob size increase accordingly. This is consistent with the lower stability and higher tendency of the particles to agglomerate at their isoelectric point. Such behavior for the silica particles would not be observed unless the pH was less than 2. It should be noted that this is a result of the BC-SSQ particles taking on a strong positive electric charge below pH values of 4, unlike the silica particles that would not take on a positive charge unless the pH value is less than 2.

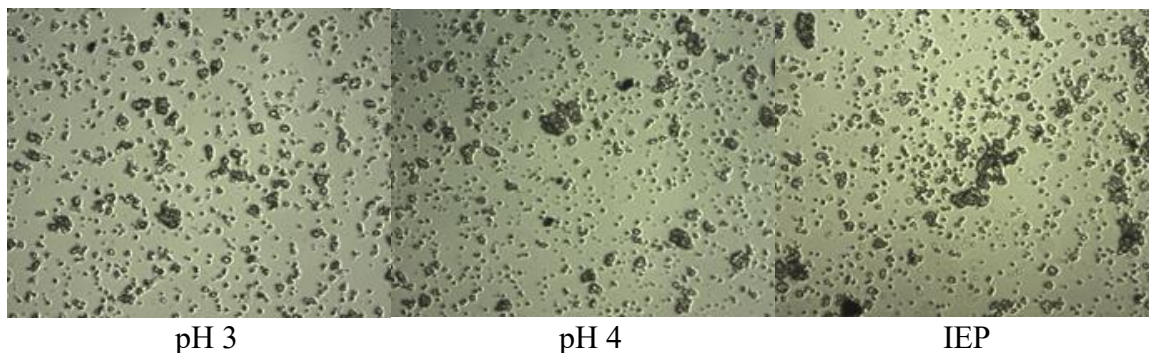


Figure 2.7. Images of the BC-SSQ particles at pH 3 and 4 and isoelectric point after 4 h using inverted microscopy (20x)⁷¹

Table 2.2. ImageJ analysis data of the BC-SSQ samples ⁷¹

pH	Count	Total blob area	Average blob size
2	337	4921	13.635
3	347	6063	17.473
IEP	394	8967	22.759

2.3.3. DENSITY

The measured particle density for BC-SSQ and BC-A-SSQ was 1.68 ± 0.05 and 1.48 ± 0.04 g/cm³ at 22 °C, respectively. This is lower than the density of silica which is reported to be 2.196 g/cm³ ⁷⁵. This result is not unexpected as the structure of the silsesquioxane is highly amorphous and has a random cage structure which is more open than the structure of amorphous silica.

2.3.4. SPECIFIC SURFACE AREA

The BET surface area (S_{BET}) of the BC-SSQ and BC-A-SSQ particles with sizes of 1.2 μm and 2.3 μm was 3.83 ± 0.07 m²/g and 4.72 ± 0.04 m²/g, respectively. The average pore width of the BC-SSQ and BC-A-SSQ particles was 7.97 nm and 8.76 nm, respectively. **Figure 2.8** shows the physisorption and pore size distribution of the particles. It can be seen that both the BCSSQ and BC-A-SSQ particles exhibit a typical type II isotherm ⁷⁶. Considering the size of the pores and type II isotherms, both types of the particles possess a nonporous structure ^{76, 77}. The gradual curvature and less distinctive point B indicate a significant amount of overlap of monolayer coverage and the onset of

multilayer adsorption. The thickness of the adsorbed multilayer generally appears to increase without limit when $P/P_0=1$.

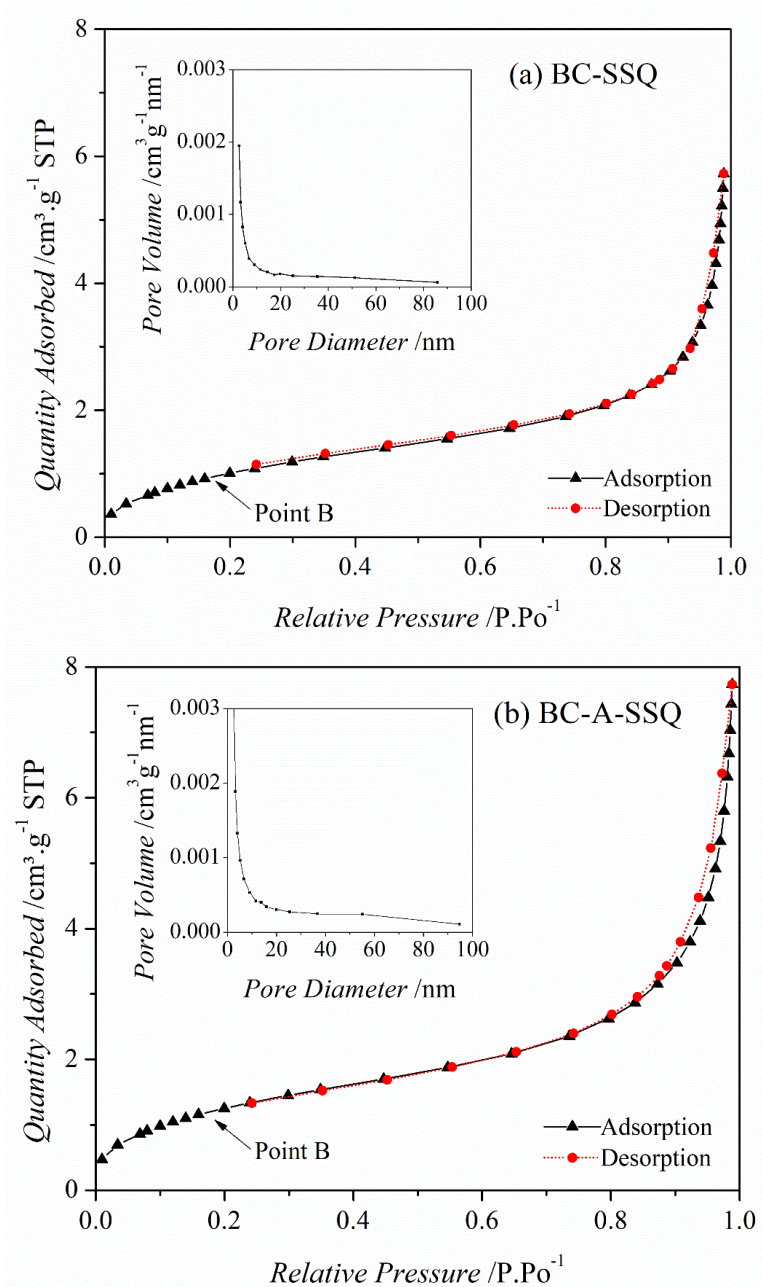


Figure 2.8. N_2 adsorption-desorption isotherm and pore size distribution of a BC-SSQ and b BC-A-SSQ⁷¹

2.3.5. GENERAL OVERALL STRUCTURE

It was also shown that the silsesquioxane particles were less dense than silica. Compared to silica, the potential colloidal stability of silsesquioxane was different due to the difference in the structure and surface charges. Benzyl chloride and amine functionalization of different silsesquioxane particles significantly affected the charge of the particles. The isoelectric points of all four types of the silsesquioxane particles were significantly higher than the isoelectric point of silica. These differences may make these particles more viable in applications where an isoelectric point closer to a neutral pH or a lower density particle is necessary ⁷¹.

Silsesquioxane is most often treated the same as silica. But in this study, it was shown that although silsesquioxane and silica have a number of similarities in their physical properties such as thermal stability and rigidity which result from their siloxane core, the one-half oxygen difference in the silsesquioxane structure along with its organic functional groups significantly impacts many other properties of these particles. The more open structure of silsesquioxane makes it less dense when compared to silica. The difference in the number of oxygen molecules, as well as the type of the functional groups in the structure of the silsesquioxane particles as compared to the silica particles, changes the overall charge of the particles in the solution and results in a significantly higher isoelectric point. The silsesquioxane particles can be positively charged in a higher range of pH while silica is almost always negatively charged due to its low isoelectric point. Charging behavior of colloids impacts the stability of the suspension and is very important for designing a particular colloidal suspension based on the desired properties of that suspension. The post-functionalization capabilities of silsesquioxanes, based on both silane

and halogen chemistry, are also beneficial for numerous applications in colloid science and ultimately give them a wider range of application when compared to silica ⁷¹.

2.4. CONCLUSION

Synthesized microparticles were characterized in order to identify the properties that are required for preparation and sedimentation analysis of the nanoparticle haloing colloidal suspensions. The characterization results showed that both the BC-SSQ and BC-A-SSQ particles were spherical with a smooth surface. The XRD results showed that both particles had an amorphous structure. The isoelectric point of the BC-SSQ and BC-A-SSQ were near pH 4 and 7. This makes SSQ favorable for conditions where highly acidic solutions cannot be used due to material or safety concerns. Density of BC-SSQ and BC-A-SSQ was 1.68 ± 0.05 and 1.48 ± 0.04 g/cm³ at 22 °C, respectively. Both BC-SSQ and BC-A-SSQ were nonporous with an average pore width of 7.97 nm and 8.76 nm and BET surface area of 3.83 ± 0.07 m²/g and 4.72 ± 0.04 m²/g, respectively ⁷¹.

Based on the characterization results, both BC-SSQ and BC-A-SSQ microparticles could be used for the nanoparticle haloing systems. Gravity settling experiments which are discussed in the next chapter were performed in order to determine the most appropriate microparticles (BC-SSQ or BC-ASSQ) for the next ISS experiment.

CHAPTER 3

GRAVITY SETTLING OF NANOPARTICLE HALOING SYSTEMS

3.1. INTRODUCTION

Gravity settling is a convenient method to determine the equation of state of a colloidal suspension in order to understand the nature of metastable phases⁷⁸. One of the essential factors in gravity settling of interacting colloids is the velocity at which a suspension coagulates. It can be characterized using the stability ratio, which measures how effective the potential barrier is in preventing particle coagulation. Stability ratio (W) is given by²:

$$W = \frac{\text{Number of collisions between particles}}{\text{Number of collisions that result in coagulation}} \quad (3.1)$$

In the absence of a potential barrier, the rate of coagulation is limited by the diffusion of the particles towards one another, a phenomenon which is known as fast or rapid coagulation (R_f). When there is a potential barrier between particles, then the coagulation rate will be slower, and the rate of slow coagulation (R_s) can be defined by the simple theoretical expression of²:

$$R_s = \frac{R_f}{W} \quad (3.2)$$

First, we would assume a certain particle with radius a to be at the center and other particles diffuse towards that particle based on Brownian motion ⁷⁹. The flux of particles whose centers pass through every sphere of radius r surrounding the central particle, and eventually come into contact with it, is given by the Fick's Law ^{2, 79}:

$$J = 4\pi D r^2 \frac{dv}{dr} \quad (3.3)$$

D is the diffusion coefficient ($D=D_1+D_2$) and v is the particle concentration. Solving equation 3.3 using the boundary conditions given by the bulk particle concentration (v_0) gives ²:

$$R_f = -\frac{dv}{dt} = \frac{1}{2} \times J \times v_0 = 4\pi D R_{11} v_0^2 \quad (3.4)$$

Where R_{11} is the collision radius between individual particles and is $\sim 2a$. This equation is valid if all the particles have the same size and if the central particle also undergoes Brownian motion. Rapid coagulation rates can be calculated using this equation for early stages of coagulation and before the formation of triplets.

Rapid coagulation rate can be determined by the characteristic coagulation time (τ) which is the time required for the number of particles to be reduced to half of its initial value ⁸⁰:

$$\tau = -\frac{v}{dv/dt} = \frac{1}{8\pi D a v_0} \quad (3.5)$$

If τ values are less than a second, it means that the suspension is strongly unstable, but large values in order of several days or even years, means that the suspension is relatively stable ².

By substituting D from the Einstein and Stokes equations where $D=kT/B$ and $B=6\pi\eta r$ (η is the viscosity of the fluid), τ becomes ^{2, 81}:

$$\tau = \frac{3\eta}{4kTv_0} \quad (3.6)$$

Substituting the values of D for water dispersion media, η viscosity of water at room temperature, equation 3.6 gives ²:

$$\tau \cong \frac{2 \times 10^{11}}{v_0} \text{ seconds} \quad (3.7)$$

As shown in the above equation, rapid coagulation time depends on the suspension concentration. Yet, in a slow coagulation process, the potential energy barrier has a significant influence on the stability of the system.

In order to expand the number of particles in an aggregate, we assume that two aggregates with i and j number of particles collide and develop an aggregate with k number of particles where $k = i + j$. Based on equation 3.4, the rate of collision between aggregates i and j is ²:

$$R_{ij} = 4\pi D_{ij} R_i v_i v_j \quad (3.8)$$

Where $D_{ij} = D_i + D_j$ and is the mutual diffusion coefficient of aggregates i and j .

In general, we assume the number of i -fold particles to be v_i (v_1 :primary, v_2 :binary).

The number of k -fold particles is given by ²:

$$\frac{dv_k}{dt} = \frac{1}{2} \sum_{i=1}^{j=k-1} 4\pi D_{ij} R_{ij} v_i v_j - v_k \sum_{i=1}^{\infty} 4\pi D_{ik} R_{ik} v_i \quad (3.9)$$

If the radii of aggregates i and j are a_i and a_j , R_{ij} will be $\cong a_i + a_j$, and based on Smoluchowski, for the conditions that the aggregates radii are not widely different, equation 3.9 simplifies to ^{2,3,82}:

$$v_k = \frac{v_0 (t/\tau)^{k-1}}{(1+t/\tau)^{k+1}} \quad (3.10)$$

This equation can be used to calculate the number of aggregates of different sizes (k -particle aggregates) in rapid coagulation conditions and as a function of time. This

equation is based on the condition where there are no attractive or repulsive interactions between the particles.

When there is a potential barrier between particles that is larger than kT , the rate of aggregation may decrease by an order of magnitude. A coagulation barrier is similar to an activation energy barrier during a chemical reaction. These two phenomena, however, differ significantly. Molecule collisions and bond rearrangements in a chemical reaction happen on a time scale of picoseconds. Although surrounding molecules may indirectly influence interactions between reacting molecules, activation energy is mostly determined by the distortion that the reacting molecules must undergo for the reaction to take place. The molecules can overcome the activation barrier if they have sufficient energy and channel it in the right direction ^{2, 83}.

If two colloidal particles have sufficient mutual kinetic energy to overcome the potential energy barrier that separates them, coagulation is likely to occur. However, this assumption is insufficient since a particle with such a high amount of energy would lose the energy in friction before passing through the barrier ².

When the distance between particles is less than 100 nm, the particles' double layers will start to overlap and that is when the particles experience the barrier. As a result of this potential barrier, particles are more likely to move in one direction than the other.

Slow coagulation depends on the barrier height and the rate of coagulation in the presence of a potential barrier decreases by an amount equal to the stability ratio W ^{2, 3}:

$$k_s = \frac{k_f}{W} \quad (3.11)$$

Where k_s and k_f are the rate constants for slow and fast coagulation, respectively.

Solving equation 3.3 with considering the force field and assuming the steady state conditions gives ²:

$$J = 4\pi D r^2 \left(2D \frac{dv}{dr} + \frac{v}{B} \frac{dV_T}{dr} \right) \quad (3.12)$$

The second term in this equation is the product of particle concentration and the mutual particle velocity as dedicated by the force field. Using the appropriate boundary conditions, the flux in slow coagulation becomes^{2, 25}:

$$J_s = \frac{8\pi D v_0}{\int_{2a}^{\infty} \exp\left(\frac{V_T}{kT}\right) dr / r^2} \quad (3.13)$$

And W is given by ^{2, 25, 84}:

$$W = J_f / J_s = 2a \int_{2a}^{\infty} \exp\left(\frac{V_T}{kT}\right) dr / r^2 \quad (3.14)$$

The sediments from a rapid coagulation have a very loose and open structure (high volume-low density sediment) due to the rapid settling of the aggregates. However, the rate of aggregate formation is slower in slow coagulation and the aggregates structures are more compact (low volume-high density sediment).

The degree of openness in an aggregate can be described using the fractal dimension, d_F . The mass of aggregates is given by ⁸⁵:

$$Mass \propto (Size)^{d_F} \quad (3.15)$$

More compact sediments have a higher d_F and diffusion-based aggregates with loose structures have a lower d_F . Perfectly formed closed packed aggregates have a d_F of 3. d_F values for denser aggregates are in the range of 2 to 3, while for open aggregates they are below 2.

Brownian particles attain a certain velocity under an external field, a process known as sedimentation. Particles will settle under gravity which is the most common external

field. The other force that affects the sedimentation of the particles is the drag force which is due to the particles motion through the dispersion medium and resists the fall of the particles. Since the sedimentation velocity is influenced by the viscosity of the dispersion medium and also particle mass and size, a measurement of the sedimentation velocity can be used to characterize the Brownian particles ⁸⁶.

The settling velocity of solid particles with a density ρ_s and radius r in a liquid of viscosity η and density ρ is affected by hindering effects. These are increased drag caused by the proximity of particles and the upflow of liquid as it is displaced by the descending particles. According to Stokes's law, the drag force rising due to resistance to fall equals $6\pi r\eta V_0$. The gravitational force which is acting downward is given by $\frac{4}{3}\pi(\rho_s - \rho)r^3g$, where g is the acceleration due to gravity. When the acceleration of the fall is constant, known as the terminal velocity, the forces upward and downward are in balance. Therefore, the settling velocity of an isolated particle, V_0 , is given by ^{6, 8}:

$$V_0 = \frac{2(\rho_s - \rho)r^2g}{9\eta} \quad (3.16)$$

Many experiments have shown that particle settling rates are lower at higher concentrations, which is normally calculated by using the semi empirical Richardson and Zaki equation. In fact, the settling velocity, V_{micro} , for a concentrated suspension with a volume fraction of ϕ_{micro} , is affected by hydrodynamic interactions with neighboring particles. It can be calculated using the Richardson-Zaki equation^{87, 88}:

$$V_{micro} = V_0(1 - \phi_{micro})^n \quad (3.17)$$

Where n is a power law exponent ($n=4.65$). The experimental microsphere settling velocity, V , is measured by tracking the interface that separates the clear and cloudy

solutions^{6,8}. Finally, the sediment volume fraction ($\varphi_{\text{sediment}}$) is calculated by measuring the final sediment height over a long period⁶.

3.2. METHODS

As was discussed in the previous chapter, although silsesquioxane and silica have a number of similarities in their physical properties, such as thermal stability and rigidity, which result from their siloxane core, the one-half oxygen difference in the silsesquioxane structure along with its organic functional groups significantly impact many other properties of these particles like their charging behavior in liquids. These differences not only allow for the ease of surface modification as compared to that necessary to modify silica but also the use in a variety of colloidal systems that due to pH or electrolyte concentrations may not be suitable for silica particles.

As was mentioned before, NASA does not let highly acidic solutions be used on ISS due to material and safety concerns. By using silsesquioxane, which had a higher isoelectric point compared to silica, we were able to meet the required level of safety for the NASA experiments.

Synthesized colloidal microparticles (BC-SSQ, BC-A-SSQ) and commercial nanoparticles (ZrO_2 , AlOOH , SiO_2) were tested for the nanoparticle haloing systems. All nanoparticle haloing systems had the same microparticle concentration of 1.0 %vol ($\varphi_{\text{micro}} = 10^{-2}$) with different nanoparticle concentrations of 0.01%, 0.055%, and 0.1 %vol ($\varphi_{\text{nano}} = 10^{-4}, 10^{-3.26}, 10^{-3}$).

3.2.1. SUSPENSION PREPARATION

Different pH solutions (pH 2 to 8) were prepared by adjusting the pH of deionized water by adding the proper amount of nitric acid (42° Be/Technical, Fisher Scientific) or potassium hydroxide (Reagent Grade, Fisher Scientific) to DI water. Aqueous binary suspensions were prepared by first adding an appropriate volume fraction ($\phi_{\text{nano}} = 10^{-4}$, $10^{-3.26}$, 10^{-3}) of different nanoparticles (5-20nm ZrO₂ (AC), NYACOL; 20 nm SiO₂, 6808NM SkySpring Nanomaterials; 10-20 nm AlOOH_xH₂O, SkySpring Nanomaterials) to the appropriate pH solution followed by 2.5 minutes ultrasonication (model Q500 QSONICA). An appropriate mass of BC-SSQ microparticles ($\phi_{\text{micro}} = 10^{-2}$) was then added, followed by 2.5 minutes of ultrasonication. The ultrasonicated suspensions were then vortexed for 10 seconds and followed by another 2.5 minutes of ultrasonication. Each sonication step consisted of 2.5 minutes pulsed at a 1 second on/off sequence at 20 kHz.

3.2.2. GRAVITY SETTLING OF THE BINARY SYSTEMS

Suspensions with different microparticles (BC-SSQ and BC-A-SSQ) and nanoparticles (ZrO₂, SiO₂, AlOOH) were tested for the nanoparticle haloing systems. Gravity settling experiments were performed for all different binary system combinations to choose the most stable system and also ensure proper long-term stability of the binary suspension. Gravity settling experiments of binary systems were conducted in 80 mm long tubes with a 4 mm inner diameter, as shown in **Figure 3.1**. The settling process was imaged using time-lapse photography with a digital camera.



Figure 3.1. Gravity settling experiments setup

3.2.3. IMAGING OF THE BINARY SUSPENSIONS

In order to understand the sediments' structure and observe the aggregations under gravity, an inverted microscope was used to image the binary systems. Nanoparticle haloing systems (binary systems at the isoelectric point) were imaged after 2 days of settling and at different magnifications (4x, 10x, 20x).

3.3. RESULTS AND DISSCUSION

3.3.1. GRAVITY SETTLING IMAGES

At first, microparticle suspensions at different pH were imaged at different times during sedimentation to understand the stability of the microparticles in the absence of nanoparticles. As shown in **Figure 3.2**, the microparticles started to settle immediately and there were barely any particles in the solution after 2 hours. It was also noticed that some

of the colloid aggregates were sticking to the wall of the tubes. This caused an error in measuring the height of the sediment in those systems.

For the binary systems with BC-A-SSQ microparticles and various nanoparticles, at the isoelectric point of BC-A-SSQ microparticles (near pH 7), the zeta potential of silica was highly negative (<-40 mV), zeta potential of boehmite was highly positive (>40 mV) while zirconia zeta potential was moderately positive (>20 mV).

During the gravity settling experiments of these systems, BC-A-SSQ microparticles were hard to mix, and they were mostly sticking to the sides of the tubes. It could be due to the fact that hydrogen from the amine part of BC-A-SSQ forms polar covalent bonds to oxygen, which is a more electronegative atom, and because a hydrogen atom is relatively small, the positive end of the bond dipole (the hydrogen) can approach neighboring nucleophilic or basic sites more closely than can other polar bonds. Coulombic forces are inversely proportional to the sixth power of the distance between dipoles, making these interactions relatively strong. This makes the mixing and resuspending of the suspension very hard. Therefore, BC-A-SSQ colloidal suspensions were not selected for the nanoparticle haloing systems.

Different binary systems of BC-SSQ with various nanoparticles were gravity settled and imaged*. At the isoelectric point of BC-SSQ microparticles (near pH 4), the zeta potential of silica is moderately negative (<-20) while that of boehmite and zirconia are highly positive (>40). The settling experiment results of these systems are shown in **Figure 3.3** to **Figure 3.5**.

* $\varphi_{\text{micro}} = 10^{-4}$, $\varphi_{\text{nano}} = 10^{-4}$ and 10^{-3}



Figure 3.2. Gravity settling experiment results of BC-SSQ microparticles ($\phi_{\text{micro}} = 10^{-2}$) without nanoparticles (a) at start (b) after 2 hours (c) after 6 hours at different pH values of 2 to 8.



Figure 3.3. Gravity settling experiment results of binary systems of BC-SSQ microparticles ($\phi_{\text{micro}} = 10^{-2}$) with SiO_2 nanoparticles at (a) $\phi_{\text{nano}} = 10^{-4}$ at start (b) $\phi_{\text{nano}} = 10^{-3}$ at start (c) $\phi_{\text{nano}} = 10^{-4}$ after 2 hours (d) $\phi_{\text{nano}} = 10^{-3}$ after 2 hours (e) $\phi_{\text{nano}} = 10^{-4}$ after 6 hours (f) $\phi_{\text{nano}} = 10^{-3}$ after 6 hours at different pH values of 2 to 8.

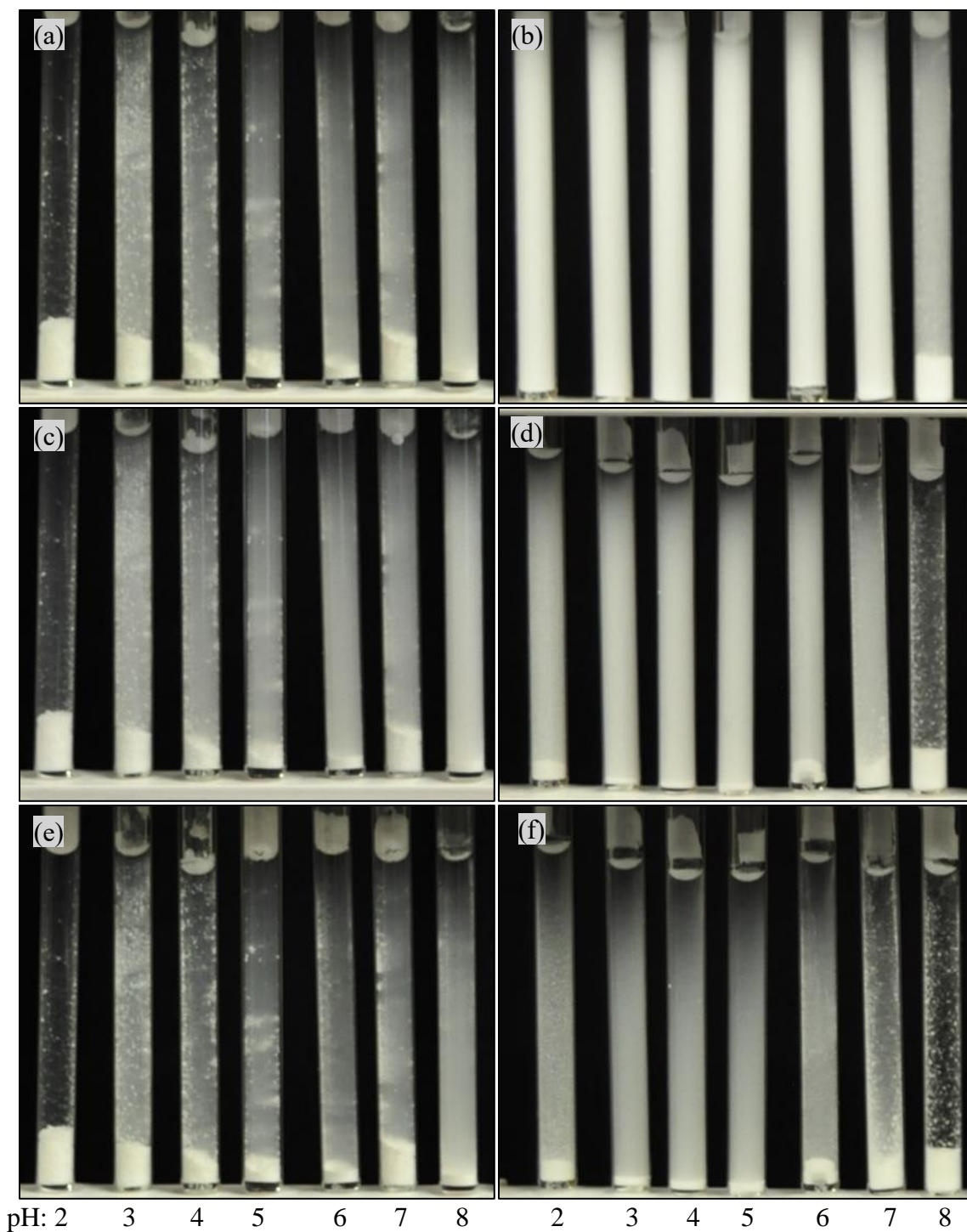


Figure 3.4. Gravity settling experiment results of binary systems of BC-SSQ microparticles ($\phi_{\text{micro}} = 10^{-2}$) with AlOOH nanoparticles at (a) $\phi_{\text{nano}} = 10^{-4}$ at start (b) $\phi_{\text{nano}} = 10^{-3}$ at start (c) $\phi_{\text{nano}} = 10^{-4}$ after 2 hours (d) $\phi_{\text{nano}} = 10^{-3}$ after 2 hours (e) $\phi_{\text{nano}} = 10^{-4}$ after 6 hours (f) $\phi_{\text{nano}} = 10^{-3}$ after 6 hours at different pH values of 2 to 8.

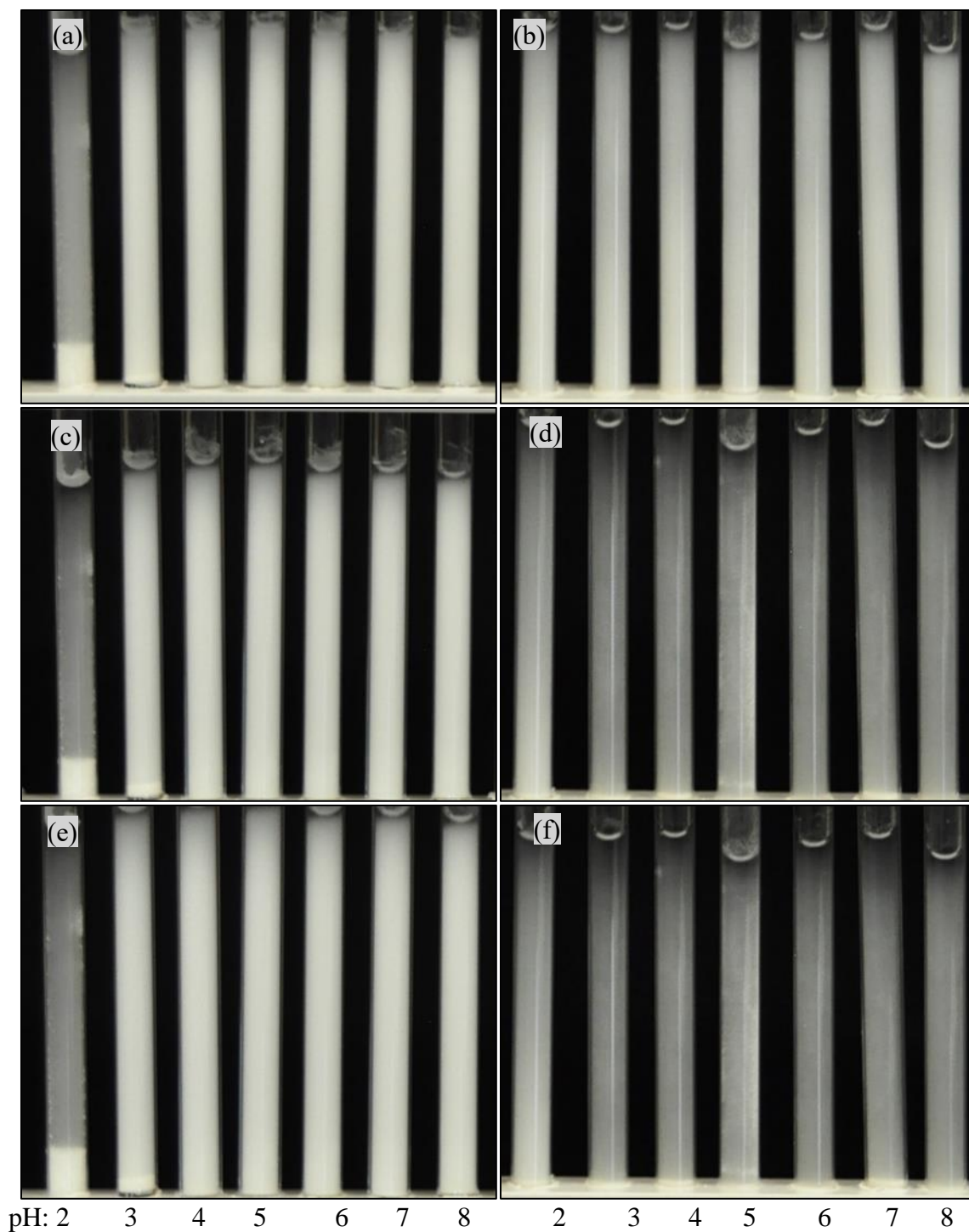


Figure 3.5. Gravity settling experiment results of binary systems of BC-SSQ microparticles ($\phi_{\text{micro}} = 10^{-2}$) with ZrO_2 nanoparticles at (a) $\phi_{\text{nano}} = 10^{-4}$ at start (b) $\phi_{\text{nano}} = 10^{-3}$ at start (c) $\phi_{\text{nano}} = 10^{-4}$ after 2 hours (d) $\phi_{\text{nano}} = 10^{-3}$ after 2 hours (e) $\phi_{\text{nano}} = 10^{-4}$ after 6 hours (f) $\phi_{\text{nano}} = 10^{-3}$ after 6 hours at different pH values of 2 to 8.

Based on the gravity settling experiments results of the three binary systems (BC-SSQ microparticles and various nanoparticles), the system with zirconia nanoparticles was the most stable system and remained suspended for a longer time. Therefore, we selected the zirconia nanoparticles for our nanoparticle haloing systems.

Gravity settling experimental results of the binary systems of BC-SSQ microparticles with different ZrO_2 concentrations at the isoelectric point is shown in **Figure 3.6**. In the absence of nanoparticles, negligibly charged microspheres coagulate due to van der Waals interactions yielding clusters that settle rapidly. However, upon adding ZrO_2 nanoparticle to the system, microsphere separation increases due to the nanoparticle induced repulsive barrier and van der Waals forces decay rapidly. By increasing the nanoparticle volume fractions the system resides in the stable fluid region from which individual colloidal microspheres settle under gravity. As seen in this figure, by increasing the ZrO_2 volume fraction from 10^{-4} to 10^{-3} , the rate that particles come out of solution increases. This can be due to the increased depletion interaction by increasing the ZrO_2 concentration.

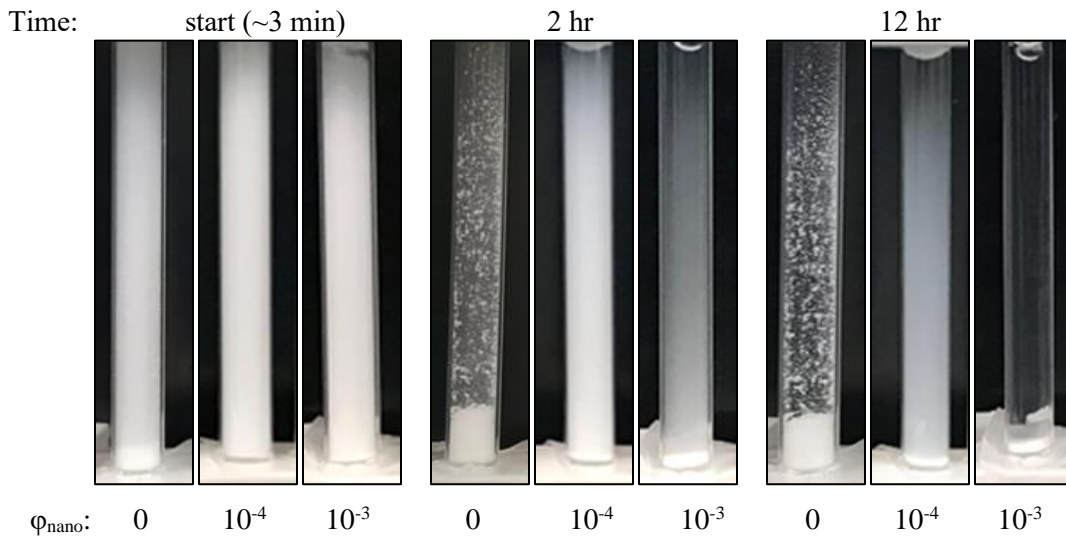


Figure 3.6. Images of gravity settling experiments of binary systems of BC-SSQ at isoelectric point with $\phi_{\text{nano}} = 0, 10^{-4}$ and 10^{-3} over time

Using equations 3.16 and 3.17, the settling velocity of an isolated particle V_0 was calculated to be 0.00051 mm/s and the settling velocity V_{micro} for a $\varphi_{micro} = 10^{-2}$ suspension of BC-SSQ microspheres in the aqueous solution was found to be 0.00050 mm/s. Since the microparticle concentration was very low, hydrodynamic interactions with neighboring particles were negligible, and V_{micro} was almost the same as V_0 . By tracking the separating interface of clear and cloudy solution in the tube (measuring the height of the clear solution and dividing it by time), the experimental microsphere settling velocity V was determined. Normalized settling velocities (V/V_{micro}) are found to be 120.1, 0.6, and 2.9 for the binary systems containing $\varphi_{nano} = 0, 10^{-4}, 10^{-3}$, respectively. By adding nanoparticles to the suspension, settling velocity decreases due to the decrease in cluster formation, resulting from the effective potential barrier that arises from nanoparticle halo formation.

In the absence of nanoparticle additions, the normalized settling velocity is approximately 120 times higher than for individual microsphere sedimentation. This reflects the formation of stringlike clusters in the suspension driven by van der Waals attractions between microspheres. By adding nanoparticles to the suspension, the normalized settling velocity decreases due to the diminished cluster formation, resulting from the effective potential barrier that arises from nanoparticle halo formation.

The sediment volume fraction, $\varphi_{sediment}$, is the total volume of the microparticle to the volume of the sediment obtained after settling. It was determined by measuring the final sediment height at long times (after 2 weeks). The settling volume fractions of the binary systems containing $\varphi_{micro} = 10^{-2}$ and $\varphi_{nano} = 0, 10^{-4}, 10^{-3}$, were found to be 0.25

0.6 and 0.4, respectively. Not surprisingly, the most open sediment structure (25 vol%) formed for pure microspheres settling in an aqueous solution.

3.3.2. MICROSCOPY IMAGES

Figure 3.7 to **Figure 3.10** show the microscopy images of the binary systems of BC-SSQ microparticles ($\phi_{\text{micro}}=10^{-2}$) and ZrO₂ nanoparticles ($\phi_{\text{nano}}=0, 10^{-4}, 10^{-3.26}, 10^{-3}$) at the isoelectric point after 2 days of settling and at different magnifications (4x, 10x, 20x).

The system with only microparticles and no nanoparticle had more aggregates with a lot of free space between them and a stringlike structure. These clusters were elongated in shape which led to an initially open sediment structure. By adding the nanoparticles to the system, aggregates became smaller and more dispersed. By increasing the concentration of nanoparticles to $10^{-3.26}$ we observed that the particles were more dispersed which is probably the effect of nanoparticle haloing. There was some regularity in the patterns of the binary systems with $10^{-3.26}$ and 10^{-3} nanoparticles. This indicates the possibility of achieving some level of crystallization in these systems.

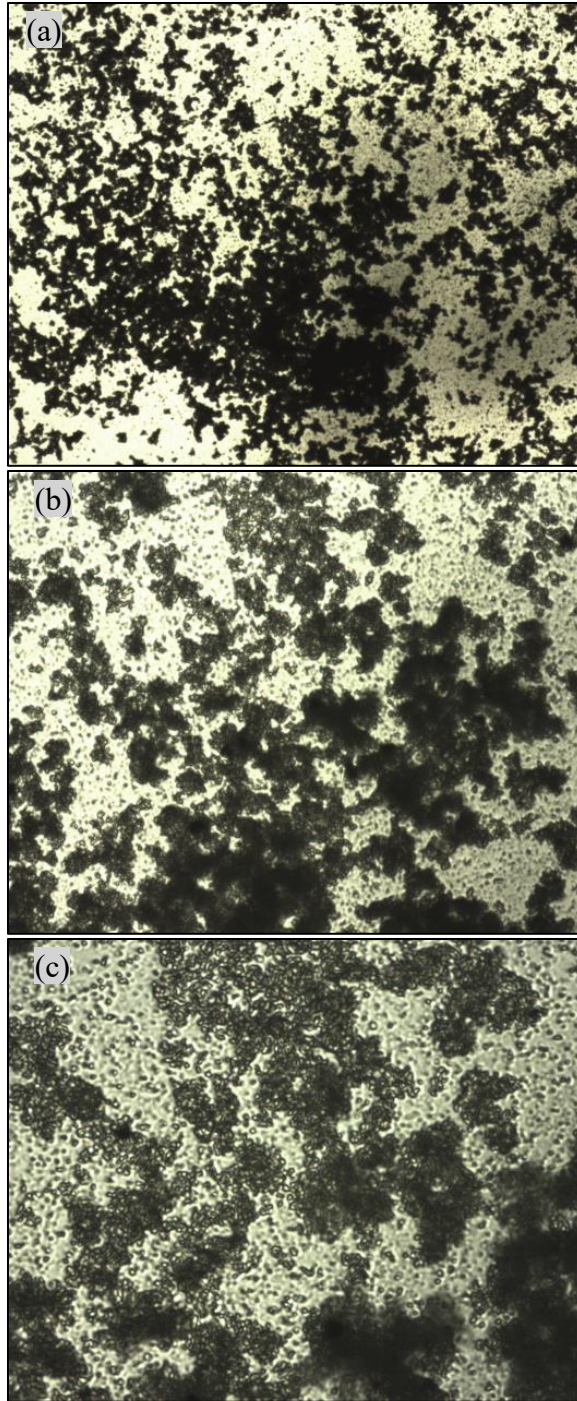


Figure 3.7. Inverted microscopy images of binary systems of BC-SSQ microparticles ($\varphi_{\text{micro}}=10^{-2}$) and ZrO_2 nanoparticles ($\varphi_{\text{nano}}=0$) at isoelectric point after 2 days with (a) 4x magnification (b) 10x magnification (c) 20x magnification

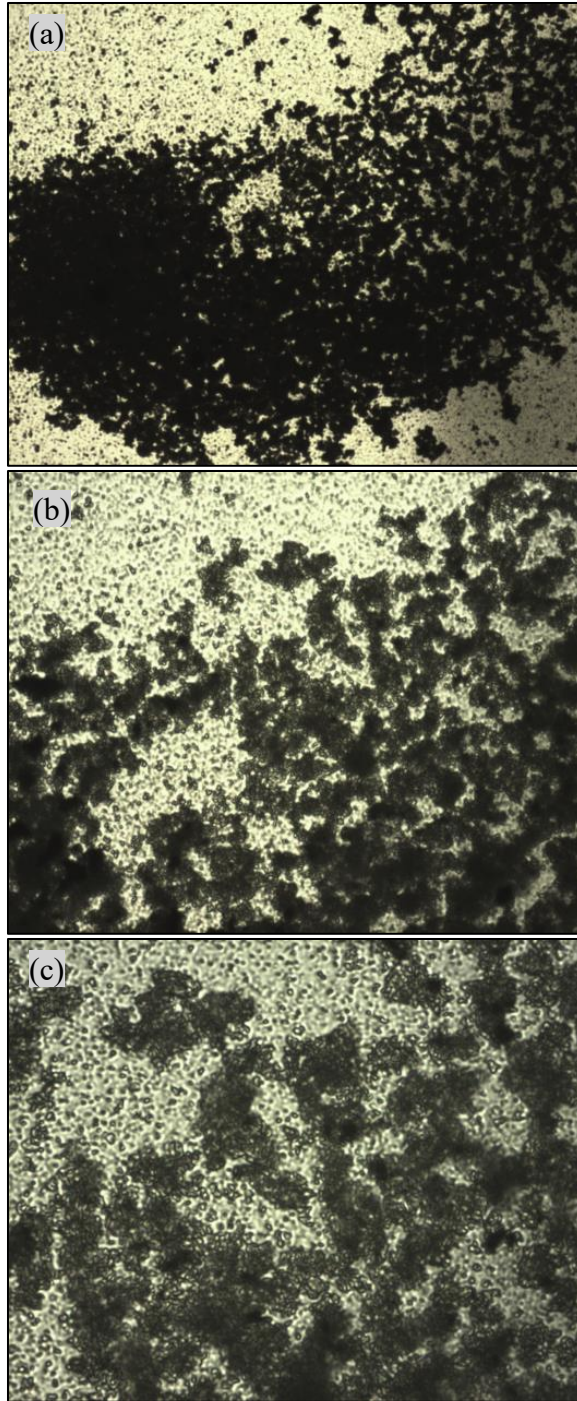


Figure 3.8. Inverted microscopy images of binary systems of BC-SSQ microparticles ($\varphi_{\text{micro}}=10^{-2}$) and ZrO₂ nanoparticles ($\varphi_{\text{nano}}=10^{-4}$) at isoelectric point after 2 days with (a) 4x magnification (b) 10x magnification (c) 20x magnification

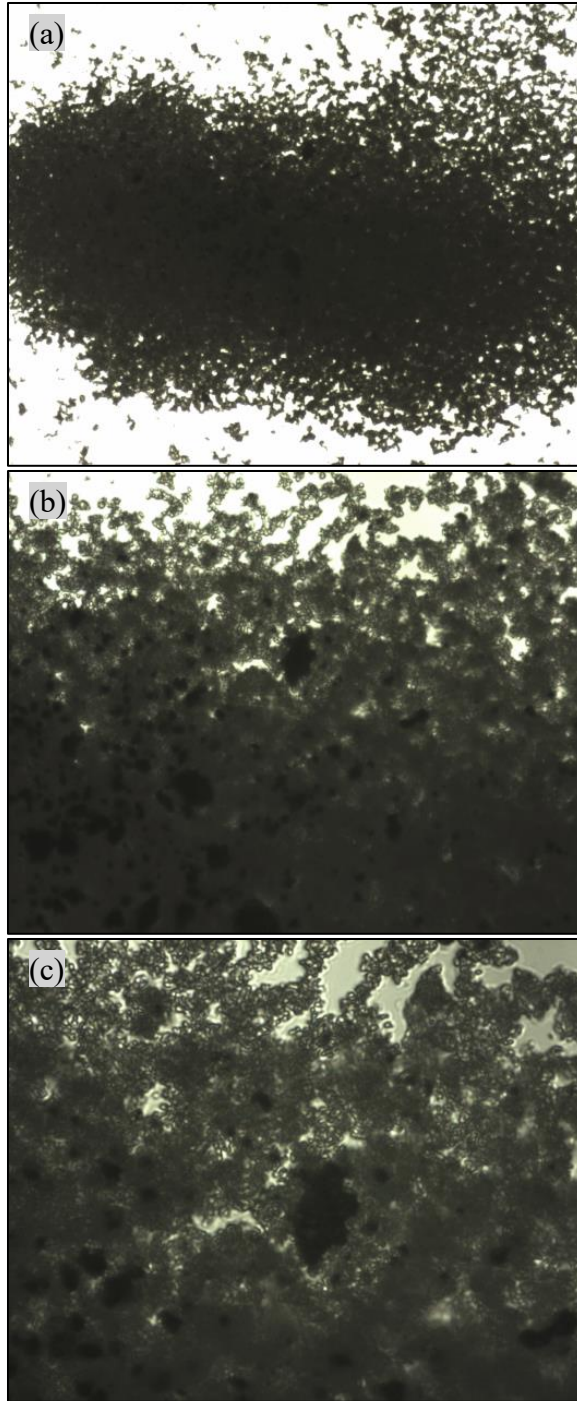


Figure 3.9. Inverted microscopy images of binary systems of BC-SSQ microparticles ($\varphi_{\text{micro}}=10^{-2}$) and ZrO_2 nanoparticles ($\varphi_{\text{nano}}=10^{-3.26}$) at isoelectric point after 2 days with (a) 4x magnification (b) 10x magnification (c) 20x magnification

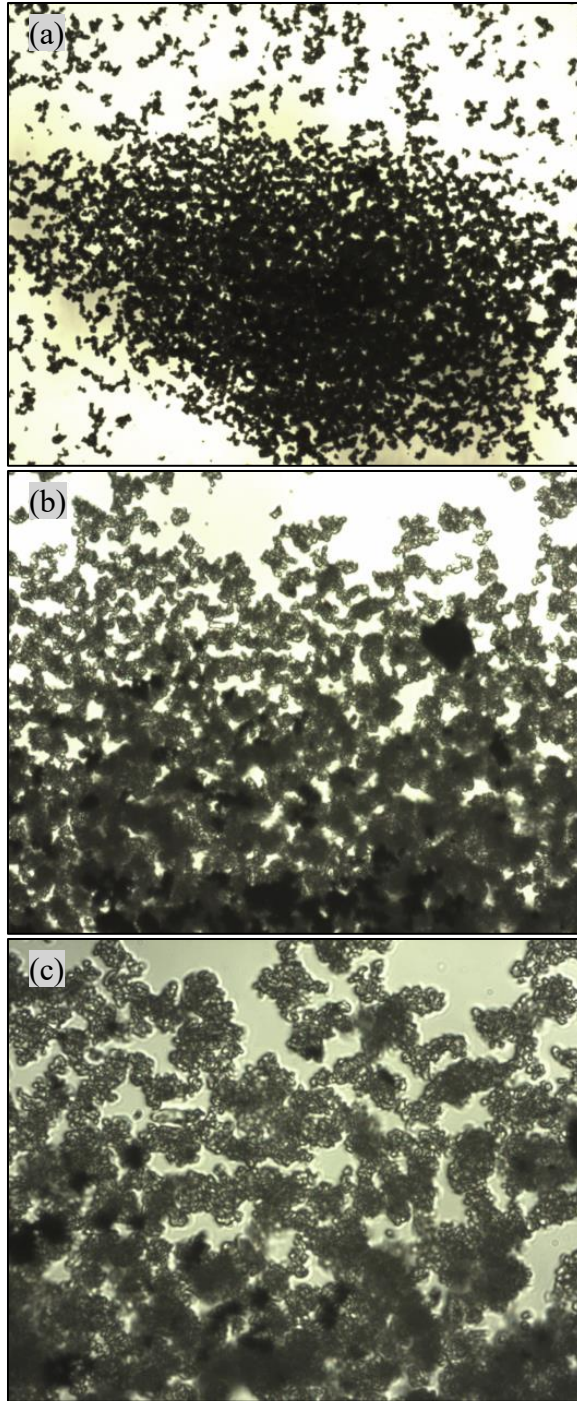


Figure 3.10. Inverted microscopy images of binary systems of BC-SSQ microparticles ($\varphi_{\text{micro}}=10^{-2}$) and ZrO_2 nanoparticles ($\varphi_{\text{nano}}=10^{-3}$) at isoelectric point after 2 days with (a) 4x magnification (b) 10x magnification (c) 20x magnification

3.4. CONCLUSION

In order to make the nanoparticle haloing binary solutions for the ISS experiments, we had a series of criteria to meet to be able to get the samples onboard and to get the full benefit of the ISS experiments. First of all, we were looking for a system with a possibility of crystallization and crystalline structures. In addition, nanoparticle haloing systems had to be easy to mix and also stable. Gravity settling experiment were performed in order to understand what system would be most stable for the ISS experiments. The stability measurements for this purpose were mostly qualitative.

Based on the ground settling experiments and ease of mixing, 1.2 μm BC-SSQ microparticles and 5-20 nm zirconia (ZrO_2) nanoparticles were selected for the nanoparticle haloing systems in this study and for the ISS experiments. Based on the zeta potential results, the pH of these samples was high enough to meet the NASA safety requirements.

Gravity settling experiments along with the microscopy images showed that in the system without nanoparticles, have clusters that are elongated in shape have open sediment structures. In fact, in the absence of nanoparticles, microspheres coagulated due to van der Waals interactions yielding clusters that settle rapidly and with an open sediment structure. By adding the nanoparticles to the system, the normalized settling velocity decreased due to the effective potential barrier that arises from nanoparticle halo formation. It was also shown that the most open sediment structure forms for pure microspheres settling in an aqueous solution. Microscopy images indicated that there is a possibility of achieving some level of crystallization in the nanoparticle haloing systems.

Initially, we wanted to also calculate the stability ratios of the binary systems as discussed in the introduction. In order to measure the volume and weight of the clusters, 3-dimensional image stacks with high resolution were needed to count the number of particles in each cluster. But our microscopes did not have that ability, so we were not able to measure the stability ratios of the samples.

CHAPTER 4

EFFECT OF TEMPERATURE

ON NANOPARTICLE HALOING SYSTEMS

4.1. INTRODUCTION

Research in colloids is gaining interest from NASA, NSF, and industry due to potential new materials that could enable advanced solar energy harvesters, mechanically robust materials, inexpensive electronic displays, and analytical instrumentation for both space-related and terrestrial activities. The following are a few of the many applications of colloid-based nanomaterials:

- “Nanofluids” with unusually high thermal conductivity used for advanced heat transfer applications ⁸⁹.
- Quantum dot solar cells with enhanced efficiencies, tunable absorption, sensitivity to diffused light, and flexibility ⁹⁰.
- Colloidal carbon films used for electromagnetic radiation shielding ⁹¹.

Understanding the temperature effect is important for these applications, as colloids can be kept at temperatures that are remarkably different from the typically used room temperature.

It is essential to understand colloids' behavior at elevated temperatures that are much different from the typical room temperature. In addition to the fact that temperature greatly influences colloidal aggregation, the lack of studies at elevated temperatures makes it impossible to understand how colloids may function in high-temperature applications.

When a temperature gradient is applied to a colloidal suspension in the presence of a wall, the particles will form a highly ordered crystal on the wall itself driven by Marangoni-like forces, which could potentially disrupt nanoparticle haloing ⁹². Thermophoresis, or the Soret effect, is the motion of particles caused by thermal gradients and is a challenging subject both experimentally and theoretically ⁹³⁻⁹⁶. However, recent experimental studies and mathematical models have provided new insights into thermophoresis as a subtle interfacial effect, which has helped bring thermophoresis into a clearer perspective. The recent scientific advances open up exciting possibilities for using thermophoresis for macromolecular fractionation, microfluidic manipulation, and controlling colloidal structures ⁹⁴.

Thermophoretic velocity is not affected by particle size, unlike dielectrophoresis and magnetophoresis where the velocity grows with the square of the particle radius ⁹⁷. In dilute suspensions, thermophoresis is driven by hydrodynamic forces resulting from a local interaction between the fluid and the colloid. Particle shape, surface coating, temperature, salinity, pH, and solvent expansivity are some of the factors that influence this interaction ⁹².

The phoretic process is generally attributed to flow in the interfacial layer, leading to slip boundary conditions on the particle surface. When the particle distances are small enough for the flow fields generated around each particle to overlap, many-body effects

are then to be expected. When colloidal particles are confined to a wall by a phoretic motion, hydrodynamic interactions may result in effective pseudopotentials^{92,93}.

Thermal gradients could cause thermophoretic particles to form stable, ordered structures through the long-range attraction between like-charged particles. An interaction with such a long range may offer new possibilities for fabricating ordered structures^{92,98}.

Unlike temperature gradient, the thermal shock effect has not gained much attention in colloid aggregation studies. We are the first group that has studied the impact of thermal shock on nanoparticle haloing, which provides a new perspective on the stability of the suspensions with temperature-dependent halo disruption.

Higher temperature will generally promote aggregation due to the increase in the collision frequency between particles and increase of the kinetic energy, which makes it easier for the particles to overcome the energy barrier that reflects the aggregation tendency^{99,100}. On the other hand, increasing the temperature could give a high enough shear force for breaking the aggregates^{3,101,102}. In this study, we investigated the temperature effect on the aggregation of nanoparticle haloing binary systems.

4.2. METHODS

The effect of temperature was explored on various nanoparticle haloing systems. For this purpose, nanoparticle haloing binary systems were observed under an inverted confocal microscopy (Andor du-897-cso) at 40x magnification and a digital camera (Sensicam QE, PCO) at 4x magnification. Confocal microscopy has a number of advantages over conventional microscopy, including a shallow depth of field, the reduction

of out-of-focus glare, the ability to collect serial optical sections, and the potential to collect hundreds of optical sections at a time.^{103, 104}

The binary systems used in these experiments were the binary suspensions of BC-SSQ-RhB microparticles and ZrO₂ nanoparticles ($\phi_{\text{micro}}=10^{-3}$, $\phi_{\text{nano}} = 10^{-4}$, $10^{-3.26}$, 10^{-3}). Sample preparation for these experiments is similar to what is explained in section 3.2.1 of the previous chapter. However, at $\phi_{\text{micro}}=10^{-2}$, it was impossible to observe the clusters and differentiate them from the background because they did not have enough color contrast. Therefore, the microparticles concentration had to be ten-fold diluted ($\phi_{\text{micro}}=10^{-3}$). This concentration was high enough for the particles to form aggregates and thin enough to differentiate between the aggregates and the background.

Two types of experiments were designed to measure the impact of the temperature on nanoparticle halving: temperature shock and temperature gradient.

Temperature Shock Design:

Each of the samples is heated by slowly ramping the temperature up to the desired maximum temperature setpoint over a period of 10 minutes. The samples are held at that temperature for 2 minutes, then cooled back to ambient temperature over 10 minutes. Samples are observed with a confocal microscope and microscope images are acquired at the highest magnification possible before, during, and after heating from ambient to the setpoint and cooling back to ambient.

Temperature Gradient Design:

Each of the samples are heated to a temperature gradient, centered around the desired temperature with the largest gradient possible at that temperature. Samples should

be observed as in the previous condition. Images are acquired before, during, and after a temperature gradient is applied.

4.2.1. TEMPERATURE EXPERIMENTS ON THE ISS

On earth, gravity induces sedimentation which prevents proper observations of the governing physics but in microgravity insight into colloidal interactions is possible. The ISS LMM heating module can produce a thermal gradient across the viewable area (ACE-T*). As discussed in the introduction, the presence of a thermal gradient will drive colloidal crystal formation on an impinging wall. Increasing the scale of the stable system and performing the temperature experiments on the ISS allows the determination of particle relative motion with respect to the temperature gradients. The experiments will elucidate the impact of the Marangoni-like forces on the different particle sizes and how that influences the stability of the haloing system during the organization process.

Temperature shock experiments up to 60°C and temperature gradient experiments centered around 45°C and 50°C with + and -10°C (20°C gradient: 35°C to 55°C and 40°C to 60°C) were performed on ISS. Through the confocal capabilities on the LMM on the ISS, it is possible to gain a fundamental understanding of the effect of temperature on nanoparticle haloing, which helps in the development of future materials where the assembly and structure of colloids are critical. The ISS experimental setup is shown in **Figure 4.1**. These experiments were done over a 4-week period starting March 22, 2021. The results will provide evidence of the applicability of gradient-driven flows in forming colloidal crystals in a nanoparticle haloing system. The resulting data were obtained;

* Advanced Colloids Experiment (Temperature controlled)

however, analyzing the ISS results is beyond the scope of this study and would be a direction for future research.

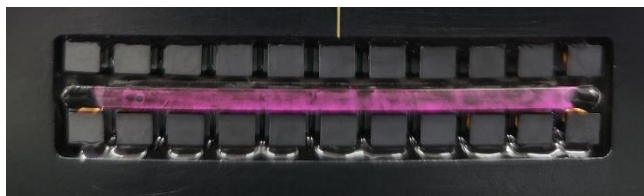


Figure 4.1. ISS experimental setup.

4.2.2. GRAVITY TEMPERATURE EXPERIMENTS

We did not have the capability to create a thermal gradient and promote thermophoresis. Therefore, we only executed the temperature shock studies in our ground-based experiments.

The highest temperature shock that was performed on the ISS was 60°C due to the equipment limitations. However, there was not a significant change in the average size of the aggregates at that temperature in our preliminary ground-based experiments. Therefore, in our gravity experiments, we tested higher temperatures of 70°C and 80°C as well. Temperatures above 80°C were not used due to the wax softening issues at those temperatures.

In each temperature shock experiment, the binary solution ($\phi_{\text{micro}}=10^{-3}$, $\phi_{\text{nano}} = 10^{-4}$, $10^{-3.26}$, 10^{-3}) was mixed, and a capillary tube* (VitroTubes #3536) was immersed in the suspension until the capillary was filled completely. Then both ends of the capillary tube were sealed with wax to keep the solution inside the capillary during the heating. Filled capillaries were then sat horizontally for two hours until all the particles settled and formed aggregates. In order to perform the heating, each capillary was kept

* Capillary tubes were cut to fit the width of the ITO glass

between two ITO glasses, which acted as the top and bottom heaters, as displayed in **Figure 4.2**. Each heater was connected to a temperature controller (OMEGA CN16PT-330). As shown in **Figure 4.3**, Indium tin oxide (ITO) glasses were heated from room temperature ($\sim 25^\circ\text{C}$) to a maximum of 60°C , 70°C , or 80°C in 10 consecutive steps while being held at each step for 1 minute and then 2 minutes at the maximum temperature. ITO glasses were then cooled back to ambient temperature over 10 steps. Microscope images were acquired at 40x magnification before (2 hours after filling the capillary tube), during the temperature ramp and soak, and after 2 hours.

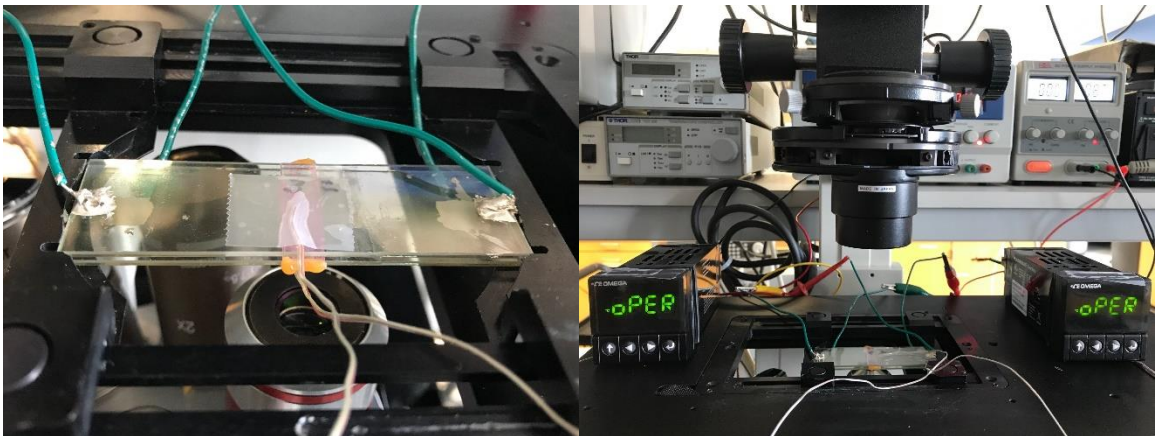


Figure 4.2. Temperature shock experiment setup

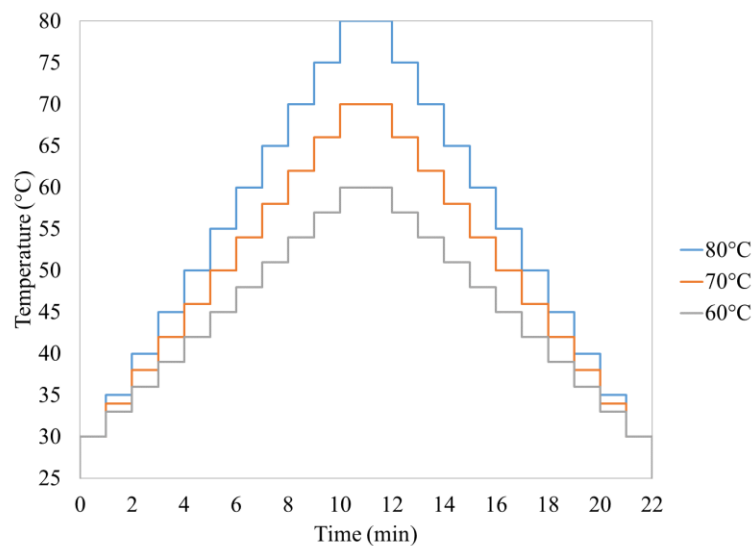


Figure 4.3. Temperature shock heating and cooling steps

4.2.3. IMAGE ANALYSIS

Confocal images of the binary systems were analyzed using ImageJ software, with two complementary methods: average the size of blobs after thresholding and determining the characteristic length based on the structure factor of the imaging data. In order to average the blob sizes, the image must be divided into the blobs (which are assumed to be colloid aggregates) and the background. Characteristic length measures the average length of the features in the image, which can depend on both the size of the aggregates and the distance between them.

Average blob size:

At first, a rolling ball algorithm was used to even the illuminated background and remove large spatial variations of the background intensities. The image was then thresholded by the Iso-Data algorithm to separate between foreground objects and background pixels. Then a binary mask operation was performed on the thresholded image, a watershed separation was performed, and the average size of the resulting blobs was recorded^{74, 105}.

Structure factor and characteristic length:

The characteristic length was calculated using Fast Fourier-transforming (FFT) of the image computed by ImageJ software. Using the FFT of an image, we can get the spatial frequency of dominant features and their characteristic length. For this purpose, an FFT bandpass filter (large structures down to 100 pixels and small structures up to 2 pixels) was first applied in order to correct for the uneven lighting of the side illumination. Then the FFT was radially averaged to obtain the structure factor, $S(q,t)$, where q is the radial distance of the FFT image. The difference in the brightness of the images resulted in

different shifting of their structure factor. Therefore, all the structure factor values were shifted down until a high spatial frequency content of zero ¹⁰⁶⁻¹⁰⁹.

Any distinctive peak of the structure factor detects the characteristic length of the underlying structures in the image. Increasing the size and distance of the structures would result in a shift of the peak value to the left (from larger q to smaller q). Calculated $S(q,t)$ of the images was noisy with no distinct single peak; therefore, we tried using the first moment of the structure factor as follow ^{107, 109}:

$$q(t) = \frac{\int_{q_1}^{q_2} qS(q,t)dq}{\int_{q_1}^{q_2} S(q,t)dq} \quad (4.1)$$

We further modified the first moment of the structure factor in order to give more weight to lower frequency content ¹⁰⁹:

$$q'(t) = \frac{\int_{q_1}^{q_2} qS(q,t)*S(q,t)dq}{\int_{q_1}^{q_2} S(q,t)*S(q,t)dq} \quad (4.2)$$

The characteristic length was then calculated using $\frac{1}{q'(t)}$. This characteristic length was multiplied by an arbitrary number for plotting purposes ¹⁰⁹.

4.3. RESULTS AND DISSCUSION

Average Blob Size Analysis:

Each confocal image from before, during, and after the temperature shock cycle was analyzed for average blob size. **Figure 4.4** shows a sample confocal image and the resulting blob areas from the ImageJ analysis. The average blob size from before, during, and after 60°C, 70°C, and 80°C temperature shock cycles was graphed in **Figure 4.5**, **Figure 4.6**, and **Figure 4.7**.

Blob size depends on the size and number of the aggregates present in the imaging area. Blob size was slightly different at different regions of each capillary tube. Therefore, in order to minimize the error, we imaged the same region (with the same aggregates) during the whole temperature shock experiment. Since different samples had different initial blob sizes, we shifted all the initial blob size values to a specific value to be able to better compare the results and the change in the blob size of the samples.

Figure 4.5 to **Figure 4.7** show that the average blob size increases with applying the temperature shock to the samples. After 60°C temperature shock, the average blob size slightly increased at the lowest volume fraction, but it was almost constant at the higher volume fractions. By increasing the temperature shock from 60°C to 80°C, the average blob size change was more significant. In addition, the average blob size growth was more significant in the nanoparticle haloing samples with the lowest nanoparticle concentration.

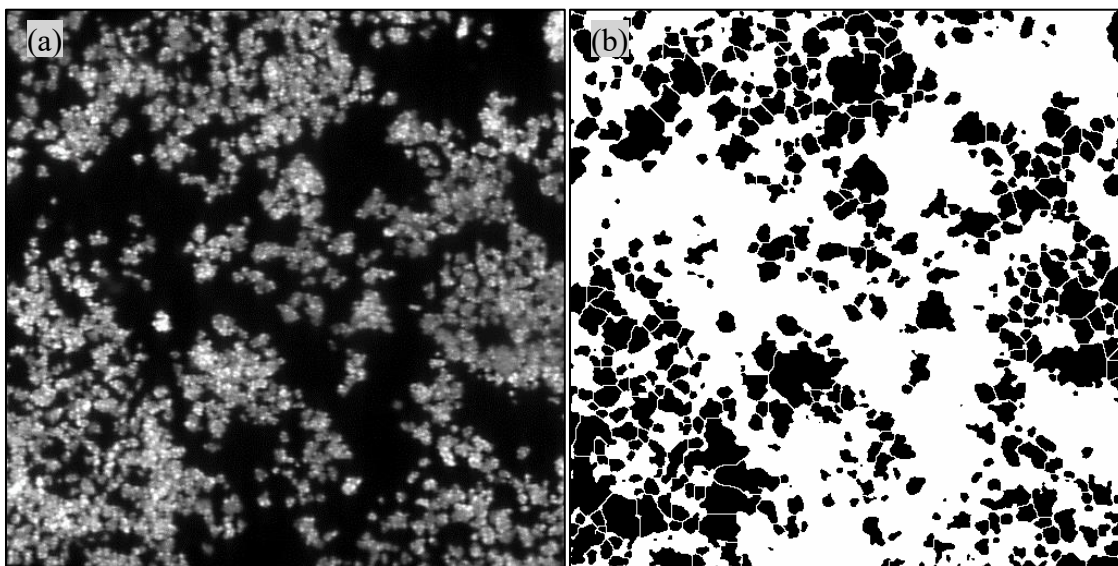


Figure 4.4. (a) An example of confocal laser scanning microscope image with 40x magnification (white particles on black background) and (b) resulting image after applying watershed using ImageJ (black blobs on white background)

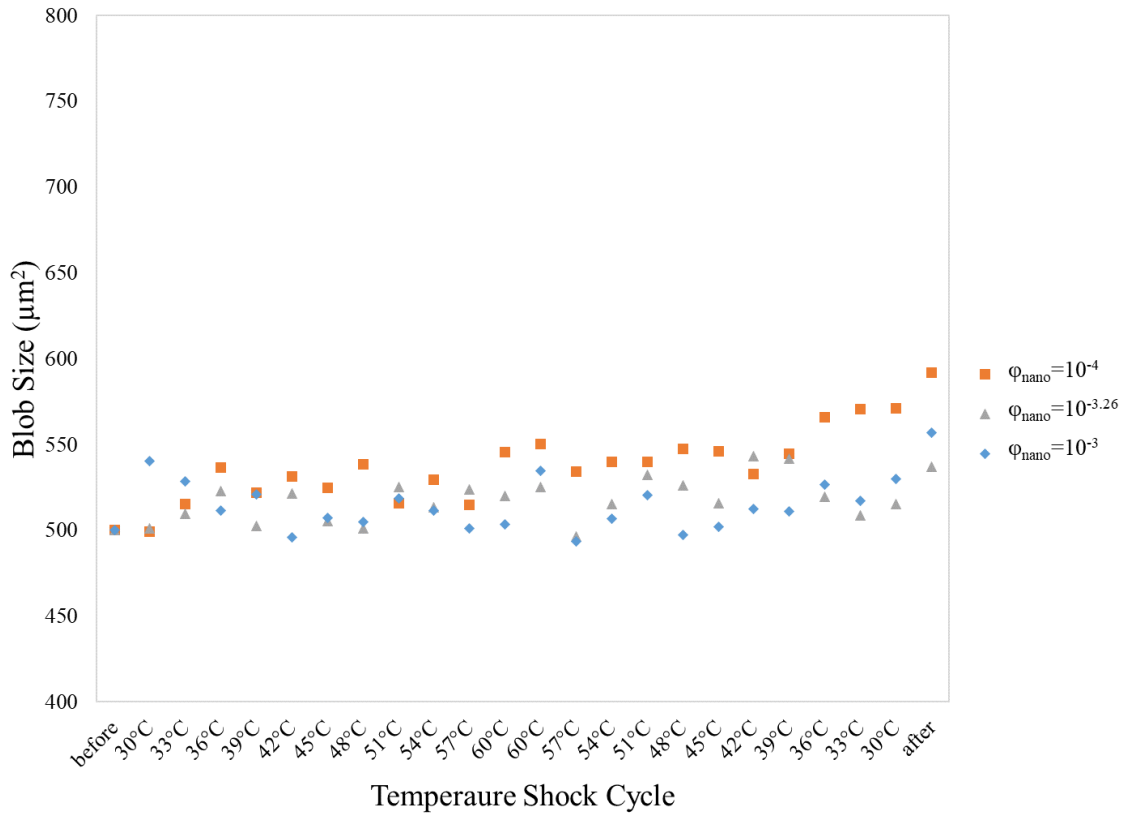


Figure 4.5. Average blob size of the binary systems with $\phi_{\text{micro}}=10^{-3}$ BC-SSQ microparticles and $\phi_{\text{nano}} = 10^{-4}$, $\phi_{\text{nano}} = 10^{-3.26}$, $\phi_{\text{nano}} = 10^{-3}$ ZrO₂ nanoparticles, during 60°C temperature shock cycle

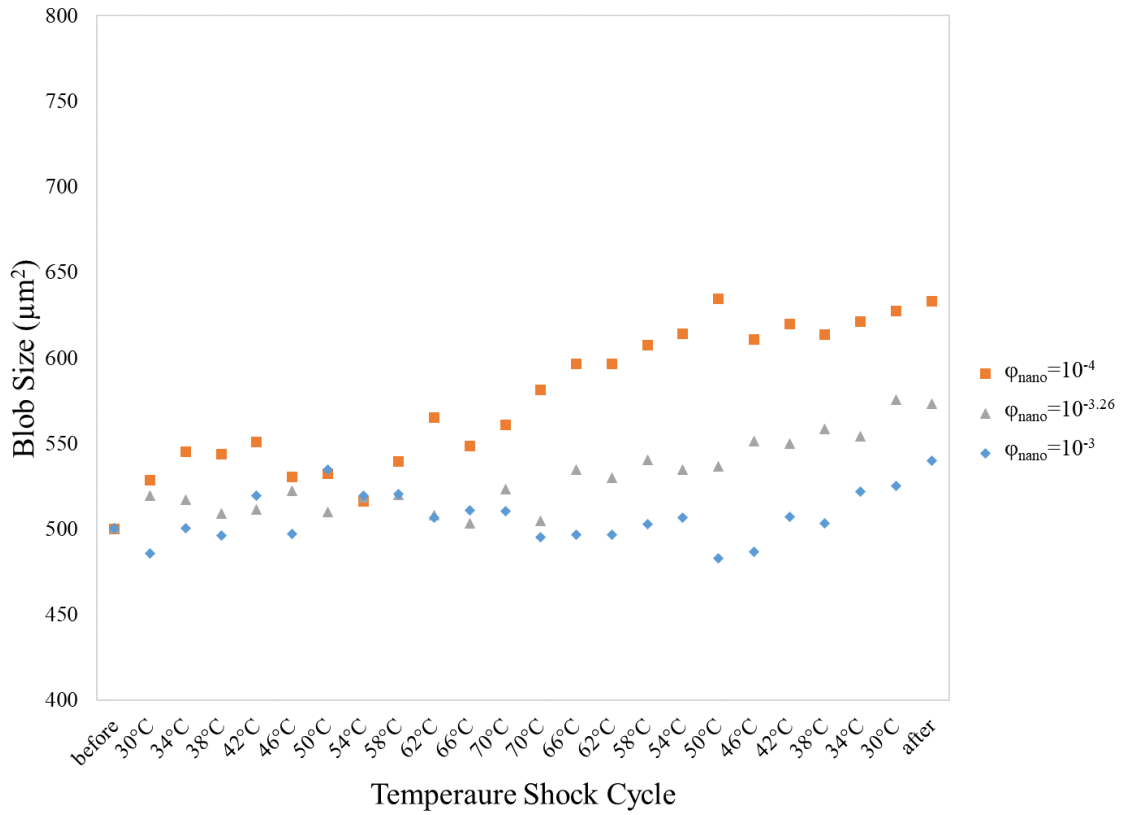


Figure 4.6. Average blob size of the binary systems with $\phi_{\text{micro}}=10^{-3}$ BC-SSQ microparticles and $\phi_{\text{nano}} = 10^{-4}$, $\phi_{\text{nano}} = 10^{-3.26}$, $\phi_{\text{nano}} = 10^{-3}$ ZrO₂ nanoparticles, during 70°C temperature shock cycle

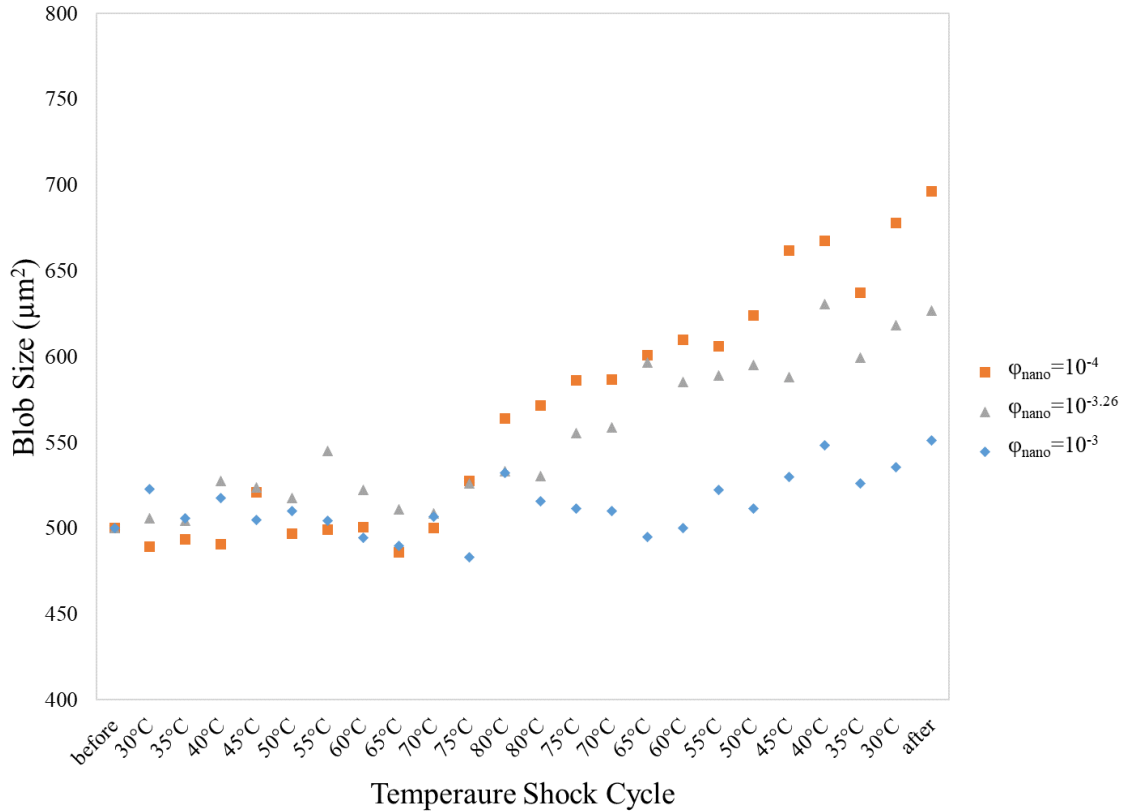


Figure 4.7. Average blob size of the binary systems with $\phi_{\text{micro}}=10^{-3}$ BC-SSQ microparticles and $\phi_{\text{nano}} = 10^{-4}$, $\phi_{\text{nano}} = 10^{-3.26}$, $\phi_{\text{nano}} = 10^{-3}$ ZrO₂ nanoparticles, during 80°C temperature shock cycle

Structure factor and characteristic length:

Each confocal image from before, during, and after the temperature shock cycle was analyzed for structure factor and characteristic length by ImageJ. **Figure 4.8** shows a sample radially averaged $S(q,t)$ measured at different steps of the 60°C temperature shock cycle. The characteristic length of the binary systems, before, during, and after 60°C, 70°C, and 80°C temperature shock cycles was graphed in **Figure 4.9**, **Figure 4.10**, and **Figure 4.11**. These figures show a similar trend to the average blob size, where the characteristic length of the samples increases by applying the temperature shock.

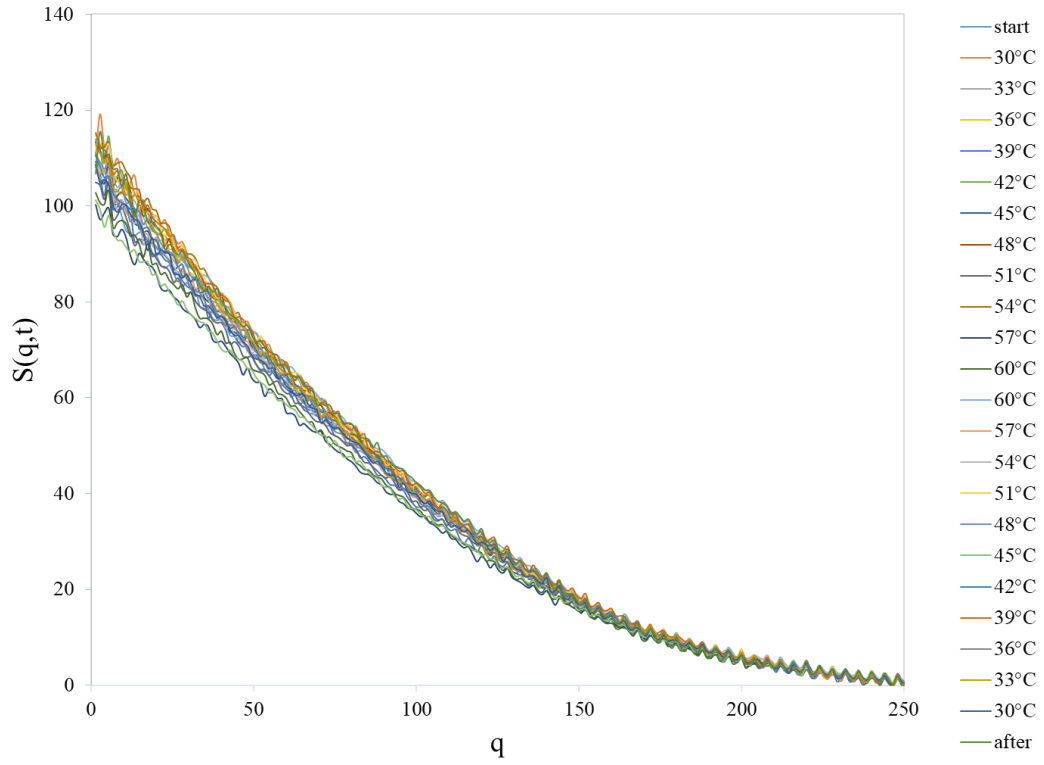


Figure 4.8. An example of radially averaged $S(q,t)$ at different steps of 60°C temperature shock cycle

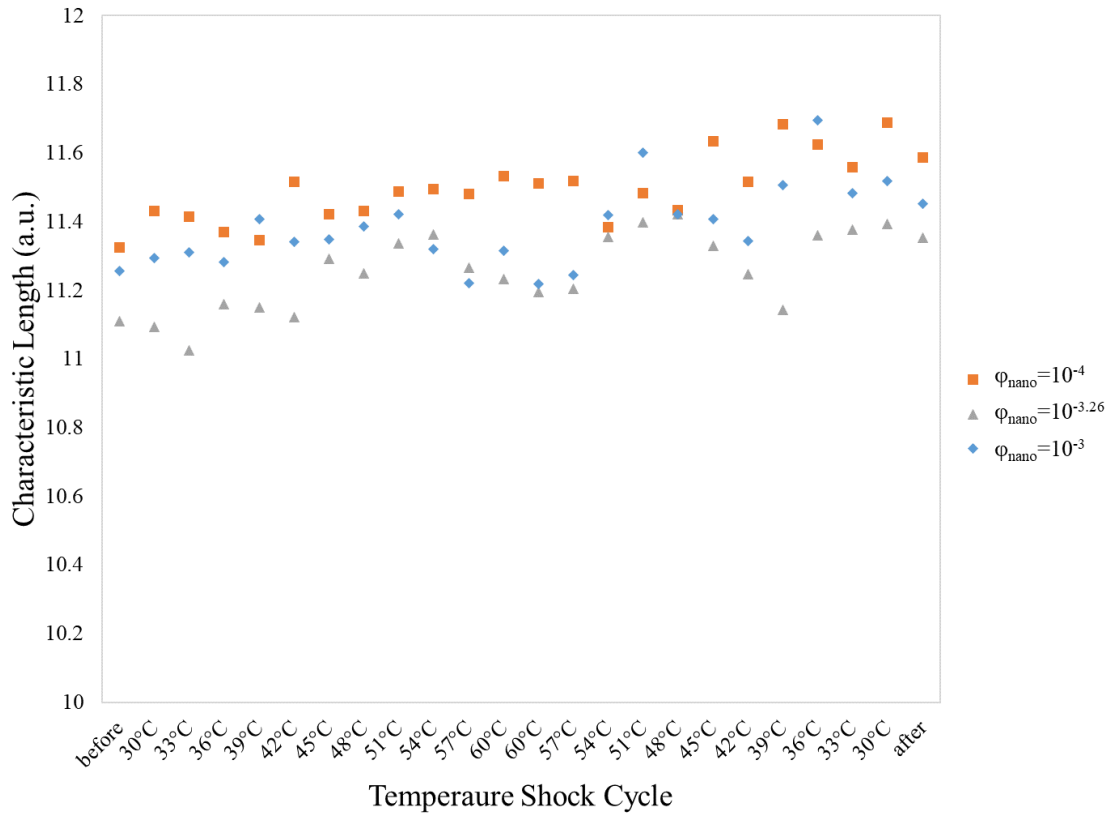


Figure 4.9. Characteristic length of the binary systems with $\phi_{\text{micro}}=10^{-3}$ BC-SSQ microparticles and $\phi_{\text{nano}} = 10^{-4}$, $\phi_{\text{nano}} = 10^{-3.26}$, $\phi_{\text{nano}} = 10^{-3}$ ZrO₂ nanoparticles, during 60°C temperature shock cycle

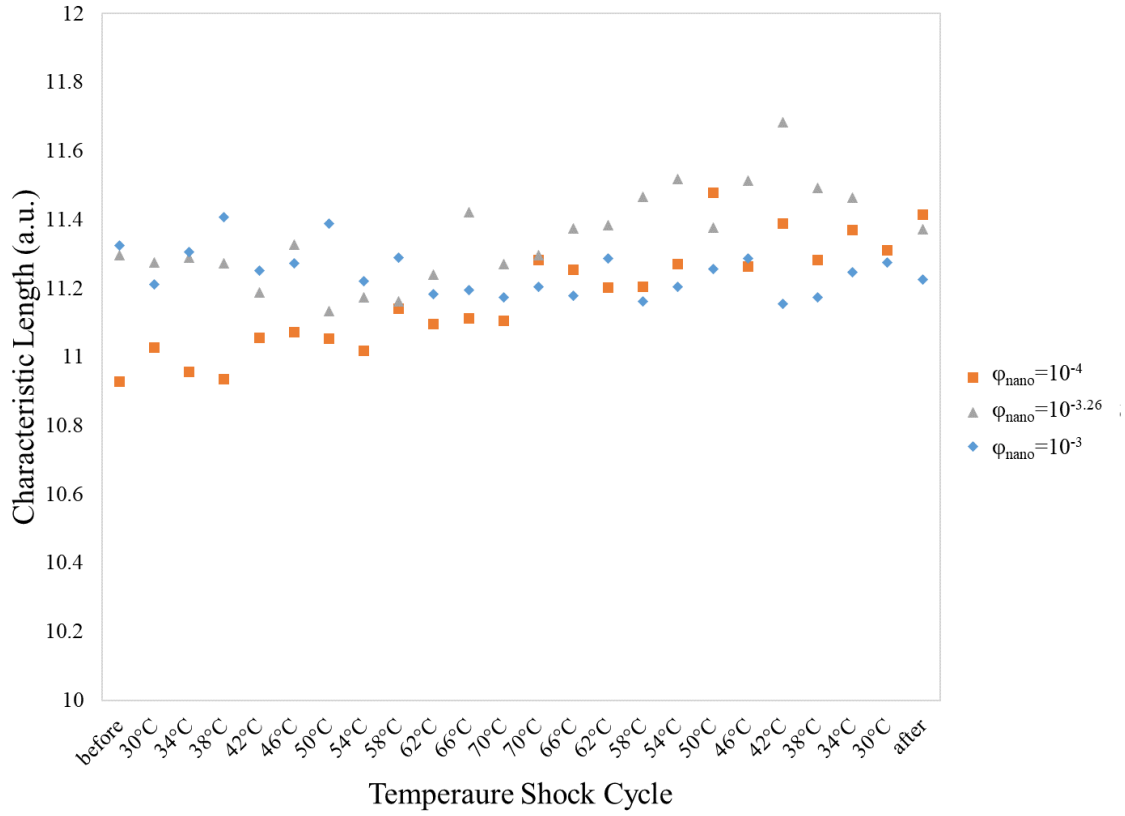


Figure 4.10. Characteristic length of the binary systems with $\phi_{\text{micro}}=10^{-3}$ BC-SSQ microparticles and $\phi_{\text{nano}} = 10^{-4}$, $\phi_{\text{nano}} = 10^{-3.26}$, $\phi_{\text{nano}} = 10^{-3}$ ZrO₂ nanoparticles, during 70°C temperature shock cycle

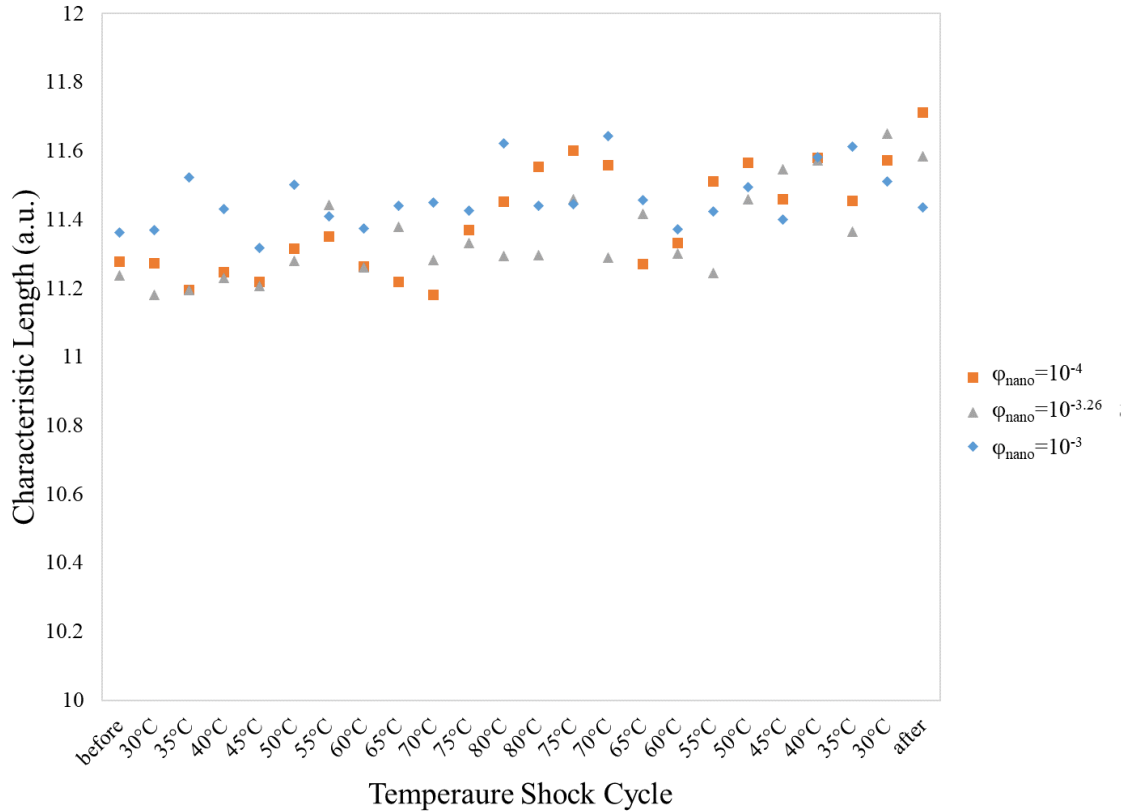


Figure 4.11. Characteristic length of the binary systems with $\phi_{\text{micro}}=10^{-3}$ BC-SSQ microparticles and $\phi_{\text{nano}} = 10^{-4}$, $\phi_{\text{nano}} = 10^{-3.26}$, $\phi_{\text{nano}} = 10^{-3}$ ZrO₂ nanoparticles, during 80°C temperature shock cycle

Inverted microscope images* of the binary solutions before and after 60°C, 70°C, and 80°C temperature shock cycles are shown in **Figure 4.12**, **Figure 4.13**, and **Figure 4.14**. From qualitative observations, for the binary system with $\phi_{\text{micro}}=10^{-3}$ and $\phi_{\text{nano}} = 10^{-4}$, the relative coarseness of the network reduces as the maximum temperature increases. In this case the visualization of coarseness is driven by the size and distribution of the microparticle aggregates. By increasing the concentration of nanoparticles in the nanoparticle halving binary systems, the systems become more stable and the change in

* Black particles on light background

the thickness and coarseness of the aggregates with the temperature shock becomes less significant.

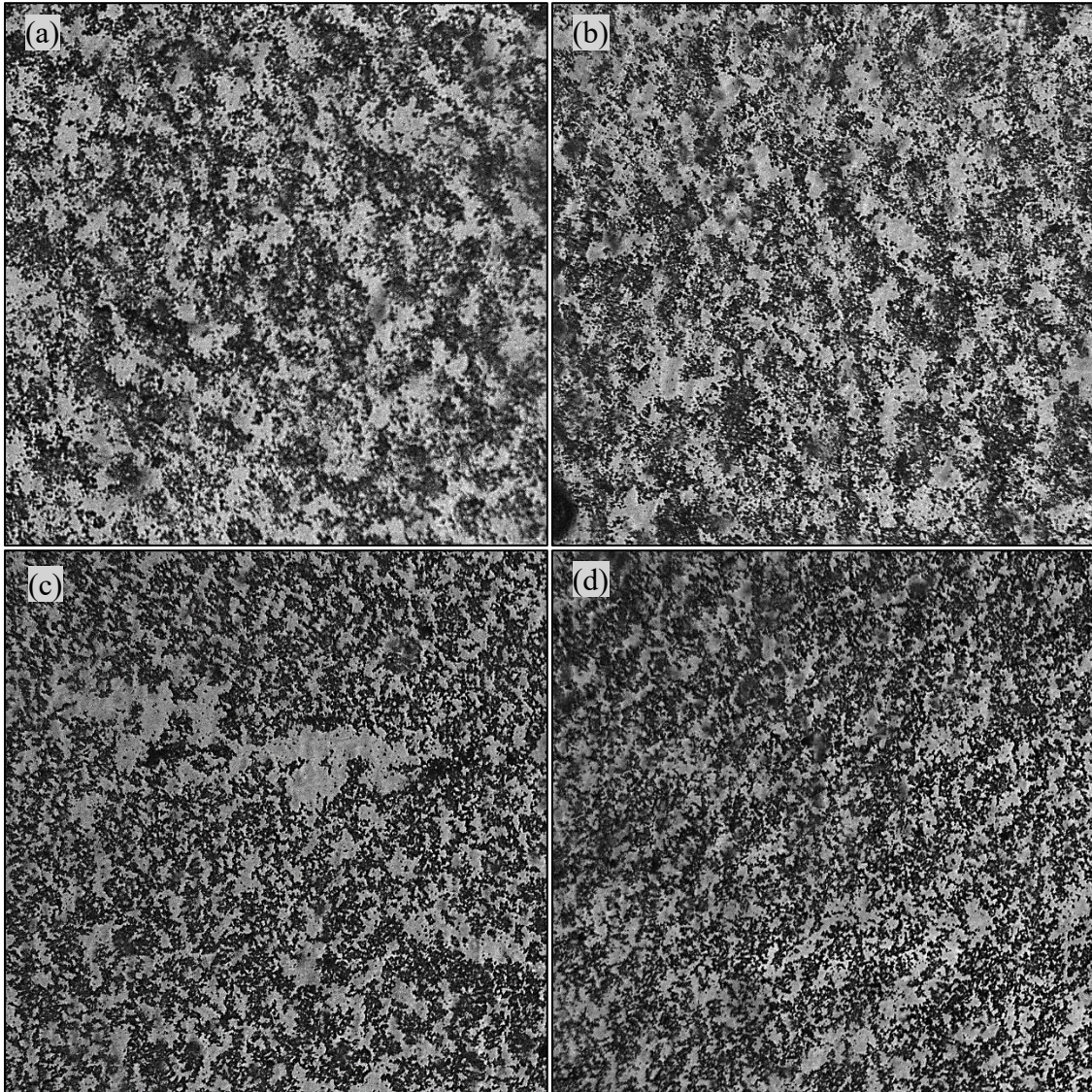


Figure 4.12. Microscopy images (4x magnification) of the binary systems of BC-SSQ microparticles ($\varphi_{\text{micro}}=10^{-3}$) and ZrO_2 nanoparticles ($\varphi_{\text{nano}} = 10^{-4}$) (a) before and / (b) after 60°C (c) after 70°C (d) after 80°C temperature shock cycles.

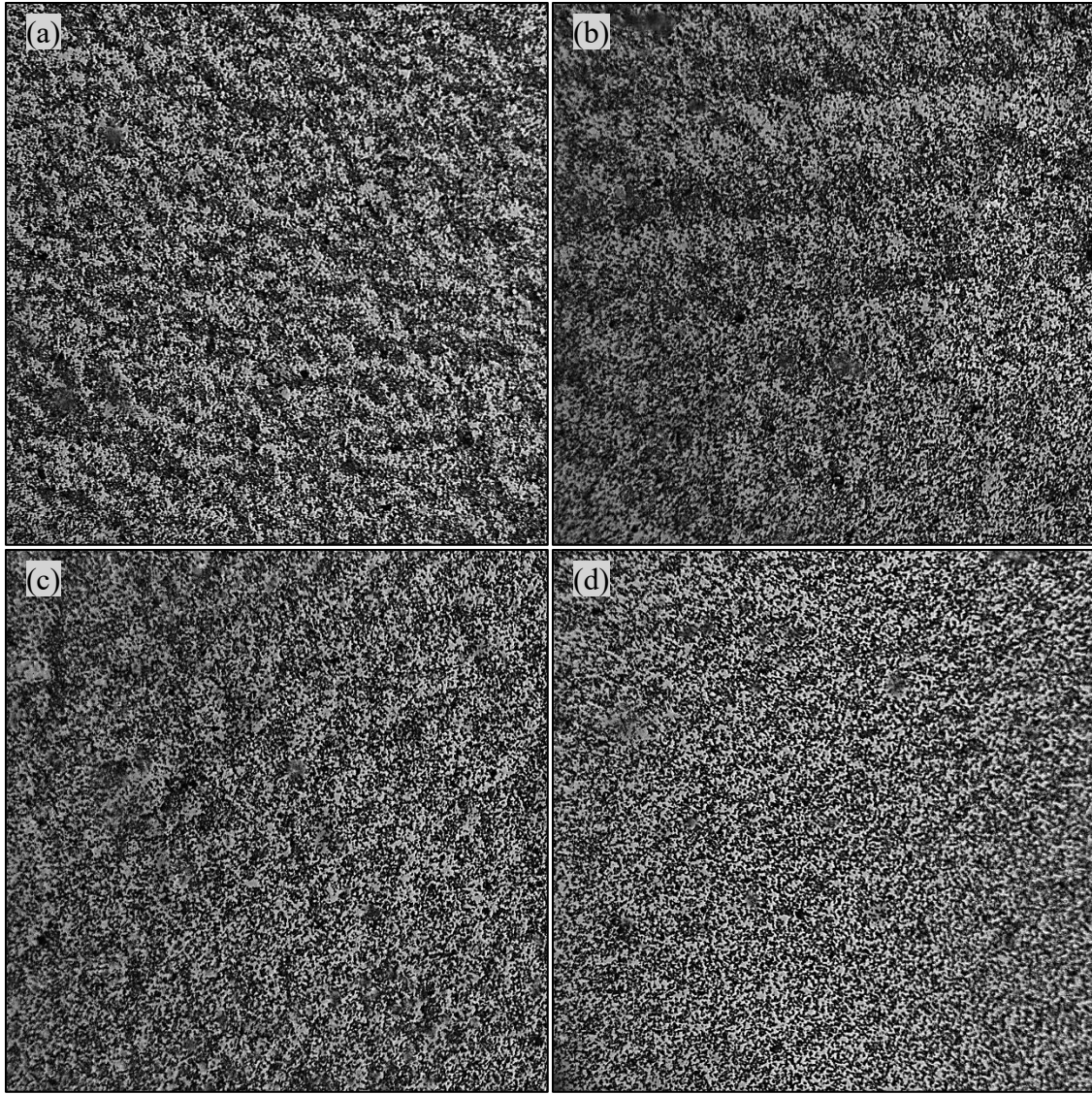


Figure 4.13. Microscopy images (4x magnification) of the binary systems of BC-SSQ microparticles ($\phi_{\text{micro}}=10^{-3}$) and ZrO_2 nanoparticles ($\phi_{\text{nano}} = 10^{-3.26}$) (a) before and (b) after 60°C (c) after 70°C (d) after 80°C temperature shock cycles.

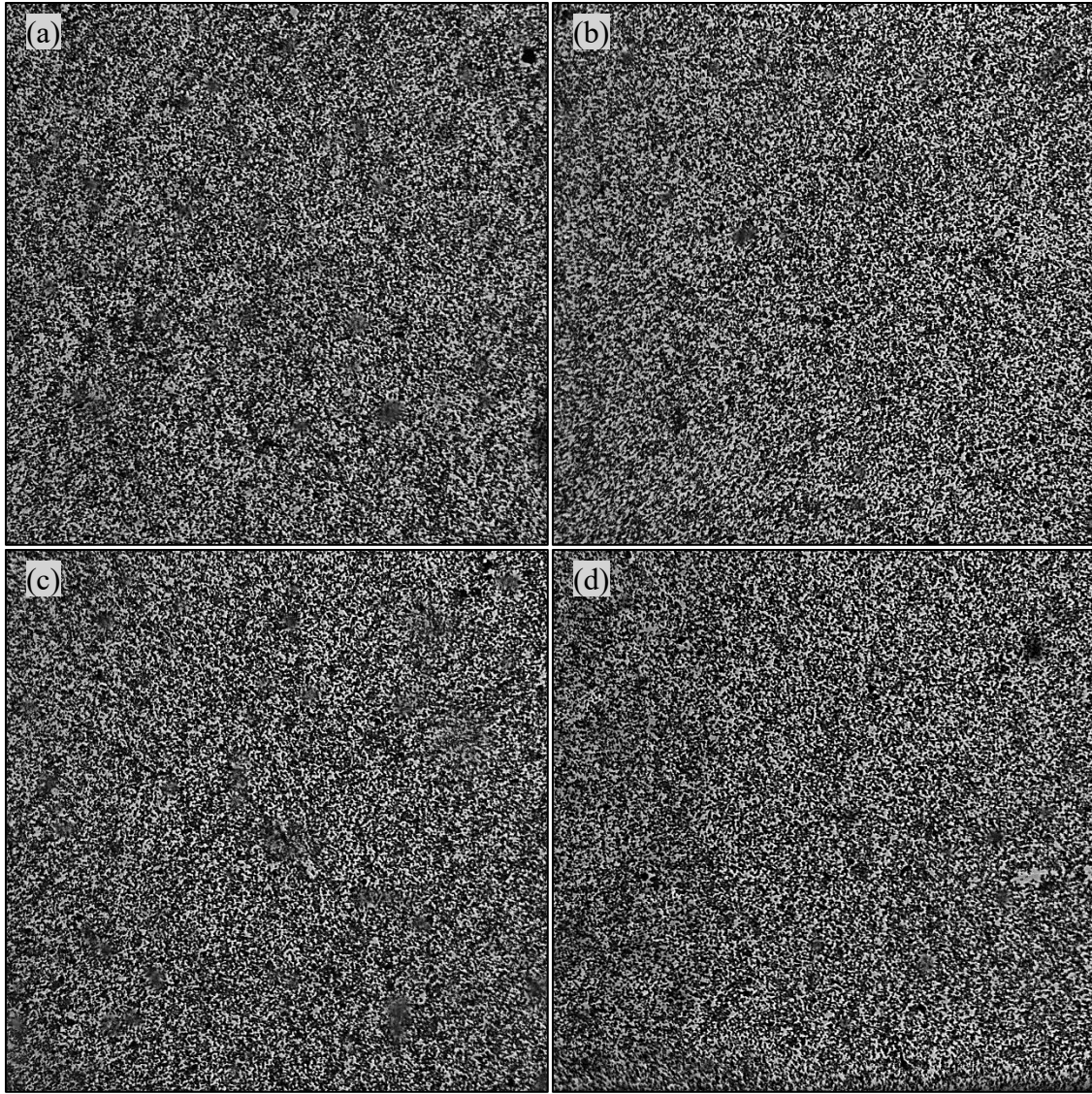


Figure 4.14. Microscopy images (4x magnification) of the binary systems of BC-SSQ microparticles ($\phi_{\text{micro}}=10^{-3}$) and ZrO_2 nanoparticles ($\phi_{\text{nano}} = 10^{-3}$) (a) before and (b) after 60°C (c) after 70°C (d) after 80°C temperature shock cycles.

4.4. CONCLUSION

The temperature shock experiments showed that the applied heat has an impact on the nanoparticle haloing binary systems. We started our temperature shock experiments with aggregated samples, and it was observed that by increasing the temperature of the samples, the individual particles and smaller aggregates moved faster than the bigger

aggregates. In addition, smaller aggregates and individual particles seemed to reaggregate at a higher rate than the bigger aggregates.

Heat conduction is a form of diffusion in which thermal energy is transferred, which is similar to mass diffusion but with much faster rates. Therefore, the growth rate of the aggregation and possible crystallization at an elevated temperature can be much faster than that due to the diffusion at room temperature ¹¹⁰.

As discussed in the previous section, the average blob size increased with applying the temperature shock to the samples. By increasing the temperature shock from 60°C to 80°C, the average blob size growth was more significant. The average blob size growth was higher in the nanoparticle haloing samples with the lowest nanoparticle concentration ($\phi_{\text{nano}} = 10^{-4}$). Samples with the highest nanoparticle concentration ($\phi_{\text{nano}} = 10^{-3}$) seemed very stable, and temperature shock had a minimum effect on their average blob size. In addition, the relative coarseness of the network reduced sharply after the temperature shock. This coarseness reduction could mean that applying the temperature shock would result in a more idealized structure with higher crystallinity. Unfortunately, we did not have the tools to observe the sediments' 3-D structures in order to measure the crystallinity. Still, after a single ramp and soak, the binary systems seemed to be more even in their structure.

By directly determining the degree of crystallinity of the samples using in situ X-ray scattering observation or using a confocal microscope with a narrow Z slicing capability and higher magnifications, we can better understand the structure and crystallinity of the binary systems ^{6, 111}. However, these are beyond the scope of this study and would be a direction for future research.

CHAPTER 5

MOLECULAR DYNAMICS SIMULATIONS OF NANOPARTICLE HALOING BINARY SYSTEMS

5.1. INTRODUCTION

Aggregation is a property of colloidal dispersions that depends on the interactions between the particles. In the absence of repulsion interactions, van der Waals interactions between particles result in the aggregation and phase separation. Electrostatic repulsive interactions are needed in order for colloidal dispersion to be stable.^{2, 12, 13.}

In nanoparticle haloing, charged nanoparticles have been found to enhance the stability of colloidal suspensions by forming a non-adsorbing layer surrounding neutral colloids, which induces an electrostatic repulsion between the neutral colloids³⁴. This stabilization mechanism has been primarily applied to silica-zirconia binary systems, though others have been investigated⁶. It is found that the silica-zirconia binary suspension system could be stabilized by highly charged nanoparticles at volume fractions ranging from 10^{-5} to 10^{-2} . At low nanoparticle volume fractions (10^{-5} to 10^{-4}), there is a minor amount of adsorption, and colloidal stabilization is dominated by nanoparticle haloing. At high nanoparticle volume fractions ($\sim 10^{-2}$), the colloidal surface is significantly occupied by the adsorbing nanoparticles, and instead of nanoparticle haloing, the increased surface

charge is primarily induced by nanoparticles that are directly adsorbed onto the silica surfaces; Therefore, adsorption will overcome nanoparticle haloing in this region. There is a transition region around a nanoparticle volume fraction of 10^{-3} , within which the stabilization mechanism can be influenced by both nanoparticle haloing and adsorption³⁴.

We can study the properties of many-particle systems using computer simulations. Particle simulations provide particle positions, potential energies, and kinetic energies at specific time points. These data can be analyzed to calculate theoretical macroscopic properties. Utilizing statistical mechanics makes it possible to calculate the macroscopic properties (bulk) of pure substances and mixtures based on their microscopic properties and interactions. The microscopic properties of a molecule or a colloidal particle include its configuration, geometry, intraparticle forces, and interparticle forces. Statistical mechanics employs probability theory to predict the distribution of molecular motions in a multi-molecule system. It provides a means for averaging the states so that macroscopic (bulk) properties such as temperature and free energy can be obtained.^{112, 113}

For condensed systems, including aqueous and nonaqueous solutions, statistical mechanics simulations have become increasingly important tools. Computer simulations, such as Monte Carlo (MC) and molecular dynamics (MD), can be useful in determining the effective pair potential between colloids, which will be particularly interesting for the problems explored in this chapter¹¹⁴.

Alder and Wainwright first introduced the MD method in the late 1950s to study the interactions of hard spheres. Their MD simulations found evidence for a solid-fluid phase transition that had not been observed previously and with MC simulations^{115, 116}. In 1964, Rahman and Stillinger used Lennard Jones potentials to do the first MD simulation

of a liquid argon system ¹¹⁷. They showed how to compute important MD properties such as radial distribution function (RDF), which gives the probability of finding a particle at a given distance from another particle ^{6, 118}.

MD simulations allow us to measure observable quantities as functions of the motions and positions of the particles within a system. In particular, MD simulations are used to determine the properties of substances in solution ¹¹⁹. MD is a method for calculating the equilibrium and transport properties of a many-body system. MD simulations estimate the time-dependent behavior of molecular or particulate systems. In these simulations, every colloidal particle will be taken into consideration, and the force and potential between two particles are a function of their separation distance ^{120, 121}.

The first step in MD simulations is to start a model system by defining the number of particles and their initial positions ^{*}, and velocities. All the velocities are then shifted to a zero momentum, and then resulting velocities are scaled to adjust the mean kinetic energy of the system to the desired value. In the thermal equilibrium condition, the following relation will hold ¹¹³:

$$k_B T(t) = \sum_{i=1}^N \frac{m_i v_{\alpha,i}^2(t)}{N_f} \quad (5-1)$$

Where k_B is the Boltzmann constant, m_i is the particle mass, $v_{\alpha,i}$ is the α component of the velocity of particle i . N is the number of particles, and N_f is the number of degrees of freedom ¹¹³.

The next step of the simulation, which is often the most time-consuming part of the MD simulations, is computing the force applied to each particle. If two particles are close

* Particle are often placed on a cubic lattice

enough to interact (within a user-defined cutoff or truncation distance), the force between them needs to be calculated. After computing all forces between the particles, the next step is solving Newton's equations of motions for the system (i.e., $F = ma$). Alternative Langevin formulations also exist to account for frictional forces such as drag ($m \frac{dv}{dt} + \gamma v(t) = \xi(t)$ where v is the velocity, $\gamma = 6\pi\eta r$ and $\xi(t)$ is the random force induced by the fluid on the Brownian particles)¹²². By using this force and the position of particles at the current and previous time steps, the positions of particles at the next step will be predicted using numerical integration. For each step, the temperature and the total energy will be calculated as functions of velocities and particle positions^{113, 123}.

Similar to MD, MC simulations are used for studying the properties of particles¹²⁴. The major difference is that MC relies on the equilibrium statistical mechanics and not the MD; therefore, time evolution is not captured by MC. MC relies on repeated random sampling to represent a target probability distribution. Random moves in MC simulations can be accepted or rejected based upon user-defined criteria. The Metropolis criterion is often used, which always accepts trial configurations with lower potential energies and probabilistically accepts trials with higher potential energies^{113, 125}.

In general, MC or MD are chosen based on the phenomenon under investigation, but there are some situations where one of these methods is preferable. For example, for an aqueous system simulation where particles are crowded within the simulation box, MD simulations are preferable because the molecular collisions in MD exchange energy between molecules, allowing molecules to cross barriers dynamically. But in MC, there is a high probability that the random moves cause the particles to overlap with neighboring particles, causing a spike in the system's potential energy and increasing the probability of

rejecting a trial move. These rejected moves significantly decrease the efficiency of sampling in MC for crowded systems such as those in the condensed phase ¹¹³.

In the previous simulations of binary colloidal mixtures, the effective repulsions induced by lower nanoparticle volume fractions ($\phi_{\text{nano}} < 10^{-3}$) were not investigated. In addition, van der Waals interactions between particles are excluded in the previous studies, and only electrostatic forces are taken into account in a MC scheme ^{6, 50, 121, 126}. The effective colloidal pair potentials are calculated from the RDF $g(D)$, also known as pair correlation function, in those studies.

In our nanoparticle haloing binary systems with higher nanoparticle volume fractions ($\phi_{\text{micro}} > 10^{-4}$), there are high energy barriers between the microparticles. Therefore, it will take a long time for the MD simulations to walk through all possible molecular states. We used an enhanced method called umbrella sampling to improve the sampling of system configurations. Umbrella sampling is a useful technique to accelerate the sampling by allowing the system to remain in states that would otherwise be rare due to potential barriers. The umbrella sampling technique developed by Torrie and Valleau in 1977 ¹²⁷ is a biased methodology in computational physics and chemistry for overcoming sampling problems by modifying the potential function so that the unfavorable states are sampled adequately ¹¹³.

Our group previously used AFM to investigate the interactions between negligibly charged silica microparticles in aqueous solutions and in the presence of highly charged zirconia nanoparticles. ³⁴

In this study, equilibrium properties of binary system of 1000 nm silica particles and 10 nm zirconia nanoparticles were evaluated by MD simulations using a DLVO

potential in HOOMD-blue. This model includes van der Waals and electrostatic interactions, and the model parameters are developed based on our previous experimental measurements³⁴. The main purpose of our simulations is to determine the effective pair potential between colloidal particles induced by the nanoparticles using the umbrella sampling technique.

5.2. THEORY

5.2.1. INTERACTIONS BETWEEN PARTICLES

In the present study, we employed MD simulations based on the DLVO theory to study the equilibrium properties of the binary system of neutral silica microparticles and highly charged zirconia nanoparticles (+70 mV). Both microparticles and nanoparticles are modeled as hard spheres with diameters of 1000 nm and 10 nm, respectively.

DLVO theory describes the total interaction energy between two colloidal particles as the sum of van der Waals (V_{vdW}) energy and the electric double layer interaction energy ($V_{electro}$)¹²⁸:

$$V_{total} = V_{vdW} + V_{electro} \quad (5.1)$$

Interaction force is the negative of the derivative of the potential energy:

$$F = -\frac{dV}{dD} \quad (5.2)$$

Therefore, the total interaction force between two particles can be written as:

$$F_{total} = F_{vdW} + F_{electro} \quad (5.3)$$

Van der Waals interactions:

Van der Waals attraction potentials and forces between two microparticles (equal-sized) and between microparticle-nanoparticle (two unequal-sized particles) are calculated from equation 5.4 to equation 5.7^{129, 130}.

$$V_{vdW,micro} = -\frac{A_{micro}R}{12D} \left[\frac{4R}{(D+4R)} + \frac{4RD}{(2R+D)^2} + \frac{2D}{R} \ln \left(\frac{D(D+4R)}{(2R+D)^2} \right) \right] \quad (5.4)$$

$$F_{vdW,micro} = -\frac{A_{micro}R}{12D^2} \left[\frac{4R}{(D+4R)} + \frac{4RD}{(2R+D)^2} + \frac{2D}{R} \ln \left(\frac{D(D+4R)}{(2R+D)^2} \right) \right] + \frac{A_{micro}R}{12D} \left[\frac{-4R}{(D+4R)^2} + \frac{4R}{(2R+D)^2} + \frac{8RD}{(2R+D)^3} + \frac{2}{R} \left(\frac{D}{D+4R} - \frac{2x}{D+2R} + 1 \right) + \frac{2}{R} \ln \left(\frac{D(D+4R)}{(2R+D)^2} \right) \right] \quad (5.5)$$

$$V_{vdW,micro-nano} = -\frac{A_{micro,nano}}{6} \left[\frac{2Ra}{r^2-(R+a)^2} + \frac{2Ra}{r^2-(R-a)^2} + \ln \left(\frac{r^2-(R+a)^2}{r^2-(R-a)^2} \right) \right] \quad (5.6)$$

$$F_{vdW,micro-nano} = -\frac{A_{micro,nano}}{6} \left[\frac{4Rar}{(r^2-(R+a)^2)^2} + \frac{4Rar}{(r^2-(R-a)^2)^2} + \frac{2r}{r^2-(R-a)^2} - \frac{2r}{r^2-(R+a)^2} \right] \quad (5.7)$$

R and a are the radii of microparticles and nanoparticles respectively, D is the surface-to-surface separation distance between microparticles, and r is the center-to-center separation distance between microparticle-nanoparticle ($r = D+R+a$). A_{micro} is the Hamaker constant of silica (0.8×10^{-20} J)²⁸, A_{nano} is the Hamaker constant of zirconia (7.28×10^{-20} J)¹³¹ and $A_{micro-nano}$ is the harmonic average Hamaker constant of silica and zirconia¹³²⁻¹³⁴.

Due to the small size and high zeta potential of the nanoparticles, the van der Waals interaction between them is negligible compared to the electrostatic interaction, and we ignored it.

Electrostatic double layer interactions:

Electrostatic double-layer interactions between two nanoparticles at a surface separation D are estimated by the Hogg-Healy-Fuerstenau (HHF) formula³⁰.

$$V_{electro,nano-nano} = 2\varepsilon_0\varepsilon_r\pi a\psi_{nano}^2 \ln[1 + \exp(-kD)] \quad (5.8)$$

For $kD \gg 1$, this equation reduces to:

$$V_{electro,nano-nano} = 2\varepsilon_0\varepsilon_r\pi a\psi_{nano}^2 \exp(-kD) \quad (5.9)$$

Therefore, electrostatic force between two nanoparticles will be given by:

$$F_{electro,nano-nano} = 2k\varepsilon_0\varepsilon_r\pi a\psi_{nano}^2 \exp(-kD) \quad (5.10)$$

ε_0 is the vacuum permittivity, ε_r is the dielectric constant of water, ψ_{nano} is the zeta potential of zirconia, and k is the reciprocal of the Debye length.

Since the silica microparticles are negligibly charged, the electrostatic interaction between them is insignificant, and we ignore it. However, due to the high charge difference between nanoparticles and microparticles, an attractive electrostatic double-layer interaction arises between them that ultimately leads to the formation of the nanoparticle halo around the microparticles. This attraction interaction for $R/a \gg 1$ is determined by⁵⁰:

$$V_{electro,micro-nano} = \varepsilon_0\varepsilon_r\pi a\psi_{nano}^2 \ln[1 - \exp(-2kD)] \quad (5.11)$$

For $kD \gg 1$, this equation reduces to:

$$V_{electro,micro-nano} = -\varepsilon_0\varepsilon_r\pi a\psi_{nano}^2 \exp(-2kD) \quad (5.12)$$

The electrostatic force between microparticle-nanoparticle will be:

$$F_{electro,micro-nano} = -2k\varepsilon_0\varepsilon_r\pi a\psi_{nano}^2 \exp(-2kD) \quad (5.13)$$

Depletion interactions:

An attractive depletion interaction, which is not included in DLVO, arises between microparticles in a nanoparticle suspension. When the nanoparticles cannot pass through the gap between two microparticles, the solvent will be forced out. This creates an osmotic

pressure that leads to an attraction between microparticles. The depletion interaction between two microparticles is given by the Asakura and Oosawa potential ¹³⁵:

$$V_{depletion} = \begin{cases} \rho_{\infty} kT \pi \left[2aRD - \frac{RD^2}{2} - \frac{4a^3}{3} + a^2D - \frac{D^3}{12} - 2a^2R \right] & \text{for } 0 \leq D \leq 2a \\ 0 & \text{for } D > 2a \end{cases} \quad (5.14)$$

$$F_{depletion} = \begin{cases} -\rho_{\infty} kT \pi \left[2aR - RD + a^2 - \frac{D^2}{4} \right] & \text{for } 0 \leq D \leq 2a \\ 0 & \text{for } D > 2a \end{cases} \quad (5.15)$$

Where ρ_{∞} is the bulk number density, and kT is the thermal energy. The effect of depletion interactions was ignored in our simulations because the depletion interaction is relatively weak compared to the van der Waals interaction. At the highest nanoparticle concentration ($\varphi_{\text{nano}} = 10^{-3}$), the maximum value of depletion force in $0 \leq D \leq 2a$ separation distance region was much smaller than the minimum value of van der Waals force in that region (~30 times smaller).

5.2.2. UMBRELLA SAMPLING

One of the main purposes of our simulations was to determine the effective pair potentials or potential of mean force (PMF) between colloidal particles induced by the nanoparticles. PMF is the free energy of the system along a particular coordinate (known as the reaction coordinate) and is most commonly a spatial coordinate ^{136, 137}.

It is difficult to sample the full conformational space in the systems with significant energy barriers, and the high-energy configurations will be poorly sampled when simulating these systems. Umbrella sampling is a widely used technique to improve the sampling of systems with high potential barriers ^{127, 138}.

In our study, we used umbrella sampling for the nanoparticle haloing binary systems due to the significant free energy barriers, especially at higher nanoparticle

concentrations. For umbrella sampling in our systems, the distance between two microparticles was divided into a series of values. Therefore, rather than conducting one simulation, many independent simulations are considered. Each simulation is meant to explore a narrow range of phase space along the reaction coordinate. An external potential was then applied to retain the distribution near the set value. The modification of the potential function $V(D)$ can be written as ^{113, 127, 139}:

$$V_{bias}(D) = V(D) + W(D) \quad (5.16)$$

Where $V_{bias}(D)$ is the bias potential along the separation distance D . $W(D)$ is a harmonic restraint function with a strength of K and a reference point of D_0 , which often takes a quadratic form ^{113, 127, 139}:

$$W(D) = K(D - D_0)^2 \quad (5.17)$$

To ensure sampling in all the distances, we need to keep each system close to its reference point with a choice of K that results in the potential energy distributions of the adjacent windows to overlap. Umbrella sampling simulations compute the biased probabilities of the systems. The unbiased free energy could be obtained by unbiasing these biased probabilities ^{139, 140}. Once the umbrella sampling simulations are performed with the restraining biases, histograms of the reaction coordinates are constructed, and each distribution is weighted, stitched, and corrected to obtain the unbiased probability distribution and associated free energy profile ¹³⁸. This method is called the weighted histogram analysis method (WHAM) ^{139, 141}.

Using the umbrella sampling results of the binary systems, a continuous PMF as a function of microparticle-microparticle distances will be constructed ¹³⁹. In fact, umbrella sampling calculates the PMF based on rigorous probability calculations over the separation

distance. PMF or the effective pair potential (V_{eff}) for diluted colloidal systems is calculated from the colloidal pair correlation(RDF) $g(D)$ derived from the simulations results of the binary systems^{50, 142}.

$$V_{eff} = -kBT \ln g(D) \quad (5.18)$$

A cubic box with $\varphi_{micro} = 10^{-2}$ and different nanoparticle concentrations from $\varphi_{nano} = 10^{-6}$ to 10^{-3} was employed which involved 2 microparticles and up to 2×10^5 nanoparticles. Both silica microparticles and zirconia nanoparticles were modeled as hard spheres with 1000 nm and 10 nm diameters, respectively.

The distance between two microparticles ($6 \leq D \leq 50 \text{ nm}$) was split into 44 windows spaced by 1 nm, restraining the surface-to-surface separation distance of two microparticles. A simulation was performed for each window. Bias potentials constrain the system's center of mass in each window and at the same time connect energetically different regions in phase space. The restraining potential was harmonic with a force constant $K = 10 \text{ kJ/mol.nm}^2$ for $6 < D \leq 20 \text{ nm}$ and $K = 1 \text{ kJ/mol.nm}^2$ for $20 < D < 50 \text{ nm}$. The simulation run time for each window was 20 ms with time steps of 0.1 ns. Langevin dynamics were used to adjust the temperature and temperature was kept constant at 298 K (25°C).

The PMF along separation distance (D) was then obtained by submitting umbrella sampling output to WHAM analysis¹³⁹.

5.2.3. MD AGGREGATION STUDIES

Stabilization and aggregation behavior of the nanoparticle haloing binary systems were studied for systems of 125 microparticles using MD by applying PMF curves from

the umbrella sampling. Thus, the stabilizing effects of nanoparticles were preserved while their physical presence in the simulation box was no longer required. The simulation run time for each window was 1 *min* with time steps of 10 *ns*.

PMF, which is equal to the Helmholtz free energy (A) of the system, incorporates an entropic term $-T\Delta S$ which at the isothermal condition is given by:

$$\Delta A = \Delta U - T\Delta S \quad (5.19)$$

U is the internal energy and includes kinetic energy and potential energy. At constant temperature, kinetic energy is constant and can be ignored. Potential energy reflects interactions between solvent molecules and particles as well as between particles themselves¹⁴³.

To reduce the degrees of freedom in the systems and to eliminate the fastest motions, we developed a coarse-grained (CG) force field for each of the nanoparticle-microparticle systems. This new CG force field reduces the number of particles by a factor of 10^5 , 10^4 , and 10^3 for systems with 10^{-3} , 10^{-4} , and 10^{-5} respectively. The timestep for integration was also increased from 0.1 ns to 10 ns. Through the use of the CG force field, we observe a 10^5 to 10^7 -fold increase in simulation throughput, thus allowing us to explore phenomena on the minute rather than millisecond timescale¹⁴⁴⁻¹⁴⁶.

To construct the CG force field, the potential of mean force (PMF) was used to approximate $V_{\text{micro-micro}}$ in a similar fashion to the more widely used Boltzmann inversion method. In Boltzmann inversion, the radial distribution function of an atomistic system is converted to a PMF by the transformation $w = -kT \ln(g(r))$ as a first approximation of CG potentials. Then, the first approximation is iteratively refined by comparing atomistic and CG radial distribution functions^{145, 147}.

Because the phenomena under consideration in this study are rate limited by large free energy barriers, intermediate states are rarely observed in standard MD simulations, and the radial distribution function is incomplete, making Boltzmann inversion prone to high statistical error in this region. Thus, rather than using Boltzmann inversion, a PMF from umbrella sampling is used instead to ensure complete sampling of the intermediate region. While the umbrella sampling-derived PMF provides a good first approximation for the microparticle-microparticle potential, it does not allow for further iterative refinement as with Boltzmann inversion. However, due to the relatively simple nature of the potentials in our system compared to the cases in which iterative Boltzmann inversion is most commonly used (e.g., for polymers and biomolecules rather than colloids), we hypothesize that the umbrella sampling-derived first approximation is sufficient to observe nanoparticle-induced kinetic barriers to aggregation^{145, 148-150}.

MD simulations were performed at constant temperature of 298 K for the 3 different nanoparticle haloing systems ($\varphi_{\text{micro}} = 10^{-2}$, $\varphi_{\text{nano}} = 10^{-5}$, 10^{-4} , 10^{-3}). Langevin dynamics were used to adjust the temperatures.

5.3. RESULTS AND DISCUSSION

5.3.1. INTERACTIONS BETWEEN PARTICLES

Interaction energies between particles based on the DLVO theory are presented in **Figure 5.1**. Since the silica microparticles are negligibly charged, we ignored their electrostatic interactions. Therefore, the interaction between microparticles is purely attractive. The electrostatic forces between nanoparticles are very large due to the high zeta potential of these particles. The van der Waals forces between nanoparticles are negligible

compared to the electrostatic force, thus we ignored it. There is an attraction between highly charged nanoparticles and negligibly charged microparticles due to the electrostatic double-layer interaction between them. It is this attraction interaction that ultimately leads to the formation of the nanoparticle halo around the microparticles.

The van der Waals attractive interactions between two microparticles and between a microparticle and a nanoparticle will cause the particles to overlap when they are very close. In order to avoid overlapping of the particles, we added a repulsive interaction at the close distances ($\sim 2\text{nm}$) so the total forces approach infinity when particles overlap.

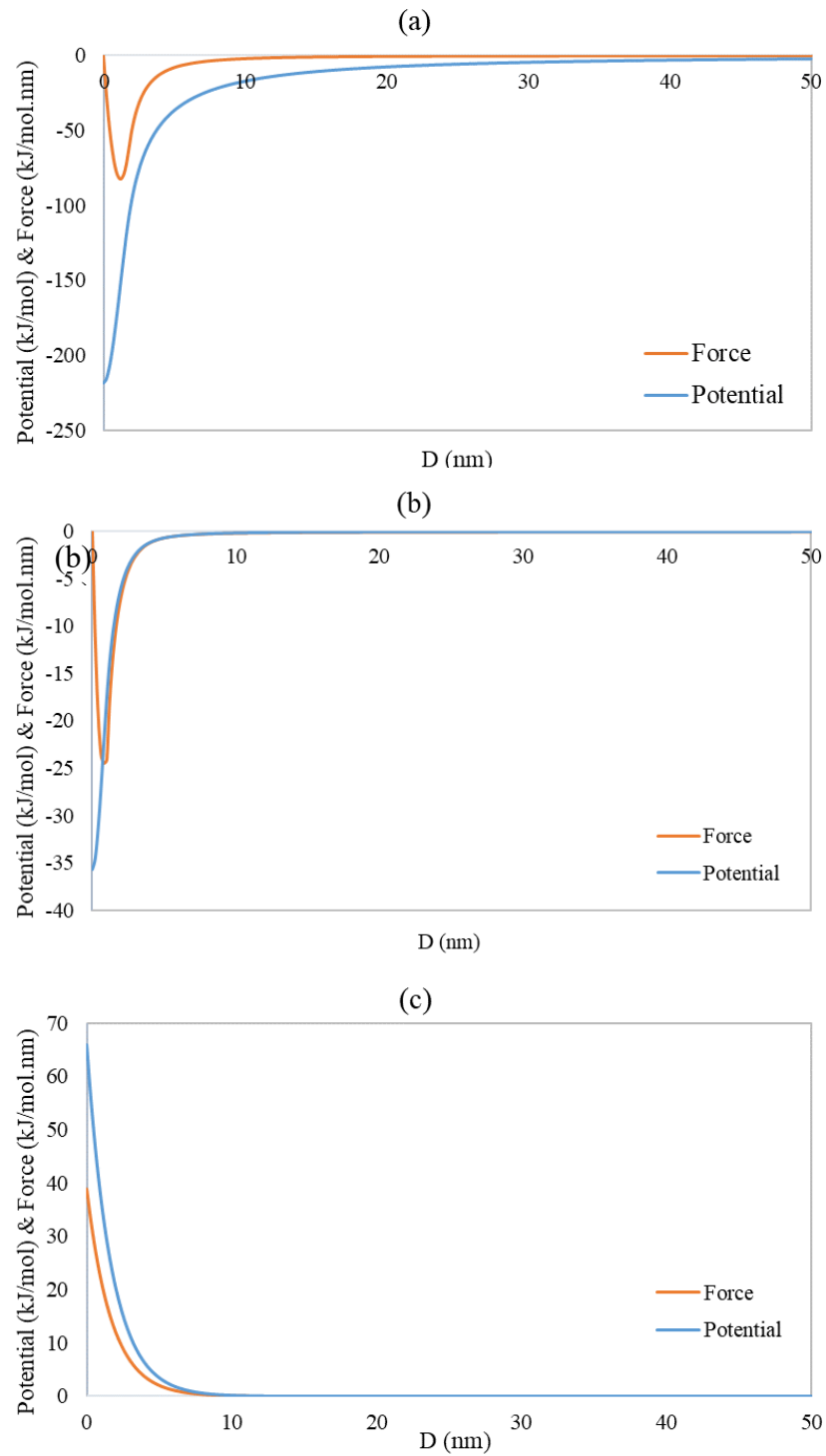


Figure 5.1. Interaction energies and forces between (a) two microparticles (b) a microparticle and a nanoparticle (c) two nanoparticles

5.3.2. UMBRELLA SAMPLING

An illustration of the umbrella sampling simulations is shown in **Figure 5.2**. It can be seen that nanoparticles are forming uniform layer around the microparticles. A depletion of nanoparticles happened in the gap between the microparticles at smaller separation distances.

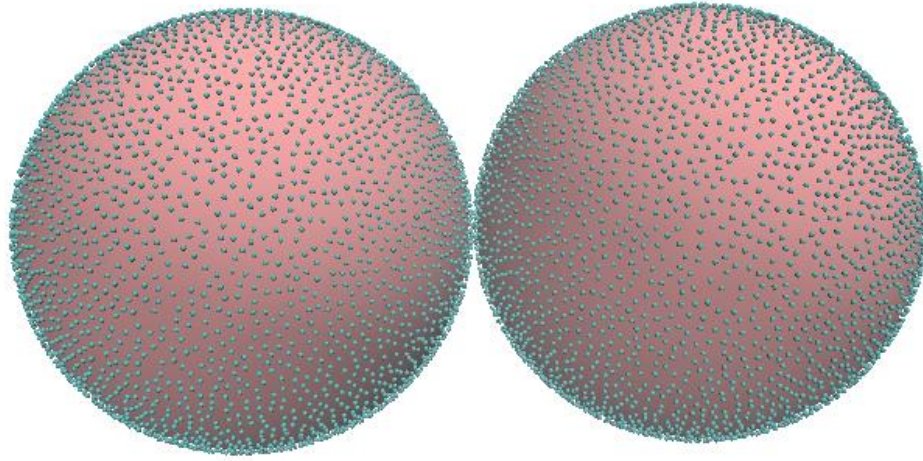


Figure 5.2. A rendering of the umbrella sampling simulation output for the binary system of $\varphi_{\text{micro}} = 10^{-2}$ and $\varphi_{\text{nano}} = 10^{-3}$ and separation distance of 20 nm. Figure is rendered in VMD using the Tachyon renderer.

Figure 5.3 shows a sample histogram graph of the umbrella sampling windows. The histograms show an appropriate overlap between all the adjacent windows, which is a requirement for the convergence of WHAM.

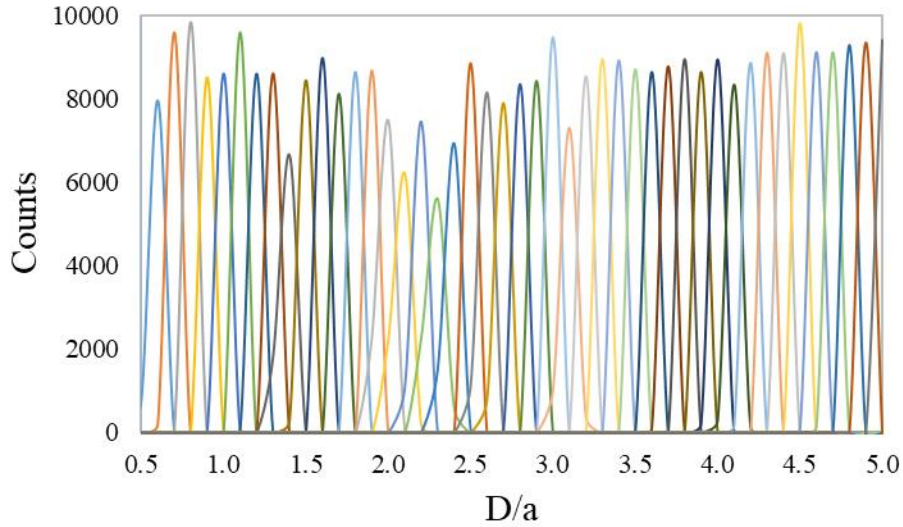


Figure 5.3. Histograms of the configurations within the umbrella sampling windows with 44 bins, for the binary system with $\varphi_{\text{nano}} = 10^{-6}$

Figure 5.4 shows the effective potential between a pair of colloidal microparticles as a function of surface-to-surface separation (D), for different nanoparticle concentrations. The obtained results clearly show that the nanoparticles induce a repulsive barrier between the microparticle. This barrier increases with increasing the volume fraction of nanoparticles and it reaches $6.5 k_{\text{B}}T$ at the highest nanoparticle concentration of $\varphi_{\text{nano}} = 10^{-3}$.

At low nanoparticle volume fractions ($\varphi_{\text{nano}} = 10^{-6}, 10^{-5}$), the repulsive barrier arises at a separation distance of 20 nm ($D/a=2$). By increasing the nanoparticle volume fraction, the barrier becomes wider, and it arises at ~ 40 nm separation distance. This repulsive barrier is strong enough to prevent gelation and lead to stabilization.

The repulsive barrier between the microparticles is a result of the nanoparticle haloing where nanoparticles form a nonadsorbing nanoparticle layer around neutral

colloidal particle, which presents as an effective surface charge and produces an electrostatic repulsion that mitigates the inherent van der Waals attraction between them.

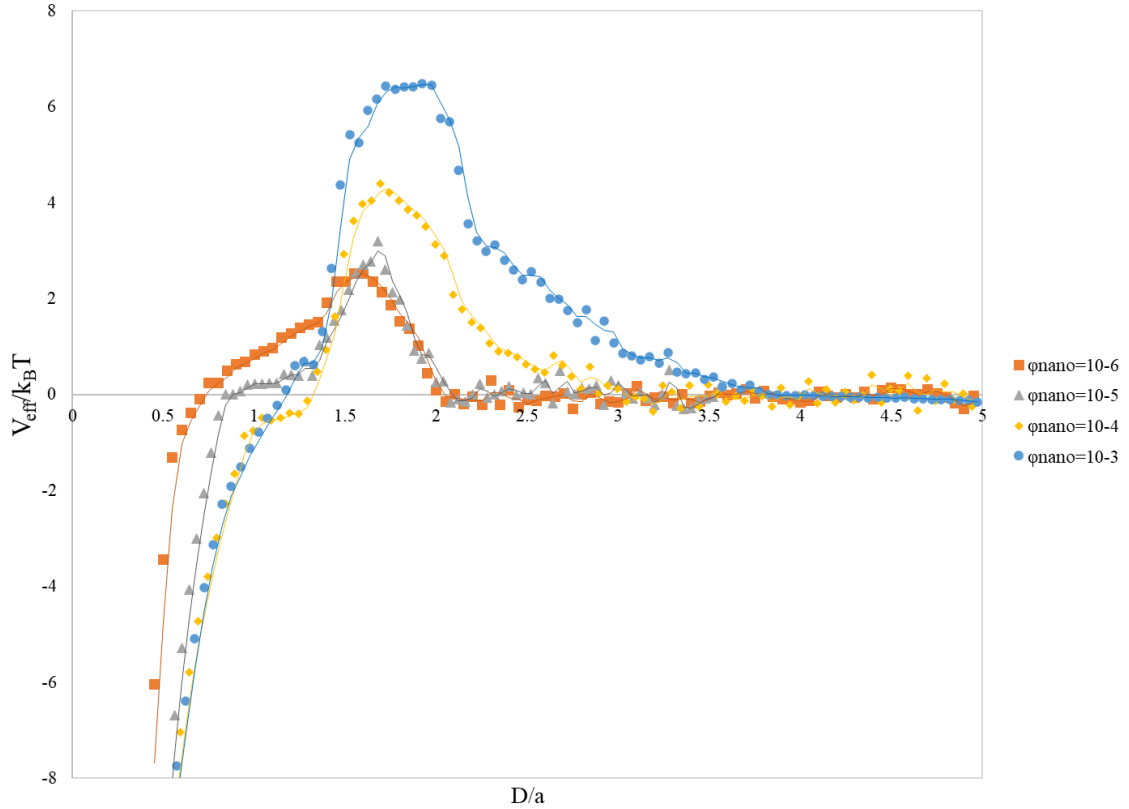


Figure 5.4. The effective potential between a pair of silica colloidal particles as a function of zirconia nanoparticle volume fraction and separation distance

5.3.3. MD AGGREGATION STUDIES

Snapshots of MD simulations results for nanoparticle halving binary systems with $\varphi_{\text{nano}} = 10^{-5}$, 10^{-4} , and 10^{-3} are shown in **Figure 5.5**. At highest nanoparticle volume fractions, the rate of aggregation and the number of aggregates decreased significantly in simulations. This observation is in agreement with the confocal images of these system where the number of aggregates decreased by increasing the nanoparticle volume fractions and at the highest nanoparticle volume fraction, the system was stabilized.

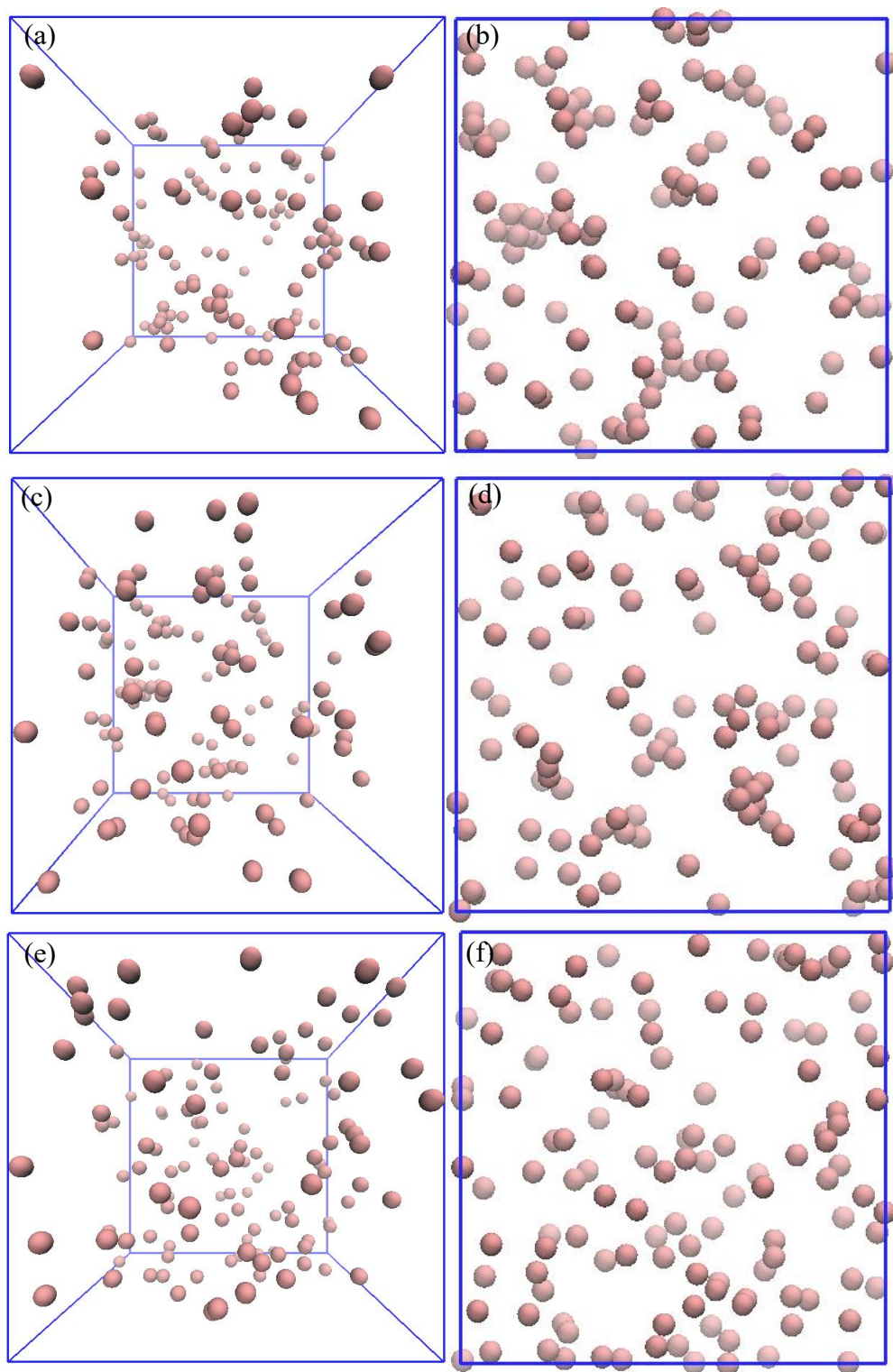


Figure 5.5. 3D and 2D Snapshots of MD simulations boxes filled with microparticles at nanoparticle volume fractions of (a,b) $\varphi_{\text{nano}} = 10^{-5}$ (c,d) $\varphi_{\text{nano}} = 10^{-4}$ (e,f) $\varphi_{\text{nano}} = 10^{-3}$

5.4. CONCLUSION

This study focuses on the stability of neutral colloidal silica microparticles in aqueous suspensions with low concentrations of highly charged zirconia nanoparticles. DLVO theory modified with additional depletion interactions was applied to describe particle interaction potentials and forces.

Previous AFM measurements^{5, 46} identified and quantified an effective repulsion between microparticles that increased as nanoparticle concentration increased, suggesting that charged nanoparticles can be used to modulate the stability of microparticle suspensions. To better understand the mechanisms by which the effective repulsion arose, MD simulations were performed. Systems containing $\phi_{\text{micro}} = 10^{-2}$ and $\phi_{\text{nano}} = 10^{-6}$ to 10^{-3} were simulated over timescales up to 1 minute. In the absence of nanoparticles, microparticles quickly aggregated during simulations. However, even in the smallest concentration of nanoparticles studied, an apparent kinetic barrier arose that slowed microparticle aggregation significantly.

To quantify the apparent kinetic barrier and the effective pair interactions between microparticles in the presence of nanoparticle halos, enhanced sampling was employed. Umbrella sampling was used to ensure sampling of rare states and to construct a continuous PMF as a function of microparticle-microparticle distances. Simulation results indicated a kinetic barrier ranging from about 2.5 to 6.5 $k_B T$ exists for microparticle-microparticle interactions. This barrier grows as nanoparticle concentrations increase, suggesting that nanoparticle concentration is a driving factor in stabilizing microparticle suspensions as was observed in atomic force microscopy experiments.

Ultimately, stabilization and aggregation were studied for systems of 125 microparticles using MD by applying PMF curves from the umbrella sampling. Thus, the stabilizing effects of nanoparticles were preserved while their physical presence in the simulation box was no longer required. Simulations indicate that the kinetic barriers found during umbrella sampling simulations affect the rate of microparticle aggregation, matching experimental observations.

CHAPTER 6

CONCLUSION AND FUTURE WORK

6.1. CONCLUSION

In this work, the effect of temperature and nanoparticle concentration on the stabilization of binary systems of colloids and nanoparticles with possible nanoparticle haloing was investigated using experimental techniques and molecular dynamics simulations. The specific aims of this project were to:

1. Prepare nanoparticle haloing samples for NASA experiments
2. Conduct gravity temperature shock experiments
3. Perform molecular dynamics simulation of the nanoparticle haloing systems using HOOMD-blue to determine the effective colloidal pair potential.

The deliverables of each of these specific aims are explained below.

ISS Experiments Sample Preparation:

After synthesizing and characterizing silsesquioxane microparticles, gravity settling experiments were performed in order to choose the most stable nanoparticle haloing binary systems for the ISS and gravity experiments. Gravity settling experiments showed that microspheres aggregate and settle rapidly due to the van der Waals interactions in the absence of nanoparticles, yielding open sediment structure clusters. By adding the

nanoparticles to the system, the normalized settling velocity decreased due to the effective potential barrier that arises from nanoparticle halo formation. Microscopy images indicated a possibility of achieving some level of crystallization in the nanoparticle haloing systems.

Based on the ground settling experiments, 1.2 μm BC-SSQ microparticles and 5-20 nm zirconia nanoparticles were selected for the nanoparticle haloing systems of this study and the ISS experiments. Based on the zeta potential results, the pH of these samples was high enough to meet the NASA safety requirements.

Gravity Temperature Shock Experiments:

Effect of temperature on nanoparticle haloing binary systems was investigated using a confocal microscopy. Images were acquired before, during, and after the temperature shock. Image analysis of the results showed an increase in the average blob size after applying the temperature shock to the samples. By increasing the shock temperature from 60°C to 80°C, the average blob size growth was more significant. The average blob size growth was higher in the nanoparticle haloing samples with the lowest nanoparticle volume fraction ($\varphi_{\text{nano}} = 10^{-4}$). Samples with the highest nanoparticle volume fraction ($\varphi_{\text{nano}} = 10^{-3}$) were stable, and temperature shock had a minimum effect on their average blob size. In addition, the relative coarseness of the network reduced sharply after the temperature shock. This coarseness reduction could mean that applying the temperature shock would result in a more idealized structure with higher crystallinity. Further studies are needed to observe the sediments' 3-D structures in order to measure their crystallinity.

Molecular Dynamics Simulations:

To better understand the mechanisms by which the effective repulsion arose, molecular dynamics simulations were performed. Simulations results showed that in the absence of nanoparticles, microparticles quickly aggregate during simulations. However, even in the smallest concentration of nanoparticles studied, an apparent kinetic barrier arose that slowed microparticle aggregation significantly.

To quantify the apparent kinetic barrier and the effective pair interactions between microparticles in the presence of nanoparticle halos, enhanced sampling was employed. Umbrella sampling was used to ensure sampling of rare states and to construct a continuous PMF as a function of microparticle-microparticle distances. Simulation results indicated a kinetic barrier ranging from about 2.5 to 6.5 kBT exists for microparticle-microparticle interactions. This barrier grows as nanoparticle concentrations increase, suggesting that nanoparticle concentration is a driving factor in stabilizing microparticle suspensions as was observed in atomic force microscopy experiments.

Ultimately, stabilization and aggregation were studied for systems of 125 microparticles using molecular dynamics simulations by applying PMF curves from the umbrella sampling. Thus, the stabilizing effects of nanoparticles were preserved while their physical presence in the simulation box was no longer required. Simulations indicate that the kinetic barriers found during umbrella sampling simulations affect the rate of microparticle aggregation, matching experimental observations.

6.2. FUTURE WORK

There are still a lot of unknowns about the effect of temperature on the binary systems aggregation. Some of the experiments and simulations have been left for the future due to lack of time. The following ideas could be tested in the future.

AFM Studies:

Our group's previous study suggested when using highly charged nanoparticles to stabilize colloidal suspensions, the two fundamental mechanisms of nanoparticle haloing and adsorption are not mutually exclusive. Further studies are needed to fully elucidate the role of nanoparticle size and charge on the transition from stabilization by nanoparticle haloing to nanoparticle adsorption and observe how the nanoparticles behave during the transition process.

In addition, to determine the impact of thermal gradients on the stability of a nanoparticle haloing system, a series of AFM measurements can be conducted to directly measure the force between a particle and a surface as a function of temperature. Comparing forces with and without temperature gradients will allow us to determine if there are any additional attractive interactions.

Direct Determination of Colloid Crystallinity:

During the temperature shock studies of the binary systems, we were not able to quantify the binary systems structural evolution. By directly determining the degree of crystallinity of the nanoparticle haloing samples using in situ X-ray scattering observation or a confocal microscope with a narrow Z slicing capability and higher magnifications, we

can better understand the structure and crystallinity of the binary systems. This would also help us to indicate if there is a possibility of achieving some level of crystallization in these systems.

Conducting temperature Gradient Studies:

During this study, we did not have the capability to create a thermal gradient and promote thermophoresis. Initial attempts utilizing nichrome wire as our heating element were examined to regulate precise heating to the colloidal suspension. Other methods, such as the use of conductive carbon tape as an alternative heating element can be investigated as well. Once a precisely tunable heating element can be utilized to generate the appropriate temperature gradient to balance the particle settling velocities, the settling of the suspension could be studied.

Compare on earth temperature gradient results with the results from similar experiments onboard the ISS:

After performing the temperature gradient gravity experiments, the results need to be compared with the results from similar experiments which was performed onboard the ISS.

Further Molecular Dynamics Simulations:

The effect of temperature on the aggregation of nanoparticle haloing can be studied by doing molecular dynamics simulations at different temperatures. The effect of gravity can also be added to the future simulations by gradually decreasing the box size.

REFERENCES

1. Shaw, D. J., *Introduction to Colloid and Surface Chemistry*. fourth ed.; Butterworth-Heinemann: 2000.
2. Hunter, R. J., *Foundations of colloid science*. second ed.; Oxford: 2009.
3. Wennerström, D. F. E. H., *The Colloidal Domain Where Physics, Chemistry, Biology, and Technology Meet*. Second ed.; Wiley-VCH: 1999.
4. The Colloidal State. In *Enological Chemistry*, 2012; pp 303-321.
5. Hong, X.; Willing, G. A., Transition force measurement between two negligibly charged surfaces: a new perspective on nanoparticle halos. *Langmuir* **2009**, *25* (9), 4929-33.
6. Martinez, C. J.; Liu, J.; Rhodes, S. K.; Luijten, E.; Weeks, E. R.; Lewis, J. A., Interparticle interactions and direct imaging of colloidal phases assembled from microsphere-nanoparticle mixtures. *Langmuir* **2005**, *21* (22), 9978-89.
7. Martinez, C. J.; Lewis, J. A., Shape Evolution and Stress Development during Latex-Silica Film Formation. *Langmuir* **2002**, *18* (12), 4689-4698.
8. Lewis, J. A., Colloidal Processing of Ceramics. *J Am Ceram Soc* **2004**, *83* (10), 2341-2359.
9. Joannopoulos, J. D.; Villeneuve, P. R.; Fan, S., Photonic crystals: putting a new twist on light. *Nature* **1997**, *386* (6621), 143-149.
10. Müller, R. H., *Colloidal carriers for controlled drug delivery and targeting: modification, characterization, and in vivo distribution*. CRC Press: Boca Raton, FL, 1991.
11. Neerudu, N.; McNamara, L.; Hammer, N. I.; Rathnayake, H., A versatile synthesis to novel binary reactive groups functionalized silsesquioxane microparticles. *Sci. Adv. Today* **2017**, *3*, 25266.
12. Hunter, R. J., *Zeta potential in colloid science: principles and applications*. Elsevier Science: 2013.
13. Hunter, R. J., *Zeta potential in Colloid Science: Principles and Applications*. Academic Press Inc.: San Diego, CA 92101, 1988.
14. Pate, K.; Safier, P., Chemical metrology methods for CMP quality. In *Advances in Chemical Mechanical Planarization (CMP)*, Babu, S., Ed. 2016; pp 299-325.
15. He, Q. Investigation of stabilization mechanisms for colloidal suspension using nanoparticles. Dissertation, University of Louisville, 2014.
16. Singh, A. K., Structure, Synthesis, and Application of Nanoparticles. In *Engineered Nanoparticles*, 2016; pp 19-76.

17. Hadjittofis, E.; Das, S. C.; Zhang, G. G. Z.; Heng, J. Y. Y., Interfacial Phenomena. In *Developing Solid Oral Dosage Forms*, 2017; pp 225-252.
18. Hassan, P. A.; Rana, S.; Verma, G., Making sense of Brownian motion: colloid characterization by dynamic light scattering. *Langmuir* **2015**, *31* (1), 3-12.
19. Minor, M.; Leeuwen, H. P. V., Dynamics and kinetics. In *Volume IV: Particulate Colloids*, 2005; pp 4.1-4.53.
20. Adair, J. H.; Suvaci, E.; Sindel, J., Surface and Colloid Chemistry. In *Encyclopedia of Materials: Science and Technology*, 2001; pp 1-10.
21. Kiil, G. M. K. S., *Introduction to Applied Colloid and Surface Chemistry*. 1 ed.; Wiley: 2016.
22. McKee, C. T.; Walz, J. Y., Interaction forces between colloidal particles in a solution of like-charged, adsorbing nanoparticles. *J Colloid Interface Sci* **2012**, *365* (1), 72-80.
23. Lifshitz, E. M.; Hamermesh, M., The theory of molecular attractive forces between solids. In *Perspectives in Theoretical Physics*, 1992; pp 329-349.
24. Hough, D. B.; White, L. R., The calculation of hamaker constants from liftshitz theory with applications to wetting phenomena. *Advances in Colloid and Interface Science* **1980**, *14* (1), 3-41.
25. Evans, D. F.; Wennerström, H., *The Colloidal Domain: Where Physics, Chemistry, Biology, and Technology Meet*. 2nd ed.; Wiley: 1999.
26. Bergström, L., Hamaker constants of inorganic materials. *Advances in Colloid and Interface Science* **1997**, *70*, 125-169.
27. Wang, Q. J.; Chung, Y.-W., *Encyclopedia of Tribology*. 2013.
28. Leite, F. L.; Bueno, C. C.; Da Roz, A. L.; Ziemath, E. C.; Oliveira, O. N., Theoretical models for surface forces and adhesion and their measurement using atomic force microscopy. *Int J Mol Sci* **2012**, *13* (10), 12773-856.
29. Studying molecular-scale protein–surface interactions in biomaterials. In *Characterization of Biomaterials*, 2013; pp 182-223.
30. Hogg, R.; Healy, T. W.; Fuerstenau, D. W., Mutual coagulation of colloidal dispersions. *Transactions of the Faraday Society* **1966**, *62*.
31. Liufu, S.; Xiao, H.; Li, Y., Adsorption of poly(acrylic acid) onto the surface of titanium dioxide and the colloidal stability of aqueous suspension. *J Colloid Interface Sci* **2005**, *281* (1), 155-63.
32. Shen, Z. G.; Chen, J. F.; Zou, H. K.; Yun, J., Dispersion of nanosized aqueous suspensions of barium titanate with ammonium polyacrylate. *J Colloid Interface Sci* **2004**, *275* (1), 158-64.
33. Singh, B. P.; Bhattacharjee, S.; Besra, L.; Sengupta, D. K., Evaluation of dispersibility of aqueous alumina suspension in presence of Darvan C. *Ceramics International* **2004**, *30* (6), 939-946.
34. Moradi, M.; He, Q.; Willing, G. A., Tuning the stabilization mechanism of nanoparticle-regulated complex fluids. *Colloids and Surfaces A: Physicochemical and Engineering Aspects* **2019**, *577*, 532-540.

35. Tohver, V.; Smay, J. E.; Braem, A.; Braun, P. V.; Lewis, J. A., Nanoparticle halos: a new colloid stabilization mechanism. *Proc Natl Acad Sci U S A* **2001**, *98* (16), 8950-4.
36. Tohver, V.; Chan, A.; Sakurada, O.; Lewis, J. A., Nanoparticle Engineering of Complex Fluid Behavior. *Langmuir* **2001**, *17* (26), 8414-8421.
37. Barr, S. A.; Luijten, E., Effective interactions in mixtures of silica microspheres and polystyrene nanoparticles. *Langmuir* **2006**, *22* (17), 7152-5.
38. Chan, A. T.; Lewis, J. A., Electrostatically tuned interactions in silica microsphere-polystyrene nanoparticle mixtures. *Langmuir* **2005**, *21* (19), 8576-9.
39. Kong, D.; Yang, H.; Yang, Y.; Wei, S.; Wang, J.; Cheng, B., Dispersion behavior and stabilization mechanism of alumina powders in silica sol. *Materials Letters* **2004**, *58* (27-28), 3503-3508.
40. Cerbelaud, M.; Videcoq, A.; Rossignol, F.; Piechowiak, M. A.; Bochicchio, D.; Ferrando, R., Heteroaggregation of ceramic colloids in suspensions. *Advances in Physics: X* **2016**, *2* (1), 35-53.
41. Shen, C.; Wu, L.; Zhang, S.; Ye, H.; Li, B.; Huang, Y., Heteroaggregation of microparticles with nanoparticles changes the chemical reversibility of the microparticles' attachment to planar surfaces. *J Colloid Interface Sci* **2014**, *421*, 103-13.
42. Dylla-Spears, R.; Wong, L.; Miller, P. E.; Feit, M. D.; Steele, W.; Suratwala, T., Charged micelle halo mechanism for agglomeration reduction in metal oxide particle based polishing slurries. *Colloids and Surfaces A: Physicochemical and Engineering Aspects* **2014**, *447*, 32-43.
43. Wu, W. S.; Queiroz, M. E.; Mohallem, N. D. S., The effect of precipitated calcium carbonate nanoparticles in coatings. *Journal of Coatings Technology and Research* **2015**, *13* (2), 277-286.
44. Barry, M. M.; Jung, Y.; Lee, J.-K.; Phuoc, T. X.; Chyu, M. K., Fluid filtration and rheological properties of nanoparticle additive and intercalated clay hybrid bentonite drilling fluids. *Journal of Petroleum Science and Engineering* **2015**, *127*, 338-346.
45. Ji, S.; Herman, D.; Walz, J. Y., Manipulating microparticle interactions using highly charged nanoparticles. *Colloids and Surfaces A: Physicochemical and Engineering Aspects* **2012**, *396*, 51-62.
46. He, Q. Investigation of stabilization mechanisms for colloidal suspension using nanoparticles. University of Louisville, 2014.
47. Piech, M.; Walz, J. Y., Analytical Expressions for Calculating the Depletion Interaction Produced by Charged Spheres and Spheroids. *Langmuir* **2000**, *16* (21), 7895-7899.
48. Ducker, W. A.; Senden, T. J.; Pashley, R. M., Measurement of forces in liquids using a force microscope. *Langmuir* **2002**, *8* (7), 1831-1836.
49. Liu, J.; Luijten, E., Colloidal stabilization via nanoparticle halo formation. *Phys Rev E Stat Nonlin Soft Matter Phys* **2005**, *72* (6 Pt 1), 061401.
50. Liu, J.; Luijten, E., Stabilization of colloidal suspensions by means of highly charged nanoparticles. *Phys Rev Lett* **2004**, *93* (24), 247802.

51. Provatas, A.; Matison, J. G., Silsesquioxanes: Synthesis and applications. *Trends Polym Sci* **1997**, *5* (10), 327-332.
52. Feher, F. J.; Walzer, J. F., Synthesis and Characterization of Vanadium-Containing Silsesquioxanes. *Inorg Chem* **1991**, *30* (8), 1689-1694.
53. Li, G. Z.; Wang, L. C.; Ni, H. L.; Pittman, C. U., Polyhedral oligomeric silsesquioxane (POSS) polymers and copolymers: A review. *Journal of Inorganic and Organometallic Polymers* **2001**, *11* (3), 123-154.
54. Eisenberg, P.; Erra-Balsells, R.; Ishikawa, Y.; Lucas, J. C.; Mauri, A. N.; Nonami, H.; Riccardi, C. C.; Williams, R. J. J., Cagelike precursors of high-molar-mass silsesquioxanes formed by the hydrolytic condensation of trialkoxysilanes. *Macromolecules* **2000**, *33* (6), 1940-1947.
55. Gravel, M. C.; Laine, R. M., Synthesis and characterization of a new amino-functionalized silsesquioxane. *Abstr Pap Am Chem S* **1997**, *214*, 194-Poly.
56. Bronstein, L. M.; Linton, C. N.; Karlinsey, R.; Ashcraft, E.; Stein, B. D.; Svergun, D. I.; Kozin, M.; Khotina, I. A.; Spontak, R. J.; Werner-Zwanziger, U.; Zwanziger, J. W., Controlled synthesis of novel metalated poly(aminohexyl)-(aminopropyl)silsesquioxane colloids. *Langmuir* **2003**, *19* (17), 7071-7083.
57. Feher, F. J.; Budzichowski, T. A., Silsesquioxanes as Ligands in Inorganic and Organometallic Chemistry. *Polyhedron* **1995**, *14* (22), 3239-3253.
58. Mori, H., Design and Synthesis of Functional Silsesquioxane-Based Hybrids by Hydrolytic Condensation of Bulky Triethoxysilanes. *Int J Polym Sci* **2012**, *2012*, 17.
59. Sulaiman, S. Synthesis and Characterization of Polyfunctional Polyhedral Silsesquioxane Cages. *Dissertation*, University of Michigan, 2011.
60. Ro, H. W.; Soles, C. L., Silsesquioxanes in nanoscale patterning applications. *Materials Today* **2011**, *14* (1-2), 20-33.
61. Liu, Y. Z.; Wu, X. R.; Sun, Y.; Xie, W. L., POSS Dental Nanocomposite Resin: Synthesis, Shrinkage, Double Bond Conversion, Hardness, and Resistance Properties. *Polymers-Basel* **2018**, *10* (4).
62. Wang, Y.; Vaneski, A.; Yang, H. H.; Gupta, S.; Hetsch, F.; Kershaw, S. V.; Teoh, W. Y.; Li, H. R.; Rogach, A. L., Polyhedral Oligomeric Silsesquioxane as a Ligand for CdSe Quantum Dots. *J Phys Chem C* **2013**, *117* (4), 1857-1862.
63. Elumalai, V.; Sangeetha, D., Anion exchange composite membrane based on octa quaternary ammonium Polyhedral Oligomeric Silsesquioxane for alkaline fuel cells. *J Power Sources* **2018**, *375*, 412-420.
64. Lee, J.; Cho, H. J.; Jung, B. J.; Cho, N. S.; Shim, H. K., Stabilized blue luminescent polyfluorenes: Introducing polyhedral oligomeric silsesquioxane. *Macromolecules* **2004**, *37* (23), 8523-8529.
65. Chanmungkalakul, S.; Ervithayasuporn, V.; Hanprasit, S.; Masik, M.; Prigyai, N.; Kiatkamjornwong, S., Silsesquioxane cages as fluoride sensors. *Chem Commun* **2017**, *53* (89), 12108-12111.

66. Smay, J. E.; Gratson, G. M.; Shepherd, R. F.; Cesarano, J.; Lewis, J. A., Directed Colloidal Assembly of 3D Periodic Structures. *Advanced Materials* **2002**, *14* (18), 1279-1283.
67. Wang, Y.; Vaneski, A.; Yang, H.; Gupta, S.; Hetsch, F.; Kershaw, S. V.; Teoh, W. Y.; Li, H.; Rogach, A. L., Polyhedral Oligomeric Silsesquioxane as a Ligand for CdSe Quantum Dots. *The Journal of Physical Chemistry C* **2013**, *117* (4), 1857-1862.
68. Baney, R. H.; Itoh, M.; Sakakibara, A.; Suzuki, T., Silsesquioxanes. *Chemical Reviews* **1995**, *95* (5), 1409-1430.
69. Musić, S.; Filipović-Vinceković, N.; Sekovanić, L., Precipitation of amorphous SiO₂ particles and their properties. *Brazilian Journal of Chemical Engineering* **2011**, *28* (1), 89-94.
70. Nallathambi, G.; Ramachandran, T.; Rajendran, V.; Palanivelu, R., Effect of silica nanoparticles and BTCA on physical properties of cotton fabrics. *Materials Research* **2011**, *14* (4), 552-559.
71. Moradi, M.; Woods, B. M.; Rathnayake, H.; Williams, S. J.; Willing, G. A., Effect of functionalization on the properties of silsesquioxane: a comparison to silica. *Colloid and Polymer Science* **2019**, *297* (5), 697-704.
72. Parks, G. A., The Isoelectric Points of Solid Oxides, Solid Hydroxides, and Aqueous Hydroxo Complex Systems. *Chemical Reviews* **1965**, *65* (2), 177-198.
73. Kornprobst, T.; Plank, J., Photodegradation of Rhodamine B in Presence of CaO and NiO-CaO Catalysts. *International Journal of Photoenergy* **2012**, *2012*, 1-6.
74. Ridler, T. W. C., S., Picture Thresholding Using an Iterative Selection Method. *IEEE Transactions on Systems, Man, and Cybernetics* **1978**, *8* (8), 630-632.
75. *CRC handbook of chemistry and physics*. 84 ed.; CRC Press: 2003-2004.
76. Thommes, M.; Kaneko, K.; Neimark, A. V.; Olivier, J. P.; Rodriguez-Reinoso, F.; Rouquerol, J.; Sing, K. S. W., Physisorption of gases, with special reference to the evaluation of surface area and pore size distribution (IUPAC Technical Report). *Pure and Applied Chemistry* **2015**, *87* (9-10), 1051-1069.
77. Lawrence, M.; Jiang, Y., Porosity, Pore Size Distribution, Micro-structure. In *Bio-aggregates Based Building Materials*, 2017; pp 39-71.
78. Buzzaccaro, S.; Tripodi, A.; Rusconi, R.; Vigolo, D.; Piazza, R., Kinetics of sedimentation in colloidal suspensions. *Journal of Physics: Condensed Matter* **2008**, *20* (49).
79. Reerink, H.; Overbeek, J. T. G., The rate of coagulation as a measure of the stability of silver iodide sols. *Discussions of the Faraday Society* **1954**, *18*.
80. Boltachev, G. S.; Ivanov, M. G., Effect of nanoparticle concentration on coagulation rate of colloidal suspensions. *Heliyon* **2020**, *6* (2), e03295.
81. Miller, C. C., The Stokes-Einstein law for diffusion in solution. *Royal Society* **1924**, *106*, 724-749.
82. Mazo, R. M., Einstein-Smoluchowski Theory. In *Brownian Motion*, 2008; pp 46-61.

83. Bulatovic, S. M., Dispersion, Coagulation and Flocculation. In *Handbook of Flotation Reagents*, 2007; pp 215-233.
84. McGown, D. N. L.; Parfitt, G. D., Improved theoretical calculation of the stability ratio for colloidal systems. *The Journal of Physical Chemistry* **2002**, *71* (2), 449-450.
85. Russel, W. B.; Saville, D. A.; Schowalter, W. R., *Colloidal Dispersions*. Cambridge University Press: 2012.
86. Sedimentation. In *An Introduction to Dynamics of Colloids*, 1996; pp 443-493.
87. Zaki, J. F. R. W. N., Sedimentation and fluidisation. Part 1. *Transactions of the Institution of Chemical Engineers* **1954**, *32*, 35-53.
88. Baldock, T. E.; Tomkins, M. R.; Nielsen, P.; Hughes, M. G., Settling velocity of sediments at high concentrations. *Coastal Engineering* **2004**, *51* (1), 91-100.
89. Prasher, R.; Bhattacharya, P.; Phelan, P. E., Thermal conductivity of nanoscale colloidal solutions (nanofluids). *Phys Rev Lett* **2005**, *94* (2), 025901.
90. Kamat, P. V., Quantum Dot Solar Cells. The Next Big Thing in Photovoltaics. *J Phys Chem Lett* **2013**, *4* (6), 908-18.
91. Wu, J. H.; Chung, D. D. L., Improving colloidal graphite for electromagnetic interference shielding using 0.1 μ m diameter carbon filaments. *Carbon* **2003**, *41* (6), 1313-1315.
92. Di Leonardo, R.; Ianni, F.; Ruocco, G., Colloidal attraction induced by a temperature gradient. *Langmuir* **2009**, *25* (8), 4247-50.
93. Wurger, A., Thermophoresis in colloidal suspensions driven by Marangoni forces. *Phys Rev Lett* **2007**, *98* (13), 138301.
94. Piazza, R., Thermophoresis: moving particles with thermal gradients. *Soft Matter* **2008**, *4* (9).
95. Yang, M.; Ripoll, M., Thermophoretically induced flow field around a colloidal particle. *Soft Matter* **2013**, *9* (18).
96. Duhr, S.; Braun, D., Why molecules move along a temperature gradient. *Proc Natl Acad Sci U S A* **2006**, *103* (52), 19678-82.
97. Burelbach, J.; Zupkauskas, M.; Lamboll, R.; Lan, Y.; Eiser, E., Colloidal motion under the action of a thermophoretic force. *J Chem Phys* **2017**, *147* (9), 094906.
98. Piazza, R., Thermal forces : colloids in temperature gradients. *Journal of Physics: Condensed Matter* **2004**, *16* (38), S4195-S4211.
99. Garcíagarcía, S.; Wold, S.; Jonsson, M., Effects of temperature on the stability of colloidal montmorillonite particles at different pH and ionic strength. *Applied Clay Science* **2009**, *43* (1), 21-26.
100. Huang, Y., Temperature Effect on the Aggregation Kinetics of CeO₂ Nanoparticles in Monovalent and Divalent Electrolytes. *Journal of Environmental & Analytical Toxicology* **2012**, *02* (07).
101. Lyklema, J., *Fundamentals of Interface and Colloid Science*. 1st ed.; 1995.
102. Higashitani, K.; Imura, K.; Vakarelski, I. U., Fundamentals of Breakage of Aggregates in Fluids. *KONA Powder and Particle Journal* **2000**, *18* (0), 26-40.

103. Conn, P. M., *Confocal microscopy*. 1999; Vol. 307, p 663.
104. *Confocal Microscopy: Principles, Techniques and Applications*. Nova Science Publishers, Inc.: 2016.
105. Sternberg, Biomedical Image Processing. *Computer* **1983**, *16* (1), 22-34.
106. Thijssen, J. H.; Clegg, P. S., Emulsification in binary liquids containing colloidal particles: a structure-factor analysis. *J Phys Condens Matter* **2010**, *22* (45), 455102.
107. Teece, L. J.; Faers, M. A.; Bartlett, P., Ageing and collapse in gels with long-range attractions. *Soft Matter* **2011**, *7* (4), 1341-1351.
108. Hsiao, L. C.; Doyle, P. S., Celebrating Soft Matter's 10th Anniversary: Sequential phase transitions in thermoresponsive nanoemulsions. *Soft Matter* **2015**, *11* (43), 8426-31.
109. Rahman, M. M.; Williams, S. J., Cyclic force driven colloidal self-assembly near a solid surface. *Journal of Fluid Mechanics* **2020**.
110. Toyotama, A.; Yamanaka, J.; Yonese, M.; Sawada, T.; Uchida, F., Thermally driven unidirectional crystallization of charged colloidal silica. *J Am Chem Soc* **2007**, *129* (11), 3044-5.
111. Wu, L.; Wang, X.; Wang, G.; Chen, G., In situ X-ray scattering observation of two-dimensional interfacial colloidal crystallization. *Nat Commun* **2018**, *9* (1), 1335.
112. Smith, R.; Inomata, H.; Peters, C., Equations of State and Formulations for Mixtures. In *Introduction to Supercritical Fluids - A Spreadsheet-based Approach*, 2013; pp 333-480.
113. Frenkel, D.; Smit, B., *Understanding Molecular Simulation From Algorithm to Applications*. Academic Press: San Diego, Calif, USA, 1996; Vol. 1.
114. Hofer, T. S.; Rode, B. M.; Pribil, A. B.; Randolph, B. R., Simulations of Liquids and Solutions Based on Quantum Mechanical Forces. In *Theoretical and Computational Inorganic Chemistry*, 2010; pp 143-175.
115. Maginn, E. J.; Elliott, J. R., Historical Perspective and Current Outlook for Molecular Dynamics As a Chemical Engineering Tool. *Industrial & Engineering Chemistry Research* **2010**, *49* (7), 3059-3078.
116. Alder, B. J.; Wainwright, T. E., Phase Transition for a Hard Sphere System. *The Journal of Chemical Physics* **1957**, *27* (5), 1208-1209.
117. Rahman, A., Correlations in the Motion of Atoms in Liquid Argon. *Physical Review* **1964**, *136* (2A), A405-A411.
118. Zhang, F.; Allen, A. J.; Levine, L. E.; Tsai, D. H.; Ilavsky, J., Structure and Dynamics of Bimodal Colloidal Dispersions in a Low-Molecular-Weight Polymer Solution. *Langmuir* **2017**, *33* (11), 2817-2828.
119. Wereszczynski, J.; McCammon, J. A., Statistical mechanics and molecular dynamics in evaluating thermodynamic properties of biomolecular recognition. *Q Rev Biophys* **2012**, *45* (1), 1-25.
120. Ulberg, D. E.; Churaev, N. V.; Ilyin, V. V.; Malashenko, G. L., Molecular dynamics simulation of the aggregation of colloidal particles. *Colloids and Surfaces A: Physicochemical and Engineering Aspects* **1993**, *80* (2-3), 93-102.

121. Fichthorn, K. A.; Qin, Y., Molecular-dynamics simulation of colloidal nanoparticle forces. *Ind Eng Chem Res* **2006**, *45* (16), 5477-5481.
122. Sandev, T.; Tomovski, Ž., Generalized Langevin Equation. In *Fractional Equations and Models*, 2019; pp 247-300.
123. Schneider, R.; Sharma, A. R.; Rai, A., Introduction to Molecular Dynamics. In *Computational Many-Particle Physics*, 2008; pp 3-40.
124. Chen, J., The Development and Comparison of Molecular Dynamics Simulation and Monte Carlo Simulation. *IOP Conference Series: Earth and Environmental Science* **2018**, *128*.
125. Harrison, R. L., Introduction To Monte Carlo Simulation. *AIP Conf Proc* **2010**, *1204*, 17-21.
126. Liu, J.; Luijten, E., Rejection-free geometric cluster algorithm for complex fluids. *Phys Rev Lett* **2004**, *92* (3), 035504.
127. Torrie, G. M.; Valleau, J. P., Nonphysical sampling distributions in Monte Carlo free-energy estimation: Umbrella sampling. *Journal of Computational Physics* **1977**, *23* (2), 187-199.
128. Derjaguin, B.; Landau, L., Theory of the stability of strongly charged lyophobic sols and of the adhesion of strongly charged particles in solutions of electrolytes. *Progress in Surface Science* **1993**, *43* (1-4), 30-59.
129. Kontogeorgis, G. M.; Kiil, S., *Introduction to Applied Colloid and Surface Chemistry*. Wiley: 2016.
130. Hamaker, H. C., The London—van der Waals attraction between spherical particles. *Physica* **1937**, *4* (10), 1058-1072.
131. Renger, C.; Kuschel, P.; Kristoffersson, A.; Clauss, B.; Oppermann, W.; Sigmund, W., Colloid probe investigation of the stabilization mechanism in aqueous 1,2-propanediol nano-zirconia dispersions. *Physical Chemistry Chemical Physics* **2004**, *6* (7).
132. Renger, C.; Kuschel, P.; Kristoffersson, A.; Clauss, B.; Oppermann, W.; Sigmund, W., Colloid probe investigation of the stabilization mechanism in aqueous 1,2-propanediol nano-zirconia dispersions. *Phys Chem Chem Phys* **2004**, *6* (7), 1467-1474.
133. Ducker, W. A.; Senden, T. J.; Pashley, R. M., Measurement of forces in liquids using a force microscope. *Langmuir* **1992**, *8* (7), 1831-1836.
134. Prica, M.; Biggs, S.; Grieser, F.; Healy, T. W., Effect of calcination temperature on the electrokinetic properties of colloidal zirconia. *Colloid Surface A* **1996**, *119* (2-3), 205-213.
135. Asakura, S.; Oosawa, F., On Interaction between Two Bodies Immersed in a Solution of Macromolecules. *The Journal of Chemical Physics* **1954**, *22* (7), 1255-1256.
136. Mills, M. Potentials of Mean Force as a Starting Point for Understanding Biomolecular Interactions. University of Michigan, 2010.
137. van Gunsteren, W. F.; Daura, X.; Mark, A. E., Computation of Free Energy. *Helvetica Chimica Acta* **2002**, *85* (10), 3113-3129.
138. Kastner, J., Umbrella sampling. *Wires Comput Mol Sci* **2011**, *1* (6), 932-942.

139. Ferguson, A. L., BayesWHAM: A Bayesian approach for free energy estimation, reweighting, and uncertainty quantification in the weighted histogram analysis method. *J Comput Chem* **2017**, *38* (18), 1583-1605.
140. Zheng, L.; Alhossary, A. A.; Kwoh, C.-K.; Mu, Y., Molecular Dynamics and Simulation. In *Encyclopedia of Bioinformatics and Computational Biology*, 2019; pp 550-566.
141. Kumar, S.; Rosenberg, J. M.; Bouzida, D.; Swendsen, R. H.; Kollman, P. A., Multidimensional free-energy calculations using the weighted histogram analysis method. *Journal of Computational Chemistry* **1995**, *16* (11), 1339-1350.
142. Almarza, N. G.; Lomba, E., Determination of the interaction potential from the pair distribution function: an inverse Monte Carlo technique. *Phys Rev E Stat Nonlin Soft Matter Phys* **2003**, *68* (1 Pt 1), 011202.
143. Manoharan, V. N., COLLOIDS. Colloidal matter: Packing, geometry, and entropy. *Science* **2015**, *349* (6251), 1253751.
144. Bastos, H.; Bento, R.; Schaeffer, N.; Coutinho, J. A. P.; Perez-Sanchez, G., Using coarse-grained molecular dynamics to rationalize biomolecule solubilization mechanisms in ionic liquid-based colloidal systems. *Phys Chem Chem Phys* **2020**, *22* (42), 24771-24783.
145. Moore, T. C.; Iacovella, C. R.; McCabe, C., Derivation of coarse-grained potentials via multistate iterative Boltzmann inversion. *J Chem Phys* **2014**, *140* (22), 224104.
146. Pak, A. J.; Dannenhoffer-Lafage, T.; Madsen, J. J.; Voth, G. A., Systematic Coarse-Grained Lipid Force Fields with Semiexplicit Solvation via Virtual Sites. *J Chem Theory Comput* **2019**, *15* (3), 2087-2100.
147. Jadrach, R. B.; Bollinger, J. A.; Lindquist, B. A.; Truskett, T. M., Equilibrium cluster fluids: pair interactions via inverse design. *Soft Matter* **2015**, *11* (48), 9342-54.
148. Li, Z.; Bian, X.; Yang, X.; Karniadakis, G. E., A comparative study of coarse-graining methods for polymeric fluids: Mori-Zwanzig vs. iterative Boltzmann inversion vs. stochastic parametric optimization. *J Chem Phys* **2016**, *145* (4), 044102.
149. Choudhury, C. K.; Carbone, P.; Roy, S., Scalability of Coarse-Grained Potentials Generated from Iterative Boltzmann Inversion for Polymers: Case Study on Polycarbonates. *Macromolecular Theory and Simulations* **2016**, *25* (3), 274-286.
150. Reith, D.; Putz, M.; Muller-Plathe, F., Deriving effective mesoscale potentials from atomistic simulations. *J Comput Chem* **2003**, *24* (13), 1624-36.

CURRICULUM VITAE

Marzieh Moradi, PhD

m.moradizani@gmail.com | <https://www.linkedin.com/in/marzieh-moradi/>

EDUCATION

Ph.D., Chemical Engineering | University of Louisville, Louisville, KY

Dissertation: *Aggregation dynamics of bulk nanoparticle haloing systems and the influence of non-ambient temperatures*

M.S., Chemical Engineering | Isfahan University of Technology, Isfahan, IR

Thesis: *Experimental study on removal of Cu and Pb ions from aqueous solution by poly (vinyl alcohol)-coated Fe₃O₄ magnetic nanoparticles*

B.S., Chemical Engineering | Isfahan University of Technology, Isfahan, IR

Thesis: *Synthesis of exfoliated graphite and experimental study on removal of MTBE from aqueous solution*

TECHNICAL SKILLS

Laboratory Techniques: Atomic Force Microscopy (AFM); Scanning Electron Microscopy (SEM); X-Ray Crystallography (XRD); BET Surface Area Measurement; Particle Size/ Zeta Potential Analysis (DLS); FTIR Spectroscopy; Raman Spectroscopy; Confocal Microscopy; Gas Pycnometry; Spin coating (Spinner) HIAC Liquid Particle Counter; High Performance Liquid Chromatography (HPLC); Gas Chromatography (GC); Differential Scanning Calorimetry (DSC); Thermal Gravimetric Analysis (TGA);

Software: HOOMD-blue; Minitab (Design of Experiments, DOE); ImageJ; Microsoft Office Suite;

Programming Language: Bash scripting; Python; MATLAB

PROFESSIONAL EXPERIENCE

Parenteral Drug Product MS&T Co-op | Bristol Myers Squibb, NJ 07/2020 to 12/2020

A member of the process characterization team, at the Parenteral Drug Product Manufacturing Science and Technology Department, actively involved in developing and executing experiments to support process improvements, product robustness, new technology and tech transfer implementation, and/or commercial manufacturing investigations of different liquid, lyophilized, and pre-filled syringe drug products.

Graduate Research Assistant | University of Louisville, Louisville, KY 08/2015 to 05/2021

Executed various research duties pertaining to data collation, research experimentations, and statistical analysis. Designed and developed all completed investigations and testing procedures associated with the application of heat to samples in ground-based experiments. Conducted multiple, innovative molecular dynamic simulations, of the colloidal systems, and prepared comprehensive reports that provide extensive information on techniques used, technical errors discovered, and solutions rendered.

Teaching Assistant | University of Louisville, Louisville, KY 08/2016 to 06/2021

Collaborated with the Professor to facilitate course curriculum construction and material preparation for students in courses such as Computer Applications, Chemical Engineering Kinetics, Advanced Kinetics and Reactor Design, and Modeling and Transport Phenomena. Revised lesson materials and provided consistent tutoring and mentorship to students when necessary. Evaluated oral course project presentations and documented student progress.

PUBLICATIONS

- M. Moradi, V. W. Jaeger, and G.A. Willing, “Molecular Dynamics Simulations of Binary Colloidal Mixtures of Silica and Zirconia Particles”, Materials Letters, manuscript preparation.
- M. Moradi, S. J. Williams, and G.A. Willing, “Effect of Temperature on Nanoparticle Haloing”, Journal of Colloid and Interface Science, manuscript preparation.
- M. Moradi, Q. He, and G. A. Willing, “Tuning the Stabilization Mechanism of Nanoparticle-regulated Complex Fluids”, Colloids Surf. A Physicochem. Eng. Asp., 577 (2019), pp. 532-540, 10.1016/j.colsurfa.2019.06.021
- M. Moradi, B. M. Woods, H. Rathnayake, S. J. Williams, and G. A. Willing, “Effect of Functionalization on the Properties of Silsesquioxane; a Comparison to Silica”, Colloid Polym Sci (2019) 297: pp. 697-704, 10.1007/s00396-019-04489-3
- A. Dudabi Nezhad, M. Akbari Sayar, M. Moradi, E. Baghban, “Short-Term, Mid-Term and Long-Term Optimizing Energy Plans of Iran Metal Casting” – In Persian language, National Conference of Optimizing Energy Consumption in Iron and Steel Industry of Iran, 2012
- M. Vosooghi far, S. Fazeli, E. Baghban, M. Moradi, “Roadmap Framework for Optimizing Energy Consumption in Iran Metal Casting” – In Persian language, National Conference of Optimizing Energy Consumption in Iron and Steel Industry of Iran, 2012
- M. Moradi, S. Mohamadian, K. Karimi, “Modeling of Fischer-Tropsch Process in a Tubular Reactor with Removal of Water” – In Persian language, 12th National Iranian Chemical Engineering Congress, 2008

PRESENTATIONS

- M. Moradi, V.W. Jaeger, S.J. Williams, G.A. Willing, “Mechanisms of Nanoparticle Haloing for the Control of Colloidal Stability”, Oral Presentation, AIChE Conference, USA, 2019.
- M. Moradi, V.W. Jaeger, S.J. Williams, G.A. Willing, “Molecular Dynamics Simulations of Binary Colloidal Mixtures of Silica and Zirconia Particles”, Oral Presentation, ASGSR Conference, USA, 2018.
- M. Moradi, S.J. Williams, G.A. Willing, “Stabilization of silsesquioxane microparticles with highly charged nanoparticles”, Oral Presentation, Graduate Student Regional Research Conference, University of Louisville, USA, 2018.
- M. Moradi, S.J. Williams, G.A. Willing, “Stabilization of Colloidal Suspensions with a Bimodal Distribution of Microparticles and Nanoparticles”, Oral Presentation, AIChE Conference, USA, 2017.
- M. Moradi, J.J. Lee, S.J. Williams, G.A. Willing, “Interparticle Interaction Forces and the Stability of Colloidal Suspensions in the Presence of Charged Nanoparticles”, Poster Presentation, ASGSR Conference, USA, 2016.
- M. Moradi, A. Moheb, S. Gh. Etemad, “Fast adsorption of Cu(II) Ions from Water by Magnetic Polyvinyl Alcohol Nanoparticles”, Poster Presentation, International Conference on Nanotechnology: Fundamentals and Applications, Canada, 2010.
- M. Moradi, S. GH. Etemad, A. Moheb, “Synthesis of Magnetic Polyvinyl Alcohol Nanoparticles for Fast Adsorption of Pb(II) Ions from Water”, Poster Presentation, International Conference on Nanotechnology: Fundamentals and Applications, Canada, 2010.